2021

Synthesis and Assessment of Sustainable Fuels for Transportation and Space Exploration

Katerina Chagoya
University of Central Florida

SYNTHESIS AND ASSESSMENT OF SUSTAINABLE FUELS FOR TRANSPORTATION AND SPACE EXPLORATION

by

KATERINA CHAGOYA
B.S. University of Central Florida, 2016
M.S. University of Central Florida, 2021

A dissertation submitted in partial fulfillment of the requirements
for the degree of Doctor of Philosophy in Mechanical Engineering
in the Department of Mechanical and Aerospace Engineering
in the College of Engineering and Computer Science
at the University of Central Florida
Orlando, Florida

Fall Term
2021

Major Professors: Richard G. Blair and Jayanta S. Kapat

ABSTRACT

As global energy sources transition towards renewable energy, the demand for sustainable fuels has never been greater. The sheer scale of this transition will require numerous solutions to accommodate for the diverse and complex situations worldwide. This dissertation will discuss 3 studies: the utilization of CO_2 waste gas to produce fuels sustainably, characterizing biofuels for efficient use in automobiles, and developing a solid, emissonless fuel intended for spaceflight but also applicable on Earth.

The hydrogenation of CO_2 into value-added molecules could reduce greenhouse gas emissions if waste stream CO_2 were captured for conversion. We found that atomic vacancies induced in defect-laden hexagonal boron nitride (*dh*-BN) can activate the CO_2 molecule for hydrogenation. Subsequent hydrogenation to formic acid (HCOOH) and methanol (CH_3OH) occur through vacancy-facilitated co-adsorption of hydrogen and CO_2. Boron and nitrogen are abundant elements, making *h*-BN an attractive catalyst in the synthesis of value-added molecules, facilitating efforts to reduce GHG emissions.

Biofuels could be vital in a sustainable fuel future. However, their implementation into existing engines requires an understanding of their interactions with engine components at temperature. The formation of carbon deposits on hot metal components can reduce engine performance. Using a novel test rig and gasoline and diesel analog compounds, the degree of fuel degradation to form carbon can be measured on various metal surfaces. Thus, we can screen for low soot-forming biofuels as promising candidates surface on the market.

Historically, innovations in space exploration have led to immensely beneficial applications on Earth. Currently, various limitations of power sources hinder the capacity for regular and frequent space exploration. The ability to harvest heat for electrical power would

reduce the cost of long-distance and long-duration missions. Employing a regulated, self-propagating, exothermic chemical reaction, we have devised a slow-burning reactant system capable of generating heat at a harvestable rate.

This dissertation is dedicated to my mom, Teodozja Lis,

my dad, Rodolfo Chagoya Ramirez,

and my father, Michael Demetrios Dermetzidis, who passed away,

for leaving everything behind in Poland, Mexico, and Greece,

so I could have this life and get this degree.

ACKNOWLEDGMENTS

I would like to thank my research advisor, Dr. Richard Blair, for his continued mentorship throughout my graduate and undergraduate degrees. My faculty advisor, Dr. Jayanta Kapat for his guidance throughout my mechanical engineering degree, as well as my committee members Dr. Laurene Tetard, Dr. Subith Vasu, and Dr. Nina Orlovskaya, for their assistance on various projects and help with this dissertation.

I thank the National Science Foundation (NSF) for their financial support for the work in Chapter 2, the Department of Energy (DOE) for their financial support of the work in Chapter 3, and the National Aeronautic and Space Administration (NASA) for their financial support of the work in Chapter 4.

To the graduate students that have come through the Blair Lab before me, thank you for your guidance and mentorship. To Jacob Todd, my original mentor, thank you for your patience and your sass, for always having a very long story that wastes time, and for all the MapQuest maps you printed me even though there are apps for that. To David Restrepo, thank you for always having the right information and for listening to every "Chagoya Method" I invented before dismissing them. To David Nash, thank you for making the lab a place of family, and for all the effort you put in to bring us all together for every holiday, birthday, and get-together. That includes made-up holidays, the summer bake-offs, and the annual Blair Group Christmas Tree Decorating tradition, which we all know is an elaborate conspiracy devised so Dr. Blair doesn't have to decorate his tree at home.

A special thank you to my coworkers and labmates over the last 4 and a half years, especially Fernand Torres-Davila, for his unwavering presence as an unofficial part of our lab group and for his momentary gifts of motivation and inspiration.

I would like to thank the many undergraduate students who have worked with me on various research projects throughout the years, including Jordyne Owens, Joseph Dalton, Alec Orosco, Alexandria Bias, Leandra Schneider, and Lauren Whetstone. A special thank you to Kayla Rothman and Errica Fusco for their immense help on the boron nitride catalysis work in Chapter 2 of this dissertation. Another thank you to Taylor Pitts and Samin Zaman for their efforts on the assessment of biofuels work in Chapter 3 of this dissertation. And thank you to Emma Blanco, Elan Marrero, and Jose Berger for their assistance on the solid pyrolants work in Chapter 4.

And of course, thank you to my close family and friends for your constant support through these years that I have been in school, especially my parents Teodozja and Rodolfo Chagoya, my brother and sister Demetrios and Michelle Chagoya, David Nash, Deepti Siddhanti, Lavina Ranjan, Wesley Blevins, and again, Fernand Torres-Davila. To David, you have been the most help throughout graduate school and beyond. Thank you for all you've done over the years.

TABLE OF CONTENTS

LIST OF FIGURES

LIST OF TABLES

CHAPTER 1: INTRODUCTION AND LITERATURE REVIEW

The globe's massive energy demands are largely met today by the burning of oil, coal, and natural gas. These three sources of energy, all derived from fossil fuels, power our electric grids, providing electricity to residential, commercial and industrial buildings and the vast majority of these fuels are used to power our various modes of transportation (Figure 1), including aviation, automobiles, trucks, buses, and ships. However, fossil fuels are not a renewable energy source and are not only depleting, but are detrimental to Earth's atmosphere [1, 2], oceans [3], ecosystems [3, 4], biodiversity [5], habitual weather cycles [6] and directly to human health and nutrition [7, 8]. These detriments are either direct or indirect consequences of burning hydrocarbon fuel and increasing levels of anthropogenic carbon dioxide in the atmosphere. Luckily, renewable energy alternatives exist and advances in technology have successfully reduced the cost of these newer power sources (i.e. solar, wind) below that of our conventional fuels.

However, transitioning so much of society's current infrastructure away from hydrocarbons and toward large-scale adoption of cleaner energies is an immense effort. The scale of this problem indicates a variety of scientific solutions are needed, as one or a few may not accommodate for diverse and complex situations and scenarios worldwide. While clean, green energies are being deployed across the globe, the discovery of sustainable syntheses of hydrocarbon fuels and utilization of biofuels may prove to be an important intermediate solution for climate mitigation. The objective of the studies discussed in the dissertation will be to facilitate progress in the areas of carbon dioxide conversion, biofuel usage in the automobile industry, and alternative energy sources in the space industry.

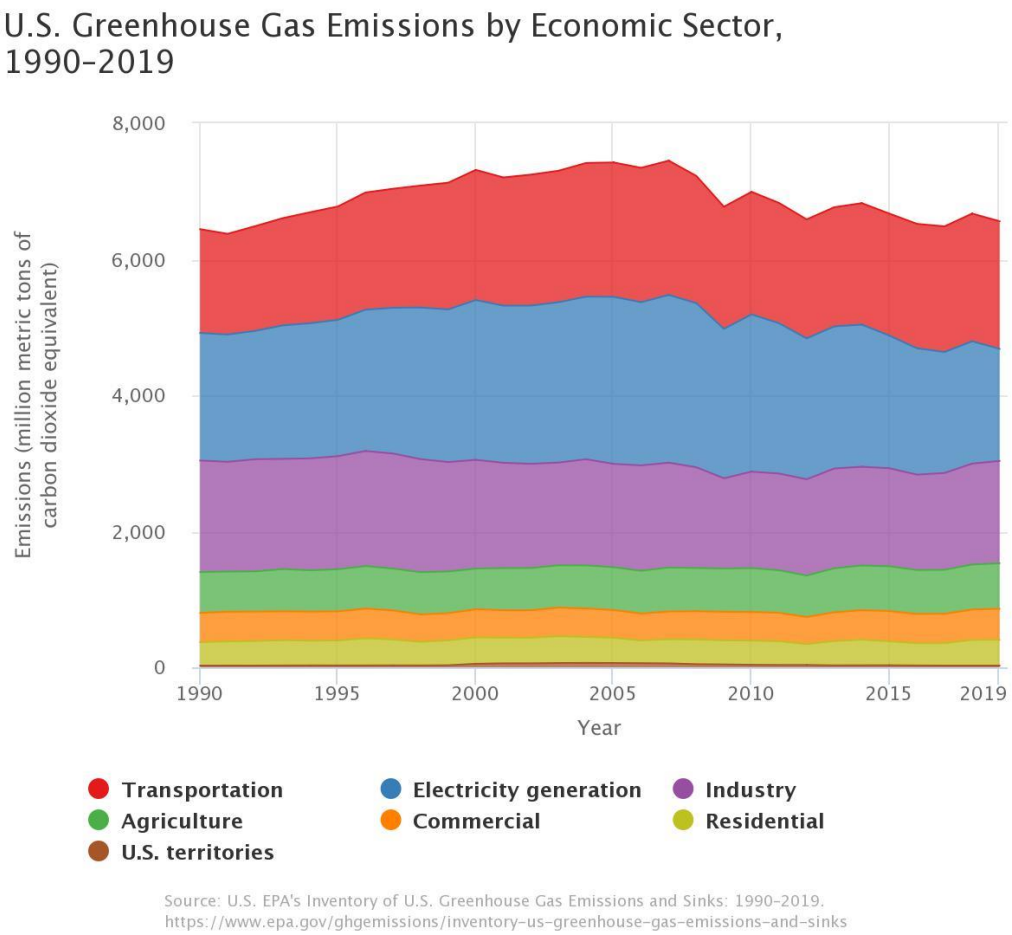

Figure 1: Sources of emissions by sector in the United States from 1990 to 2019. Image credit: EPA.

1.1 Catalytic Reduction of Carbon Dioxide

Research in carbon dioxide capture, utilization, and storage (CCUS) technologies have increased steadily over the last decade in an attempt to address concerns of increasing CO_2 emissions. While many carbon capture and storage (CCS) technologies intend to profit from compressed CO_2, or to inject carbon dioxide into rock formations undergroud, returning them from whence they came [9], carbon dioxide utilization can have significant benefits as well. CO_2 has garnered considerable scientific interest as a potential C_1 source for fuel production. [10-12] Carbon dioxide can be utilized in this way by carboxylation [12] or reduced via electrochemical [13], homogeneous [14] and heterogeneous [15, 16] means. The conversion of some CO_2 into

useful, valuable compounds could provide a monetary incentive for emitters to implement such technologies for profit and thus may increase manufacterer willingness to sequester carbon dioxide.

A prospective catalyst for CO_2 conversion is defect-laden hexagonal boron nitride (*dh*-BN), an environmentally safe, low-cost, non-metal, heterogeneous catalyst that both chemisorbs sufficiently large quantities of CO_2 on its surface and reduces it to methanol and formic acid.

1.1.1 Mechanocatalytic Activity of Boron Nitride

The crystal structure of pristine hexagonal boron nitride (*h*-BN) consists of layered sheets of alternating boron and nitrogen atoms, held together by Van der Waals forces (Figure 2). In its pristine state, boron nitride is an inert catalyst posessing no calatytic activity. However, sites which are catalytically active for hydrogenation (aka reduction) can be conveniently generated in the material by mechanical grinding.

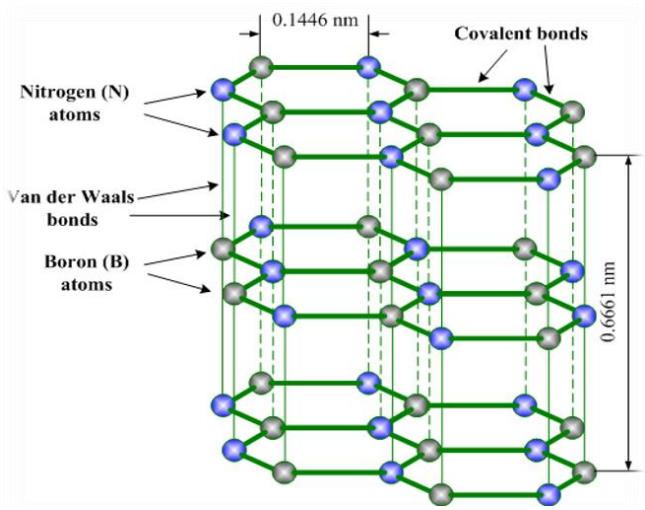

Figure 2: Structure of the h-BN crystal lattice containing alternating nitrogen (blue) and boron (gray) atoms in layered sheets.

Ball milling, or grinding, of the boron nitride sheets is accomplished by placing the material in a vial to be rapidly shaken among milling media (ball bearings). As the media compressively

impacts the *h*-BN powder, it acts to remove or rearrange atoms from the sheet arbitrarily, creating random locations of an atomic vacancy or irregularity. These sites now host regions of either electron deficiency or electron density as compared to the unaffected areas in the sheet. Figure 3 illustrates the variety of defect sites able to be produced by ball milling conditions. Density functional theory (DFT) calculations indicate that propene and other olefins have the greatest affinity for the N_B, B_N, V_N, and V_B defect sites, with the boron vacancy (V_B) having the largest affinity for both propene and hydrogen with binding energies of -3.69 eV and -4.95, respectively. [17]

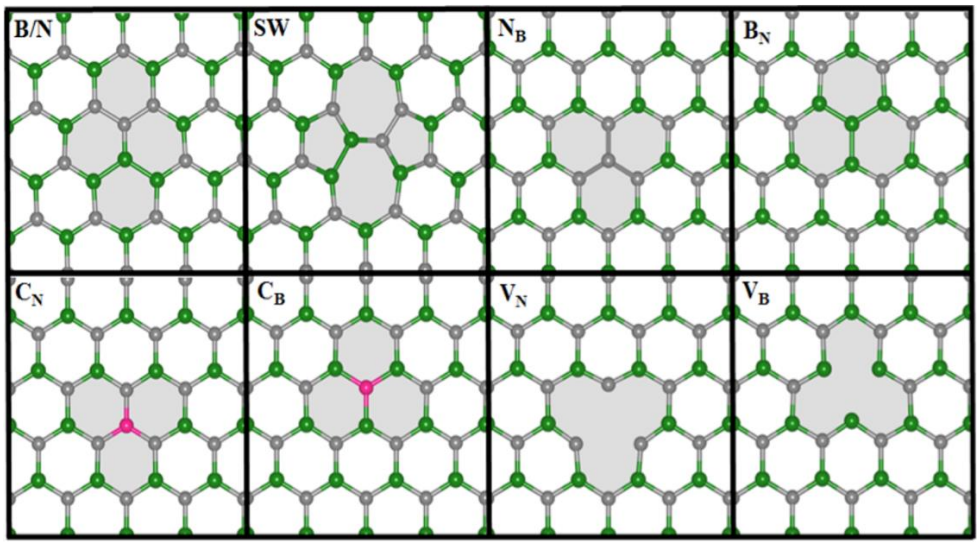

Figure 3: Different types of defect sites that can be generated in the boron nitride, as calculated by density functional theory (DFT). From the top left we have a boron nitrogen swap (B/N), Stone-Wales defect (SW), a nitrogen substitution for a boron (N_B), a boron substitution for nitrogen (B_N), a carbon substituted for a nitrogen (C_N), a carbon substituted for a boron (C_B), a nitrogen vacancy (V_N), and a boron vacancy (V_B). [17]

Following the creation of defect sites in a mixer mill, we have previously demonstrated that the *dh*-BN is catalytically active for hydrogenation of propene if the catalyst is continually subject to low-energy milling conditions in a second type of mill, a pebble mill. [17] A detailed background of different milling styles are discussed in the following section titled Mechanochemistry. The pebble mill subjects the *dh*-BN to plastic deformation as the ball bearings

impact the catalyst surface, somewhat similar to the impacts in the defect site creation stage using the mixer mill. It is hypothesized that plastic deformation of the *dh*-BN sheets leads to fluctuations in the binding energies of surface sites, inducing desorption of a substrate from a site. These observations are similarly true for the hydrogenation of carbon dioxide over *dh*-BN, and neither hydrogenation of propene nor CO_2 has been able to be replicated under static (non-milling) environments. However, if the catalyst is milled, the reduction of CO_2 over *dh*-BN has been demonstrated to produce high value products. Although *dh*-BN is best implemented in CO_2-rich conditions (namely, O_2-free) [18] it could still be used to catalytically recycle this combustion product back into fuel or valuable product at low temperatures if the CO_2 is isolated first, or the gas stream is oxygen deficient.

1.1.2 Mechanochemistry

The phenomenon of a mechanical action resulting in a chemical effect is known as mechanochemistry. The first uses of mechanochemistry can be dated as far back as the striking of rocks to produce a flame, though systematic implementation of mechanochemistry was first reported by M. Carey Lea (1823-1897). Mechanochemistry is defined as *"a branch of chemistry dealing with the chemical and physiological changes of substances of all states of aggregation due to influence of mechanical energy"*. [19] By applying mechanical energy, reactions can be induced in solids, providing a new path to synthesis.

The reaction of two chemicals in the solid phase has traditionally been performed in a variety of ways. Solids are oftentimes dissolved first in an appropriate solvent, which results in the introduction of an additional reagent. Solid-state reactions can be treated under elevated temperature and pressure, though the lack of intimate contact, non-uniform size distribution of the particles, and poor diffusion results in low efficiency. [20] In addition, such reactions are difficult

to perform in large batches, and chemical syntheses can only be performed in small quantities. However, implimenting mechanical action, agitation, or forces as part of the reaction procedure allows for the mitigation of these effects and results in simple chemical reaction synthesis, catalysis, and phase transformation.

Mechanochemical reactions can be performed within various types of ball mills. Each ball mill consists of a particularly shaped container, or vial, inside of which ball bearings are placed. When a mill is turned on, the motor causes the vial to undergo either shaking, rotation, spinning, or a combination of these motions, which in turn cause the ball bearings to exhibit a particular behavior in response. During a milling reaction, the chemical reagents within the vial encounter a sufficiently large magnitude of force and kinetic energy from ball bearing contact, that a reaction is forced. When performing such a reaction, there are many variables to consider when chosing the ideal ball mill. The type of reaction, the physical phase and hardness of the reagents, the quantity of material needing processing, and the modes of force required to achieve the desired result are a few variables to consider when chosing the ideal reactor. Some of these parameters are summarized in Table 1 for a mixer, pebble, attritor, and planetary mill. Additional details will be provided for the mixer and pebble mills, since they are utilized in experiments discussed in this dissertation.

Table 1: The mixer, pebble, attritor, and planetary mills are four examples of ball mills which can accomplish mechanochemical reactions.

Type	F_{max} (N) Energy Class	Forces at Work	Speed (RPM)	Loading Volume	Scalability
Mixer (Shaker) Mill	3053 High-energy	Compression Shear	1200	2-20g 2 vials/reactor	Low
Pebble Mill	329 Low-energy	Tumbling	Variable	>1000 kg	High
Attritor Mill	3881 High-energy	Compression Tumbling Shear	4000	100 kg	High
Planetary Mill	N/A	Centrifugal Compression Shear	600	250 g 4 vials/reactor	Low

1.1.2.1 Mixer Mill

The mixer (or shaker) mill is a common laboratory-scale mill with the smallest vial size. As seen in Figure 4, the mill consists of an arm (or sometimes 2 arms), where a cylindrical vial (Figure 5) is clamped, which rotates rapidly in a figure-eight motion. As the mill shakes the vial, the media inside collide with the top, bottom, and sides of the vessel, forcefully impacting the reactants.

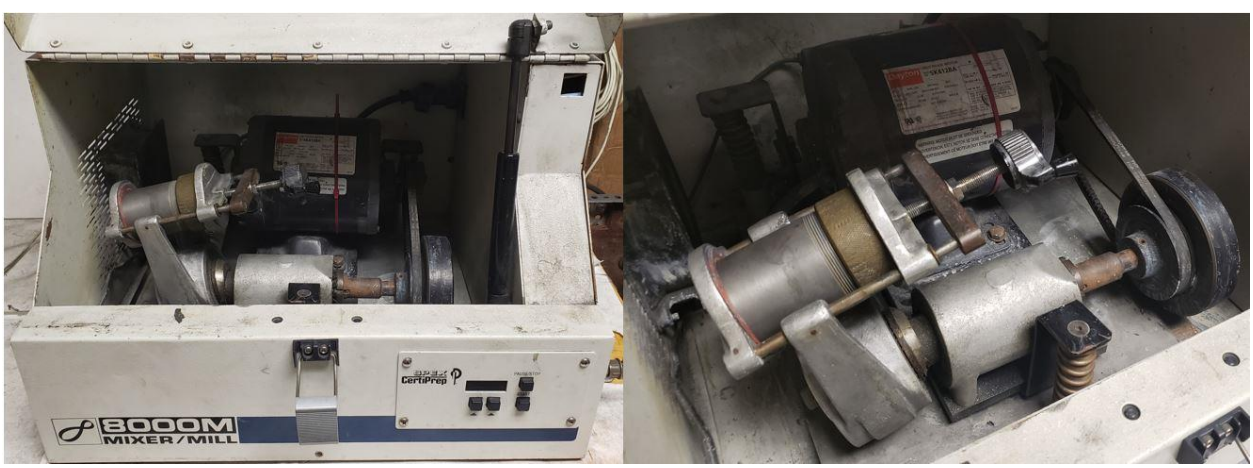

Figure 4: The shaker (mixer) mill with a clamped vial.

This type of mill is ideal for small-batch reactions on the order of a few grams, which is convenient for exploratory, discovery, or qualitative reactions, although quantitative reactions can also be performed. The stainless steel shaker mill vial is comprised of the cylindrical vial base, a lid which houses an o-ring to seal in the reagents, a threaded screw cap (brass), and a small number of milling media (ball bearings). The zirconia vial (white) is not threaded, and thus, the lid is placed on top of the vial and is clamped down using a unique clamping mechanism made from hose clamps. Both vials are gas-tight, but do not contain a gas inlet or outlet, and therefore have limited atmospheric control. Due to the mechanism in which the mill delivers the impacts (shaking), the mixer mill is ill-suited for large-scale industrial applications. Meaning, a proven successful chemical reaction in a mixer mill must be achieved again in a pebble or attritor mill in order to be scaled up to an industrial size, since large-scale versions of pebble and attritor mills do exist. However, pebble and attritor mills are inconvenient for exploratory research due to the effort required for set up and cleaning.

Figure 5: Shaker mill vials made out of stainless steel (left) and zirconia (right), both assembled and disassembeled (disassembly in center). The stainless steel vial is sealed gas-tight using a screw cap (brass) while the zirconia vial uses a unique clamp to compress the lid down onto an o-ring located on the vial itself.

1.1.2.2 Pebble Mill

The pebble (or roller) mill is an intermediate-sized mechanochemical reactor that can be used for both laboratory- and industrial-scale applications. A laboratory-scale pebble mill is pictured in Figure 6 and employs a gear and chain which rotates a horizontal-lying reaction vial. As the vial (Figure 7) rotates about its long-axis, the media within it tumble along with the reagents.

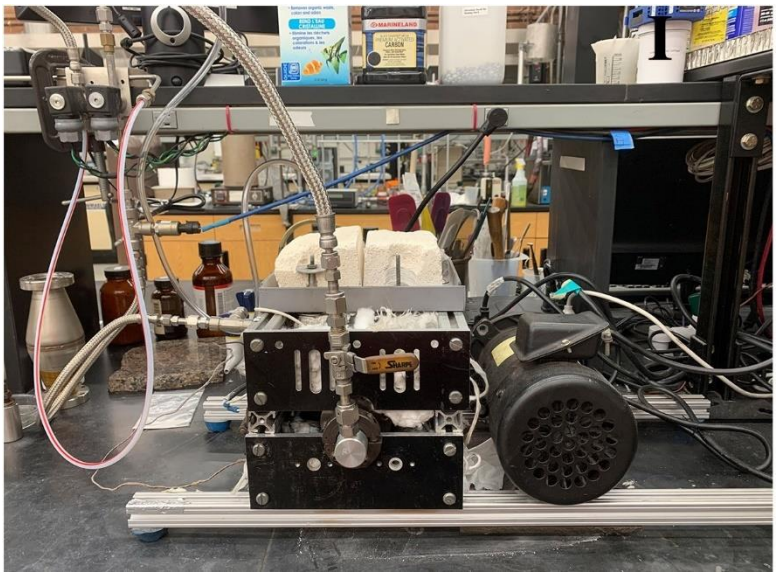

Figure 6: A pebble mill reactor, consisting of a motor and chain, which rotates the vial and causes tumbling of the ball bearings. The pebble mill vial is situatued within a heated bed with the capabilities for atmospheric control.

Solid, liquid, and gaseous reagents can be loaded within the pebble mill, since it is equipped with a gas inlet and outlet. The vial is gas-tight and is outfitted with specialized filters (stainless steel) to keep solids and liquids contained within the reaction vessel. Compared to the mixer mill, the pebble mill vial is best suited for a large quantity of milling media (ball bearings) since the bearings are tumbled and not shaken.

Figure 7: A stainless steel (left) and alumina (right) pebble mill vial, with their respective ball bearings. Two flanges (bottom) are used to close each end of the vial. Two filters (center in petri dish) are placed between the vial end and a flange on each side to prohibit reagents from exiting the reaction zone. O-rings (orange) seal the vial at the flange. Six bolts secure the flanges to the vial on each side. A threaded hole in the center of each flange accomodates for a gas inlet and outlet.

1.1.2.3 Reactor Material and Media

Reaction vessels can be constructed out of a wide range of materials, so long as the desired vial shape can be machined. A few examples of vial materials are shown in Figure 8. Changing the vessel material can serve many purposes. For example, stainless steel reaction vessels tend to cause metal contamination, which can be undesirable for catalytic reactions, since these metals can act as catalysts themselves. For mechanical synthesis reactions, metal contamination may interfere with characterization of the reaction products. Vial material can offer a selection of degrees of hardness during milling. A vial of softer material such as acrylic may be desired to dampen the

impact of the ball bearings, if a particular reaction calls for such conditions. Similarly, harder materials such as tungsten carbide can be used to increase the impact force of ball bearings.

Figure 8: Mixer mill vials made from various materials (from left to right) stainless steel with "hourglass" interior, stainless steel, acrylic with "hourglass" interior, acrylic, zirconia, tungsten carbide. Top image is a top view of the vial interior.

Choice of material for milling media (ball bearings) can be of greater importance than the material of the vessel itself. A wider selection of ball bearing materials are displayed in Figure 9. The material of the ball will determine its density, and thus, higher density balls will have a larger mass (assuming equal ball diameter). More massive bearings will impart a higher force with each impact (Equation 1.1). The acceleration of the ball will remain constant and depends on mill design specifications (i.e. shaking speed of arm).

$$F = ma \tag{1.1}$$

In addition, bearings of different sizes (Figure 10) can be employed to target specific impact force without changing the materials used. Reactions with high activation energies may call for high-density bearings made of tungsten carbide or stainless steel. On the other hand, for particle size reduction or mixing reagents within the vial, lighter media is ideal. Although the vial

and ball bearing material typically match, there is nothing constraining the use of different material ball and vial unless there is a possibility of contamination or damage of the equipment.

Figure 9: Ball bearings (0.5 in diameter) in a variety of materials.

Figure 10: Ball bearings for any material come in various sizes. Here are a selection of sized bearings made from stainless steel, and a single zirconia bearing (white). The largest 2 bearings are 0.75 in diameter.

A SPEX mixer mill clamp shakes at a speed of 1060 cycles/minute in a "figure-8" motion, with a distance of 5.9 cm traveled by the vial in the x direction (the vial's long axis) and 2.5 cm in the y direction (along vial radius). Thus, in a single "shake", the vial travels 11.8 cm in the x direction and 5 cm in the y direction. Using the discrete element method simulation software,

EDEM, we can approximate the average acceleration of a ball bearing within a standard stainless steel SPEX vial to be 212.36 m/s^2. This average is taken over all paths traveled by a ball bearing, including collisions with the side walls as well as collisions with the vial base and lid. Although collisions of bearings traveling from end to end of the vial may have the highest acceleration, in reality, side-wall collisions are extremely likely. Using this value of acceleration and implementing Equation 1.1, the approximate impact force of a 0.5 in diameter ball bearing can be estimated for a number of materials (Table 2). These estimations are for vial with dimensions like that of a standard SPEX vial with an interior volume of 65 mL.

Table 2: The calculated impact force of a 0.5" diameter ball bearing of various materials, that can be achieved in a 65 mL volume mixer mill vial.

Material	Density (g/cc)	Mass (g)	Impact Force (N)
Polypropylene	0.91	0.98	208.05
Torlon PAI	1.41	1.51	321.37
PTFE	2.13	2.29	485.36
Alumina	3.88	4.16	882.62
Zirconia	6.02	6.46	1371.12
440C Stainless Steel	7.75	8.31	1765.15
Tungsten Carbide	17.16	18.41	3908.38

1.2 Biofuels

Implementing biofuels is an important means by which to bridge the gap in the transition between fossil fuels and renewable energies. Although still hydrocarbon based, biofuels are produced from plant and animal waste materials, resulting in net carbon emissions that can potentially be near zero depending on crop choice. [21] A demand for biofuels would result in a demand for plant biomass material and thus, an increase in plant growth; plants which, while alive, would fascilitate uptake of atmospheric carbon dioxide by their natural life cycle and through soil regeneration. [22] Despite the benefits of some CO_2 sequestration, biofuels still produce fewer metric tons of CO_2 than that of gasoline combining all stages of production. [23] Figure 11 shows

the improvement in those numbers as efficiency in biofuel production increases. It is important to note that although biofuels are an important element of this story, electrification of vehicles still outsurpasses biofuels in terms of lowest emissions, as shown in Figure 12.

Some bio-derived fuels, referred to as “drop-in” fuels, are similar enough to conventional fuels that they can operate within current engine systems with no modifications. [24] Thus, they are ideal candidates for swift adoption. Biogasoline, biodiesel, and fuel additives (bioethanol) can all be produced from green wastes. However, each must be subject to the same characterizations and screenings as conventional hydrocarbon fuel, since they will likely exhibit the traditional problems associated with the burning of hydrocarbons.

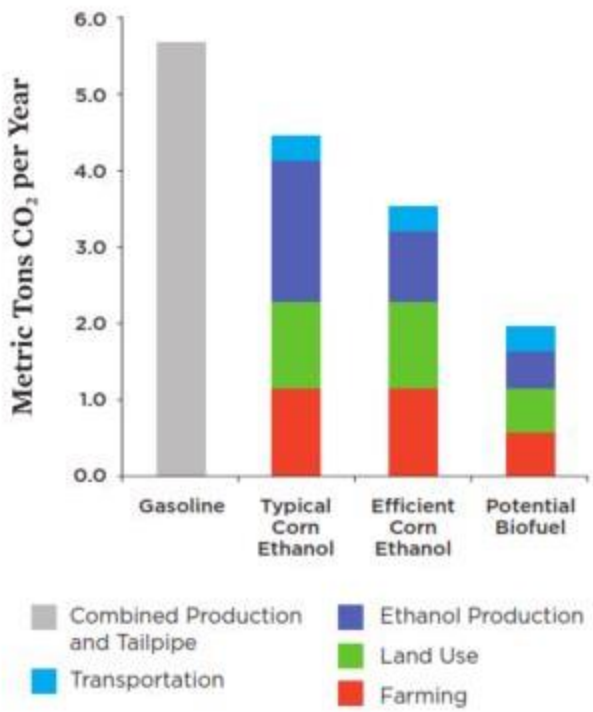

Figure 11: The emissions produced from typical corn ethanol without implementing efficient practices is less than that of gasoline. With more efficient agricultural practices these emissions can be even further reduced.

One such problem is the tendency of hydrocarbons to thermally degrade to carbon at high temperatures. Thermal degradation of conventional petroleum-derived fuels to form coke deposits

has been a topic of study for decades. [25] Jet fuel has long been known to degrade to form soot products, giving rise to problems in the aviation industry. [26] The chemical composition of biofuels and novel additives may vary from that of conventional fuels, and it is desirable to understand the effects they may have in a typical engine environment. Depending on the nature of these compositional differences (Table 3), thermal degradation may increase or decrease, especially with variations in compounds within different hydrocarbon classes (or functional groups). [27] The integration of new biofuels into existing systems relies on the ability to rapidly test and screen for promising biofuel candidates. It is desirable that testing for fuel properties such as soot formation need not require exceedingly long sampling times.

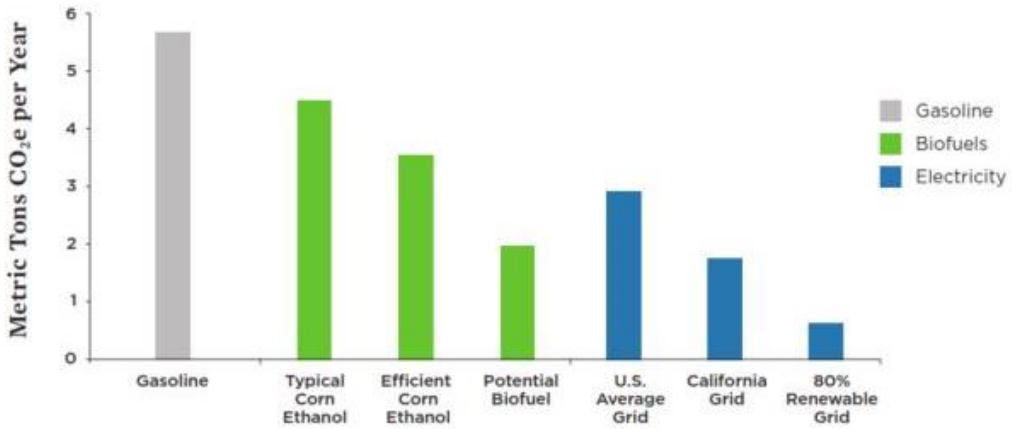

Figure 12: A comparison of gasoline-, biofuel-, and electically-powered vehicles. Gasoline emissions here include oil extraction and refining as well as tailpipe emissions. Biofuels have a high potential for emissions reductions as ethanol production efficiencies increase and responsible agriculture practices improve.

Table 3: The differences between gasoline, diesel, biogas, and biodiesel compounds.

	Gasoline	Diesel	Biogasoline	Biodiesel
Composition	• *C4 – C12* • Alkanes (paraffins) • Alkenes (olefins) • Cycloalkanes (Naphthenes)	• *C9 – C25* • Long chain • Aromatics	• *C6 – C10* • Short chain • Alcohols (ethanol)	• Long-chain • Fatty acid esters
Source	Petroleum (crude oil)	Petroleum (crude oil)	• Biomass (corn, algae) • Cellulosic plant waste	• Vegetable oil • Animal fats
Benefits	• Already implemented in modern engines		• Fewer emissions in production • "Drop-in" fuels are engine-ready	
Dis-advantages	• Non-renewable • Emissions from drilling • Emissions from combustion		• Increase food prices • Deforestation for agriculture use • Emissions from combustion	

1.3 Solid Pyrolant as an Energy Source for Space Missions

Space agencies are continually searching for innovative power solutions which would enable more flexibility when planning missions. [28-32] Energy sources powering space missions can range from highly energetic nuclear reactors to short-lifetime and low-output batteries (Figure 13). [33] Batteries are conventional and convenient, but require recharging if they are to be used over the course of weeks or months. In addition, batteries may not contain sufficient outputs to power all the instruments that may be desired on board, leaving scientists to prioritize some scientific equipment over others. This is now another constraint in addition to weight restrictions. Novel technologies such as regenerative fuel cells are a promising source of energy that could further diversify fuel options. [33, 34] For the Artemis program, NASA plans to widen the scope of their sustainable power generation through public prize competitions such as the Watts on the Moon Challenge, [35] launched in 2021, which intends to solve the problem of powering sustained living on the Moon.

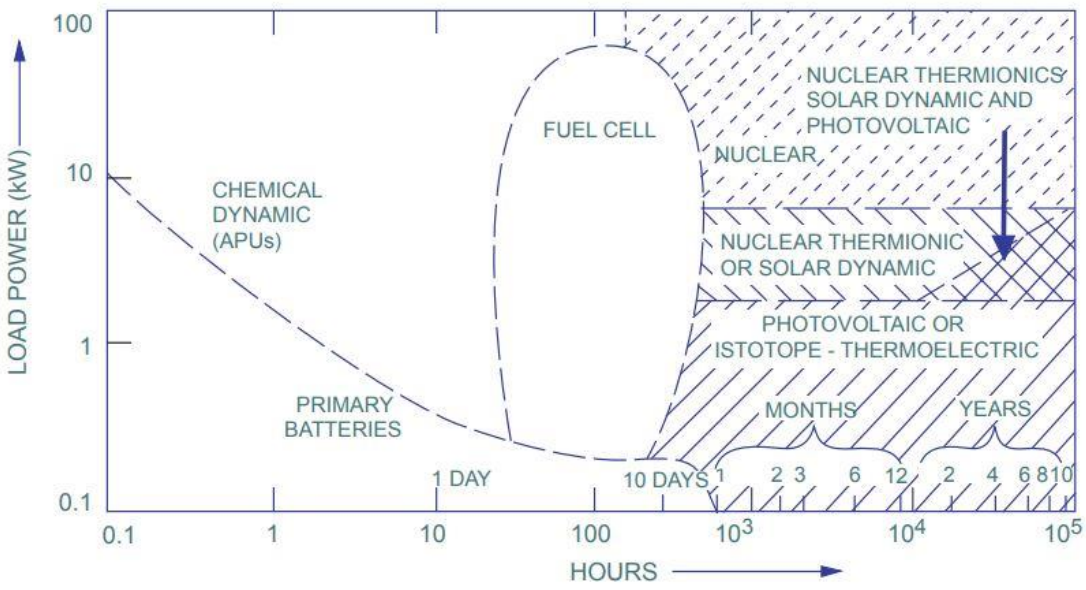

Figure 13: The range of power output and lifetimes of various energy sources for spacecraft. [33]

The proper selection of a power system is dependent on a multitude of variables, including the mission duration and the destination. Oftentimes, an energy source that has an appropriate lifetime for a mission may not be a suitable choice for the destination, or vice-versa. For example, solar arrays paired with lithium-ion batteries may operate well on missions as far as Mars, but this power quickly diminishes with increasing distance. [36] To date, only the Juno spacecraft, launched in 2011 to Jupiter, has successfully utilized solar panels to generate power at a distance greater than Mars (Figure 14). [36] However, Lucy, JUICE, and the Europa Clipper will soon travel to the Trojan asteroids, Jupiter, and Europa while utilizing large-area solar arrays to fuel their batteries. For the Europa Clipper, these solar arrays will span about 100 feet in order to receive sufficient sunlight. [37] Moreover, even some missions to the Moon and Mars may require alternatives to solar power in order to overcome specific challenges, such as cold temperatures at high altitudes, at the poles, or during winter season, as well as sunless locations. [38] Likewise, manned missions to any destination will require power other than solar. [39]

Figure 14: An illustration of NASA's Juno spacecraft, exhibiting its large solar arrays. Image credit: NASA.

1.3.1 Radioisotope Thermoelectric Generators (RTGs)

Radioisotope thermoelectric generators (RTGs) have powered several long-range, long-duration, and energy-intensive space missions, most of which are listed in Table 4. Pioneer 10-11, Voyager 1-2, Galileo, Cassini, New Horizons (Figure 15), and Dragonfly have destinations to the Jovian planets and beyond, which are too large of a distance from the sun for solar panels to operate efficiently. The Ulysses spacecraft, whose mission was to collect data from the Sun's poles, required a gravity-assist maneuver around Jupiter in order to escape the plane of the Solar System. [40] The detour to Jupiter ruled out the possibility of a solar-powered mission to study the Sun.

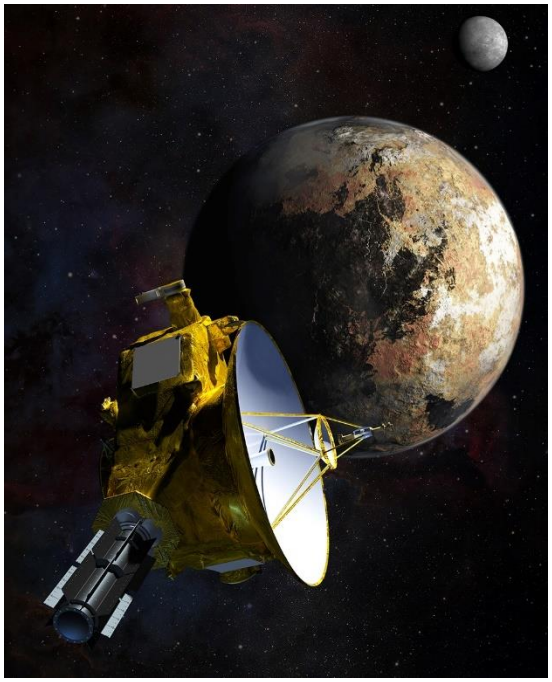

Figure 15: An illustration of New Horizons, an example of a spacecraft powered by an RTG. Image credit: NASA.

RTGs provide a thermal fuel source that also maintains ideal equipment operating temperatures onboard the craft. Their simple operation and low maintanence requirements make them suitable for unmanned missions to the most extreme environments in space and on Earth. RTGs operate continuously and independent of certain unavoidable circumstances such as variations in sunlight, temperature, dust, and radiation. [39]

Table 4: List of spacecraft powered by a radioisotope thermoelectric generator.

Spacecraft	Mission Destination	Launch Year	Years Active	RTG Type	Isotope	Class
Apollo 12 – 17	Moon	1969-72		SNAP-27	Pu-238	N/A
Pioneer 10	Jupiter	1972	31	SNAP-19	Pu-238	N/A
Pioneer 11	Jupiter/Saturn	1973	22	SNAP-19	Pu-238	N/A
Viking Landers 1, 2	Mars	1975		mod. SNAP-19	Pu-238	Flagship
Voyager 1, 2	Interstellar Space	1977	43	MHW-RTG	Pu-238	Flagship
Galileo	Jupiter	1989	14	GPHS-RTG	Pu-238	Flagship
Ulysses	Sun	1990	19	GPHS-RTG	Pu-238	N/A
Cassini	Saturn	1997	20	GPHS-RTG	Pu-238	Flagship
New Horizons	Pluto/Kuiper Belt	2006	15	GPHS-RTG	Pu-238	New Frontiers
Curiosity Rover	Mars	2011	10	MMRTG	Pu-238	Flagship
Perserverance Rover	Mars	2020	1	MMRTG	Pu-238	Flagship
Dragonfly	Saturn	2026	0	MMRTG	Pu-238	New Frontiers

CHAPTER 2: MECHANICALLY ENHANCED CATALYTIC REDUCTION OF CARBON DIOXIDE OVER DEFECT HEXAGONAL BORON NITRIDE

This work is reprinted (adapted) with permission from K.L. Chagoya, D.J. Nash, T. Jiang, D. Le, S. Alayoglu, K.B. Idrees, X. Zhang, O.K. Farha, J.K. Harper, T.S. Rahman, R.G. Blair, Mechanically enhanced catalytic reduction of carbon dioxide over defect hexagonal boron nitride, Sustainable Chemistry and Engineering (2021), 10.1021/acssuschemeng.0c06172.

2.1 Introduction

In the last decade, the large-scale release of carbon dioxide (CO_2) into the atmosphere has resulted in great international concern for our climate and widespread action to curb its release. Carbon dioxide is the main component of all combustion products produced in power generation and transportation. As consumer demands increase, the production of CO_2 will also increase. Global carbon dioxide emissions have been increasing, and each recent year yields a new record high. In 2018, CO_2 emissions again hit a record high at 36.7 gigatons. [41] The emission reduction of this greenhouse gas is of critical importance to the world climate. Popular approaches for the reduction of CO_2 emissions involve sequestration [42], electrochemical reduction [13], and homogeneous [14] as well as heterogeneous [15, 16] reduction. However, each of these approaches has disadvantages. Sequestration is limited to available space, electrochemical reduction is energy intensive, homogeneous reduction utilizes catalysts that can be difficult to recover, and heterogeneous catalysts are typically transition metal based. The most popular transition metals (save iron) utilized are not abundant.

Here we present a new approach for decreasing CO_2 emissions by implementing a heterogeneous catalyst produced from abundant elements to chemically reduce waste CO_2 and

produce valuable products. This approach facilitates reuse of the catalyst and allows the process intensification needed for industrial utilization. Reduction of carbon dioxide to useful molecules presents an attractive solution by providing economic incentive for capturing and utilizing CO_2 instead of disincentives for CO_2 release. This combination of both encourages CO_2 to be viewed as a raw material and not as a waste gas.

Although carbon dioxide is a combustion product there are enthalpically favored pathways to usable molecules. A reductant gas, such as hydrogen, that can be produced using renewable energy offers a potential solution to realizing value-added molecules from CO_2. Currently, most hydrogen is produced by steam reforming, and advances in water splitting catalysts may make hydrogen production greener. [43] The simplest reaction is the addition of molecular hydrogen (H_2) across a carbonyl bond (C=O) in CO_2. This produces formic acid by Equation 2.1.

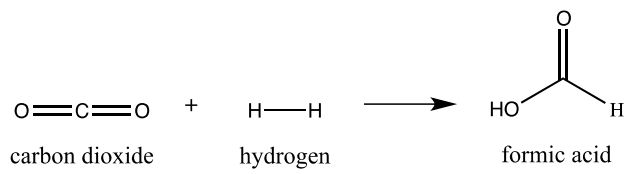

(2.1)

The forward reaction is enthalpically favored below the boiling point of formic acid (-31.59 kJ/mol, 100.8 ˚C). The reverse reaction is favored above the boiling point of formic acid (-14.9 kJ/mol). Furthermore, reduction of formic acid to methanol (Equation 2.2) is favored below the boiling point of formic acid (-99 kJ/mol) as well as above its boiling point (-64.1 kJ/mol).

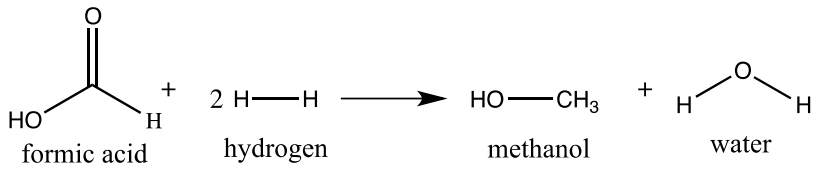

(2.2)

A forthcoming paper shows that the reaction mechanism proceeds through the formation of formic acid. [44] Hexagonal boron nitride has the potential to catalyze multiple reactions, as multiple defect types are possible (Figure 16). These defects can produce quite different chemical environments, from the Lewis acidity of a nitrogen vacancy (V_N) to the Lewis basicity of a boron vacancy (V_B). In fact, boron nitride has been shown to be catalytically active for hydrogenation under reductive conditions [17] and dehydrogenation under oxidative conditions. [45] Although oxidative dehydrogenation may be due to B-O species formed *in situ*[46], both hydrogenation and dehydrogenation take place on defect sites. [17, 45] We have found that these defect sites are active for catalyzing the reactions outlined in Equations 2.1 and 2.2 with localized electronic structures favoring CO_2 binding and carbonyl bond activation. These defect sites are conveniently introduced into the boron nitride structure via the application of mechanical force.

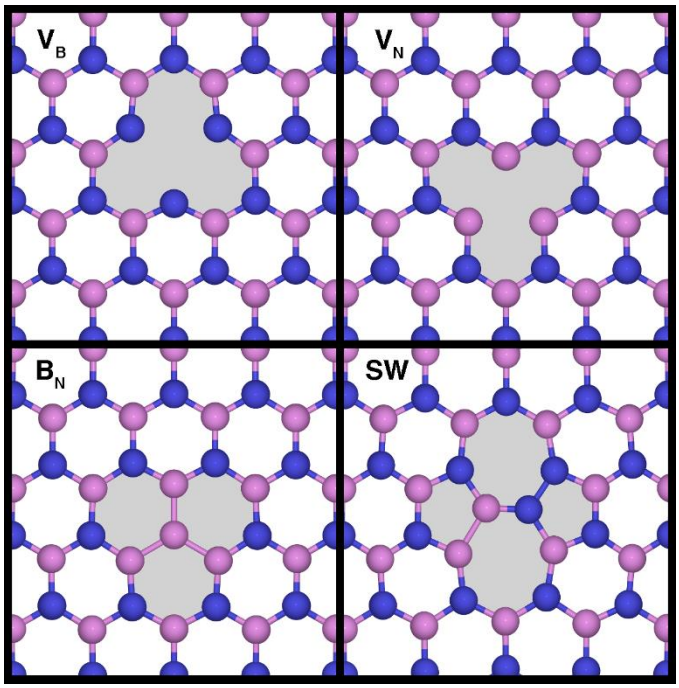

Figure 16: Four defect structures in BN were studied. These are (from top left to bottom right): a boron vacancy (V_B), a nitrogen vacancy (V_N), boron substitution for nitrogen (B_N), and 90° rotation of a BN bond, aka Stone-Wales defect, (SW). Blue and pink spheres represent nitrogen and boron, respectively. The light-gray backgrounds indicate the defect areas. As shown in Ref. 19, they are potential defected sites with affinity towards chemisorption. Table 8 summarizes binding energies calculated for CO_2 and H_2 (this study) and those for ethane and propene. Because the binding energy of CO_2 to nitrogen vacancies (V_N) is on par with olefin binding energies and strength of binding energy of CO_2 and H_2 are similar, the V_N site has been identified as the most likely catalytic site for olefin hydrogenation.

The use of mechanical force to achieve CO_2 reduction to methane has been previously demonstrated over MgO supported Ru/Ni/Fe catalysts. [47] Milling during hydrogenation was demonstrated to reduce the activation energy of the process and increase the production of methane. [47] This study found no advantage to pre-milling whereas we have found pre-milling significantly reduces the induction period for the onset of catalysis. [17]

Reduction of carbon dioxide in this way provides an economic incentive for capture and utilization of waste CO_2 as a profitable raw material. This could be instrumental in reducing CO_2 atmospheric emissions while mitigating the costs associated with control of these emissions.

2.2 Experimental

2.2.1 Preparation of dh-BN

Pristine *h*-BN (PCTF5 grade) supplied by Saint-Gobain Ceramic Materials was dried under dynamic vacuum at 400˚C for 20 hours then transferred to an argon-filled glovebox. In a 65 mL zirconia milling vial with (1) 20 mm diameter zirconia milling media (ball bearing), 3 g of dry *h*-BN was milled for 1 hour in preparation for hydrogenation. For uptake experiments, milling times ranged from 30 minutes to 4 hours. Milling was performed in an 8000M SPEX CertiPrep mill. All milling vials were loaded under argon. A silicone o-ring and custom clamp were used to ensure the vial was gas-tight during high energy activation. The boron nitride power is handled using plastic tools to eliminate contact with metal.

2.2.2 Mechanocatalytic Batch-Mode Hydrogenation Reaction

CAUTION! Hydrogen presents a significant hazard. The flammability limit of hydrogen in air is between 4 % and 75%. [48] Hydrogen burns with a blue nearly invisible flame. Engineering controls and safe operating procedures must be in place before proceeding. In this work all apparatus are thoroughly purged of air before admission of hydrogen. Hydrogen transfer lines are composed of 303 stainless steel or nylon (which has a low hydrogen permeability [49]). Hydrogen tanks have flash arrestors and excess flow valves between the regulator and the application. During an experiment, all materials in the vicinity are either non-flammable or ignition resistant.

In an argon-filled glovebox, 2.5 g of *dh*-BN was loaded into the stainless-steel batch-mode reactor (Figures 17, 18, and 19) containing 440C stainless steel, spherical milling media (ball bearings) of diameters and quantities: 19.1 mm (12), 12.7 mm (53) and 6.35 mm (86). The reactor

was sealed using silicone o-rings, removed from the glovebox, and purged with food-grade carbon dioxide. The reactor was then pressurized with food-grade CO_2 and H_2 at 20˚C to a total pressure of 685 kPa. The partial pressures of CO_2 and H_2 were 393 kPa and 292 kPa, respectively. Temperature was controlled using a CN3000 process controller and measured with 12 gauge K-type thermocouple in a copper sheath held against the rotating reactor by the spring tension of the thermocouple wire. Hydrogenation was performed at rotational speeds of 60 or 120 rpm at room temperature (20˚C), 120˚C and 160˚C.

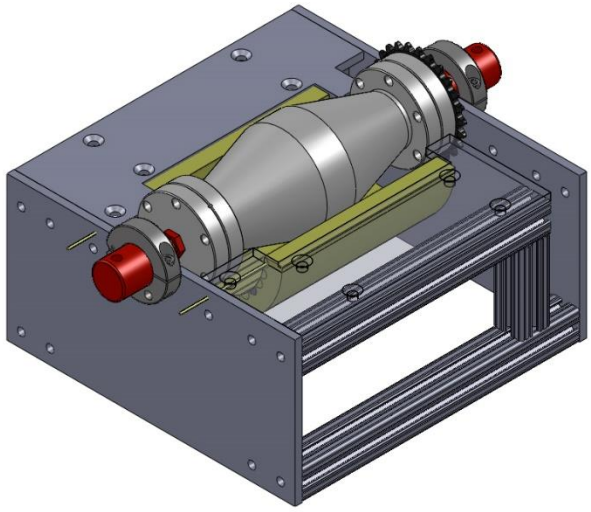

Figure 17: The mechanical reactor used for this study allows gaseous reactants to be introduced in a batch or flow configuration. Mechanical energy is supplied by rotation of the vessel (light gray) about rotary gas feedthroughs (red) by chain and spherical media inside the reaction vessel. Heat is applied from below (yellow) and above (not shown, mirror of below apparatus).

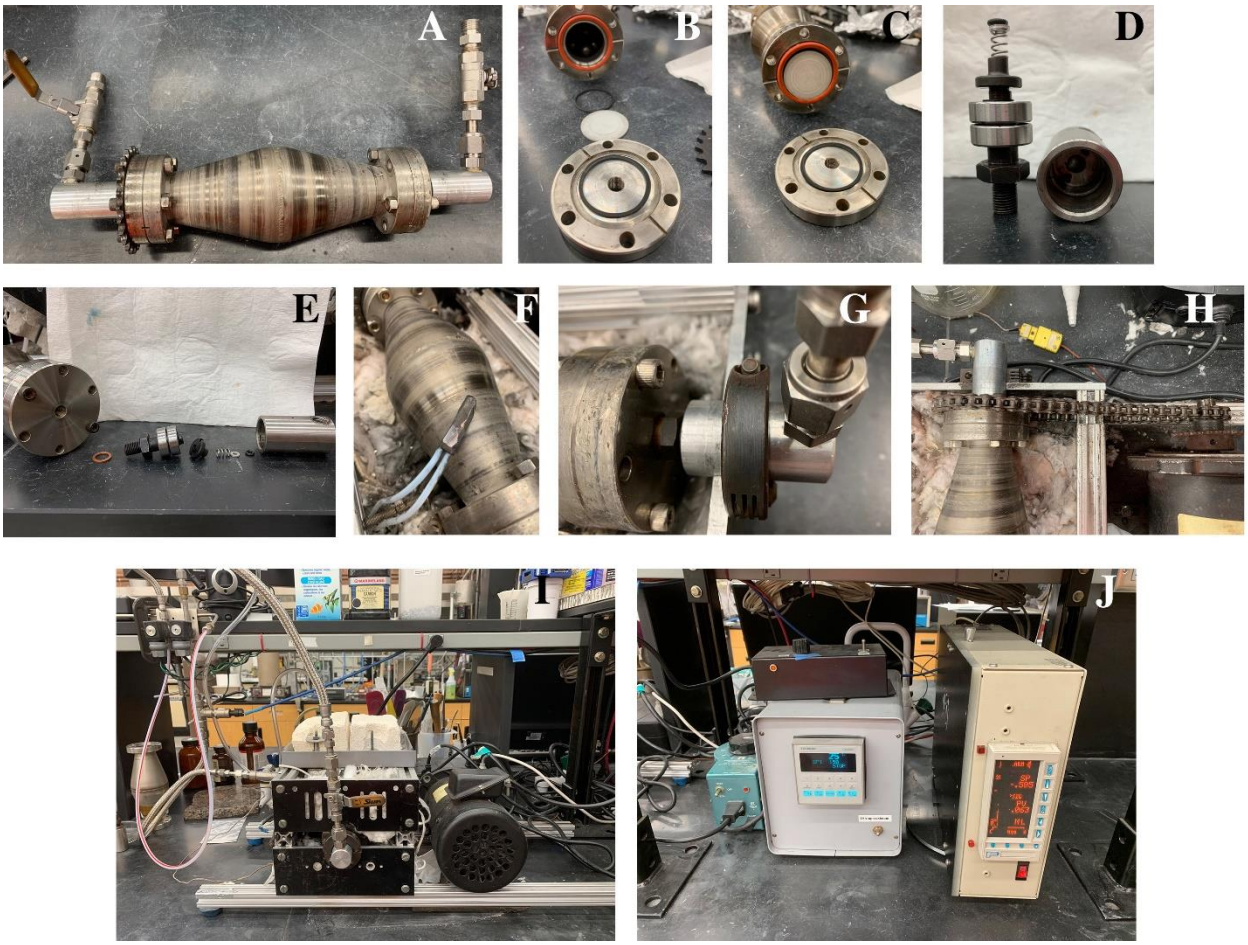

Figure 18: The moving portion of the mechanical reactor (A) is in the center. The rotary feedthroughs (left and right) are shown disassembled in D and E. A stainless steel fritted disc sits in a pocket machined in to the body and is sealed with Viton O-rings (B&C). The K-type thermocouple is housed in a copper sheath and held against the rotating mill body by the spring tension of the thermocouple wire (F). The rotary feedthrough bodies are held to the rigid case by a collar clamp fatened to the case (G). Rotary motion is driven by a DC motor (I right). Motion is transferred by chain and sprocket attached to the reactor end cap (H and A). The assembled mechanical and gas feedfeedthroughs are shown in I. The control electronics (J) include a Variac (left) to control current to the heating element, a pulse width modulated DC speed controller (top middle) to control rotation speed, an Omega CN6000 temperature controller (middle bottom) and a MicoMod process controller (right).

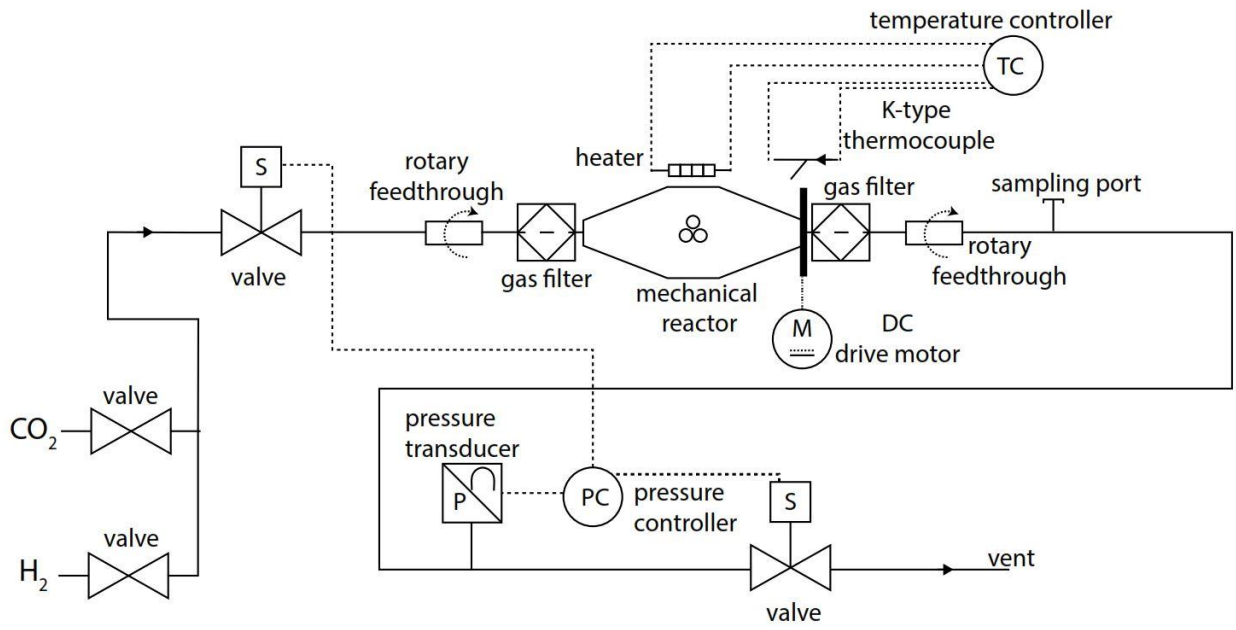

Figure 19: Batch-mode process and gas control topology is illustrated in this process and instrumentation diagram. Mechanical agitation is controlled by a variable speed DC motor. The Omega CN3000 temperature controller with K-type thermocouple on the reactor body is used for temperature control. Gas filters keep powdered catalysts from entering the rotary feedthroughs. Inlet and outlet solenoid valves allow pressure control via a MicroMod process controller with feedback from a pressure transducer. Process gases are introduced sequentially and the pressure is monitored during the entire processing time. The reaction products can be analyzed by syringe sampling through the sampling port or by venting through a sealed serum vial and GCMS analysis. Alternatively, a carbon trap can be placed near the sampling port to capture and concentrate reaction products.

2.2.3 Plug Flow Hydrogenation Reaction

One gram of *dh*-BN was mixed with 15 grams of 1 mm alumina beads and placed in a plug flow reactor (PFR). Reactions were performed at 20, 120, 200, 350, and 500 ˚C; 308.2 kPa, with CO_2 flow of 5 sccm and hydrogen of 5 sccm. A gas hourly space velocity (GHSV) of 414 was maintained for 17 hours. The product stream post-reactor was diluted with an argon flow of 13 sccm and this mixture was sampled every hour by gas sampling valve and analyzed using an Agilent 6890 GC with an HP PLOT U 30m x 0.32mm x 10µm column. Product detection was performed with an Agilent 5973N Mass Sensitive Detector (Figures 20 and 21).

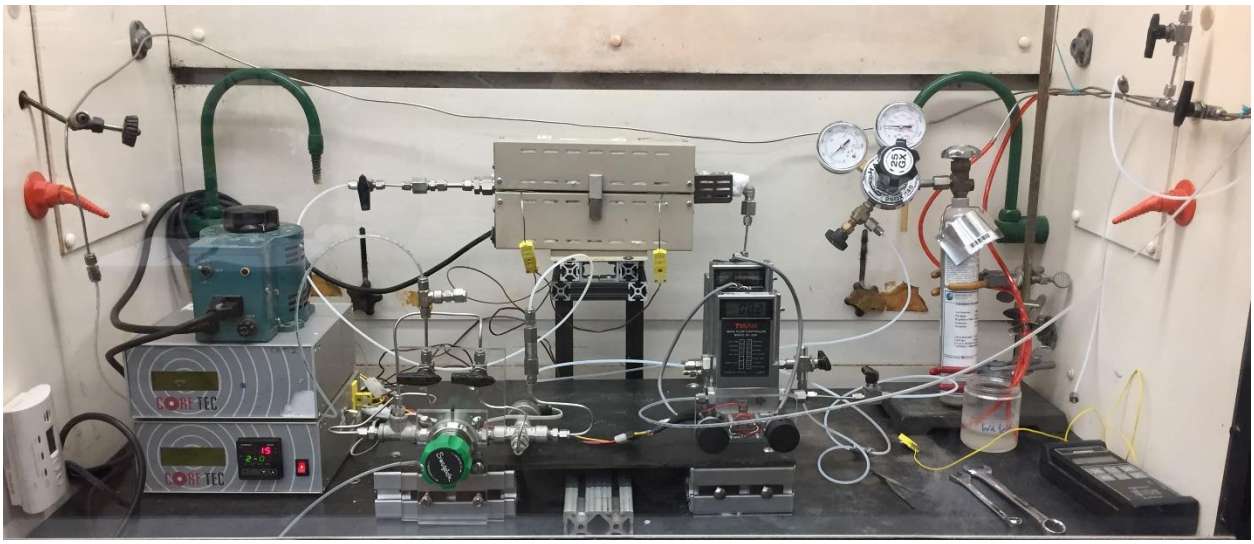

Figure 20: The plug flow reactor. Gas flow is from left to right. Center top is the furnace with packed bed installed. Temperature hysteresis is mitigated through the use of a Variac to supply heating power via the process controller. Three sheathed thermocouples (two front, one back) are connected in series to provide an average temperature across the length of the packed bed. The gas stream is directed out of the hood in a stainless steel gas path to the gas sampling valve of the Agilent gas chromatograph. GC vent gas is carried back to the hood via a stainless steel return line. Gas back-pressure is controlled manually with the green knob. Gas flow is controlled manually with the black knobs.

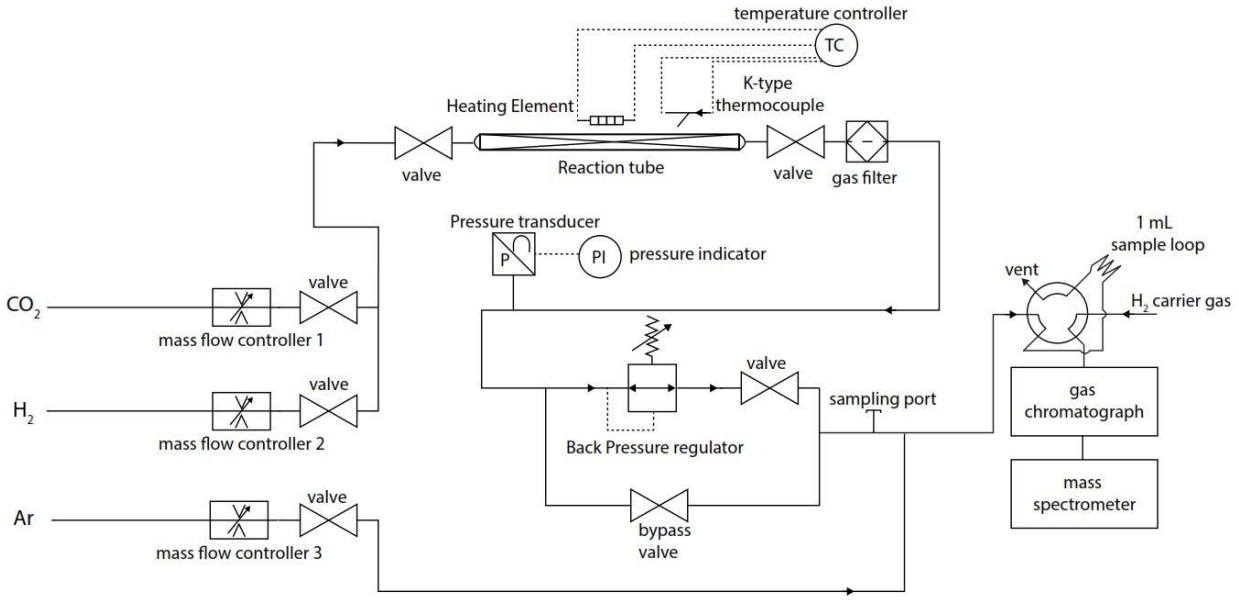

Figure 21: The plug flow reactor used for this study consists of three Tylan mass flow controllers with CO2 (10 sccm max), H2 (10 sccm max), and Ar (50 sccm max). CO2 and H2 are introduced into a packed bed column consisting of ½" 316 stainless steel tubing. All other gas tubing was 1/8" nylon. All gas connections are made with Swagelok fittings as well as national pipe tapered (NPT). The bed is held at temperature in a furnace controlled by an Omega CN9600 temperature controller with a sheathed K-type thermocouple for temperature feedback. A gas filter is used to keep catalyst powders from damaging the back-pressure regulator. The backpressure regulator is used to keep the catalyst bed at pressure. The bed pressure is set manually by adjusting the back-pressure regulator and observing the response of the pressure transducer. A bypass vale allows purging of the system before starting a reaction. A sampling port allows sampling of the reaction stream manually. The reaction stream is diluted with argon before entering a rotary sample valve with 1 mL sample loop. During operation, a sample is automatically taken at regular intervals and analyzed by GCMS.

2.2.4 CO_2 Mass Uptake

In an argon-filled glovebox, 1.5 g of *dh*-BN was placed into a glass vial of known mass. This vial is loaded into a pressurization cell, removed from the glovebox, and pressurized with either 372 kPa of CO_2 or 138 kPa each of CO_2 and H_2. The defect-laden BN was left to equilibrate for 48 hours before the pressurized cell was returned to the glovebox for a final mass measurement. Thermogravimetric analysis was performed on the recovered solids after the final massing.

2.2.5 Turnover Frequency and Turnover Number Estimations

Maximum turnover frequencies were estimated using the slope of the asymptote line of the pressure-time curves of each hydrogenation (Figure 26). The slope is taken between times 0 and 20 minutes and divided by four (4 moles of gas are consumed when one mole of CO_2 is hydrogenated). Turnover numbers were estimated by computing the ratio of the total number of moles of CO_2 converted in each cycle (from t = 0 to t = 1320 minutes) to the number of CO_2 adsorption sites determined by Equation 2.3.

$$TON = \frac{CO_2\ consumed\ (mol)}{active\ sites\ (mol)} \tag{2.1}$$

2.2.6 Density Functional Theory (DFT) Analysis

Calculations were carried out using the Quantum ESPRESSO package [50] employing the projector-augmented wave (PAW) [51, 52] and plane wave basis set methods. We utilized the vdW-DF2 functional [53] for describing electron exchange-correlation interaction. We set cut-off energy for plane-wave expansion at 45 Ry. We construct our simulation supercell with a 6×6 *h*-BN sheet with one N vacancy at the middle and a vacuum of 20 Å to decouple periodical image along the normal direction of the sheet. Considering the large size of supercell, we sampled the Brillouin Zone at the zone center. Structural relaxation is performed for all configurations until the forces acting on each ion are smaller than 0.0002 Ry/Bohr. To calculate reaction energy barriers, we use the Nudged-Climbing image method. [54] As V_N is identified as active site, calculations for reaction energies and barriers are carried out only for V_N defect *h*-BN.

2.3 Results

2.3.1 Defect Sites and Adsorption onto Boron Nitride

Evaluation of defect sites in *dh*-BN was performed by mass uptake experiments, TPD, and SSNMR. For all these analyses, *dh*-BN was kept rigorously oxygen- and moisture-free, to prevent blockage of defect sites.

It was found, from mass uptake experiments, that pristine, defect-free *h*-BN exhibited almost no CO_2 uptake while *dh*-BN produced through high-energy ball milling absorbed up to 5 mass% or 45.9 mg/g CO_2 (H_2O<20 ppm) at the relatively low pressure of 372 kPa. This is significantly better than other *h*-BN materials prepared specifically for CO_2 uptake. [55] Infrared spectra showed that adsorbed CO_2 (Figure 22) had a reduced bond strength as the asymmetric stretch (ν_3) was lowered in energy from 2349 cm^{-1} [56], for gaseous CO_2, to 2335 cm^{-1}. This reduction in bond energy is greater than that observed for CO_2 adsorbed onto ruthenium (2343 cm^{-1}) [57], a metal with known activity for CO_2 reduction. DFT calculations supported these observations by predicting a change in the O-C-O angle from linear to bent, suggesting a reduction in the C=O bond order and an increase in carbon sp^3 character. [58] Maximum uptake of CO_2 occurred at 1 hour of high-energy ball milling with subsequent decrease in CO_2 adsorption at longer processing times for these milling conditions. The resulting solid was stable under ambient conditions and heating above 100˚C was required to release the adsorbed CO_2. Temperature programmed desorption (TPD) analysis (Figure 23) indicates a binding site concentration of 81.1 µmole/g (all sites producing CO_2 or CO desorption). This is nearly two orders of magnitude smaller than previous olefin hydrogenation studies over *h*-BN defect sites produced in a similar manner. [17]

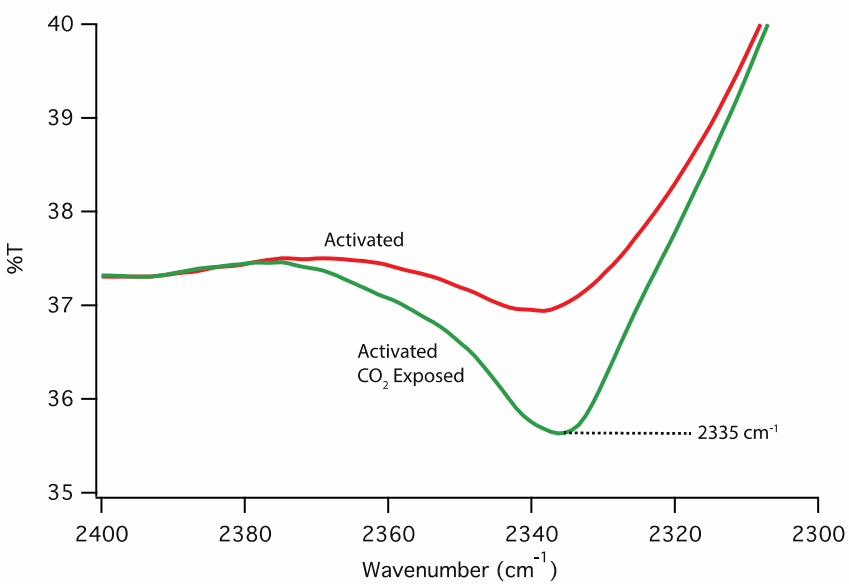

Figure 22: The infrared spectra of activated *dh*-BN as produced and exposed to 372 kPa of CO_2 shows increased signal due to CO_2 uptake. As the species is surface adsorbed, the C=O asymmetric stretch is missing the P and R branch and shifted to lower energy (from 2349 cm^{-1} shifted to 2335 cm^{-1}).

In addition to CO_2 desorption, CO, NO, and water were among the gases shown to desorbed from the *dh*-BN sample by TPD. Large desorption of mass 44 (CO_2) peaks are seen at temperatures 105˚C and 211˚C (Figure 23) whereas desorption of mass 28, belonging to either N_2 or CO (but predicted to be CO), occurs at temperatures 111˚C and 198˚C. Water desorbs increasingly after 200˚C. Although other materials show desorption of CO_2 at relatively low temperatures [59], the initial CO_2 desorption peak at 105˚C is on par with desorption peaks observed over zeolites with a similar second peak at 227 ˚C for Cs^+ exchanged zeolites [60] suggesting that the adsorption sites are of similar strength to the acid/base sites on ion exchanged zeolites. The desorption of CO_2 from CaO shows a peak at 227 ˚C [61] suggesting a similar basic surface character for the *dh*-BN site, Cs^+ exchanged zeolite, and CaO.

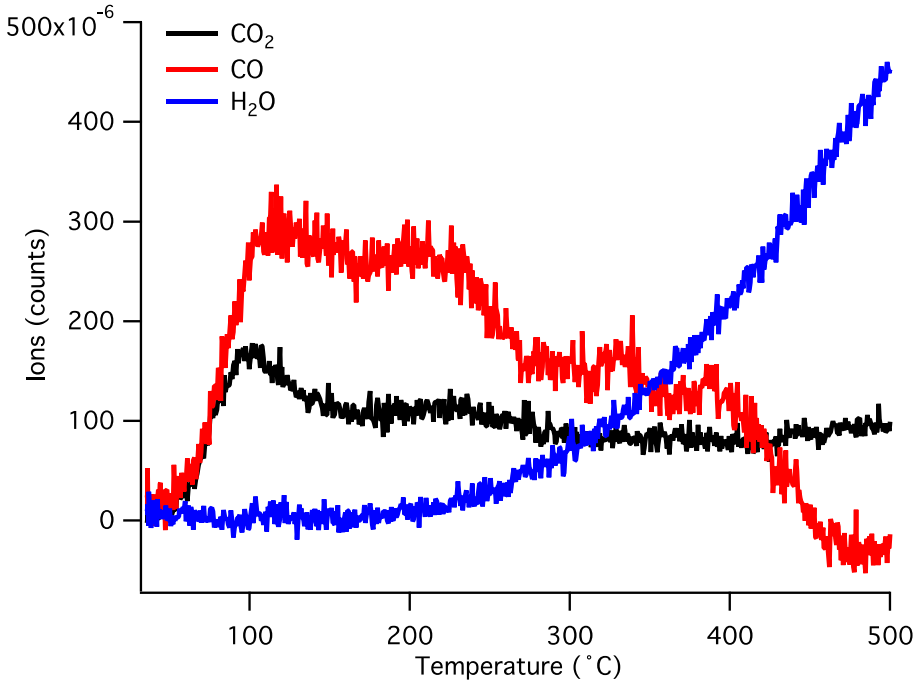

Figure 23: Temperature programmed desorption (TPD) of CO_2 adsorbed onto *dh*-BN shows desorption profiles of CO_2 and CO from different defect sites within the BN sheet, indicated by peaks.

Solid-state ^{13}C NMR spectrum of the $^{13}CO_2$ adsorbed *dh*-BN was acquired to further elucidate the environment of CO_2 bound to boron nitride. The NMR spectrum (Figure 24) was obtained after exposing *dh*-BN to > 99% isotopically labelled $^{13}CO_2$. A group of CO_2 resonances was observed near 155 ppm with an overall line width of approximately 15 ppm. This spectrum was well fit by a superposition of three resonances (Figure 25). Based on this fitting, the peaks at 161.7, 156.3, and 151.7 ppm are present in a ratio of 3.1:2.5:1.0, respectively. These lines observed are consistent with surface bound CO_2 because all the shifts differ significantly from the frequency of CO_2 in solution at 132.2 ppm. [62] Moreover, surface bound CO_2 would invariably be in very close proximity to ^{14}N, ^{10}B and ^{11}B nuclei and the resonances would thus be expected to broaden because these nucleides are quadrupolar. The fact that the observance lines are broad and differ from the expected shift of CO_2 is consistent with surface bound CO_2 at three distinguishable sites.

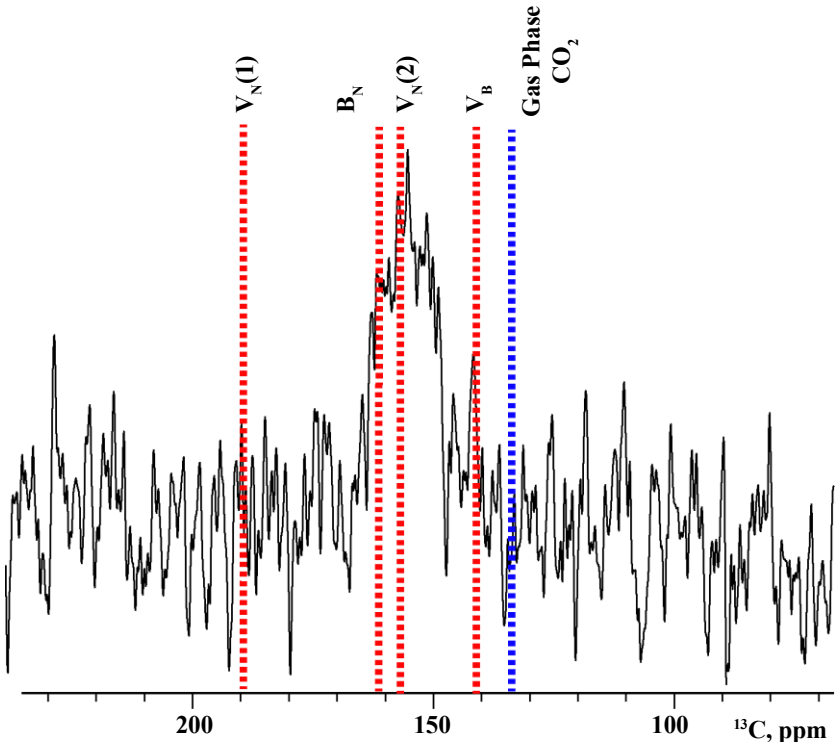

Figure 24: The ^{13}C spectrum of CO_2 bound to boron nitride. The red dashed lines represent theoretical shifts from four model binding sites. Theoretical shifts were computed at using the B3PW91/D95** level of theory. The blue dashed line represents the shift of gas phase CO_2.

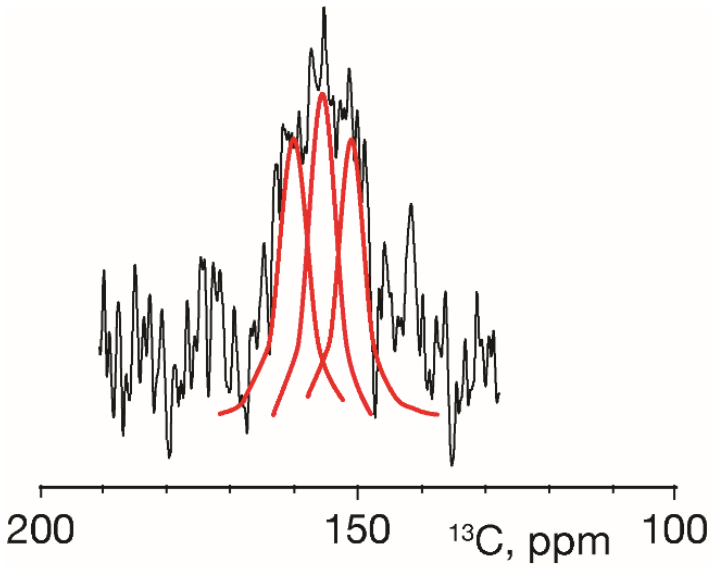

Figure 25: The ^{13}C spectrum of CO_2 bound to boron nitride. The spectrum is consistent with three unique CO_2 binding sites as indicated by the excellent fit to the spectrum from three model Lorentzian resonances.

2.3.2 CO_2 Reduction

Hydrogenation reactions in batch-mode run over fresh *dh*-BN resulted in complete reduction of CO_2 and formation of valuable products. For experiments run at temperatures 20°C and 120°C, turnover numbers (TON) were calculated to be 57 and 56 per cycle, respectively, with multi-cycle totals listed in Table 5. With each subsequent recycle, the catalyst shows reduced activity (Figure 26). This observed reduction in activity is accompanied by increasing discoloration (yellowing) of the BN from its original white and darkening with increased temperature (Figure 27). The calculations for TON, described briefly in the experimental, are obtained using Equation 3. The number of moles of active sites was obtained through TPD analysis, by determining the molar difference in adsorption and desorption of carbon-containing species. In this way, the determination of maximum active sites is specific to those sites having carbon dioxide affinity. Tables 6 and 7 report the TON values after each recycle of the catalyst at 20°C and 120°C.

Table 5: TON and TOF numbers for CO_2 hydrogenation over *dh*-BN catalyst.

Mode	T/P (°C/kPa)	TON	TOF ($s^{-1}\cdot10^{-2}$)	Products	Analysis Method
Batch	20/685	289	1.52	methanol	GC/MS
	120/685	108	7.57	methanol	GC/MS
	160/685	-	-	formic acid	GC/MS *captured via trap
Plug flow	20, 120, 200, 350, 500/308.2	0	-	none	-

Plug flow implementation of *dh*-BN in a packed bed was investigated at 20, 120, 200, 350, and 500˚C in a system with (dynamic) a without mechanical agitation (static). No measurable amounts of hydrogenation products were observed. High-intensity vibratory agitation of the PFR bed was not sufficient to facilitate the reaction. GC/MS analysis of the mechanocatalytic batch

reactor revealed that hydrogenation reactions run at temperatures 20˚C and 120˚C formed methanol while reactions at 160˚C produced formic acid.

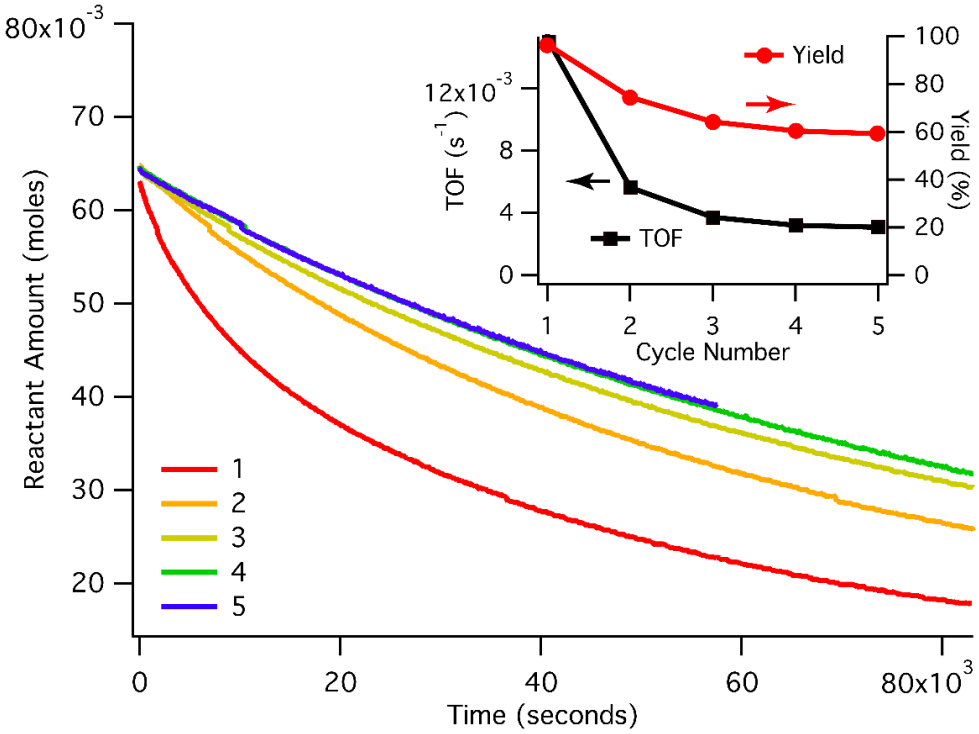

Figure 26: The reduction of CO_2 by H_2 for multiple recycles of the catalyst decreases with each recycle, ultimately reaching a stable state as the BN surface experiences coking. This reduction at 20˚C occurs at a rate comparable to olefin hydrogenation with decreasing TOF (inset) for each recycle of the catalyst.

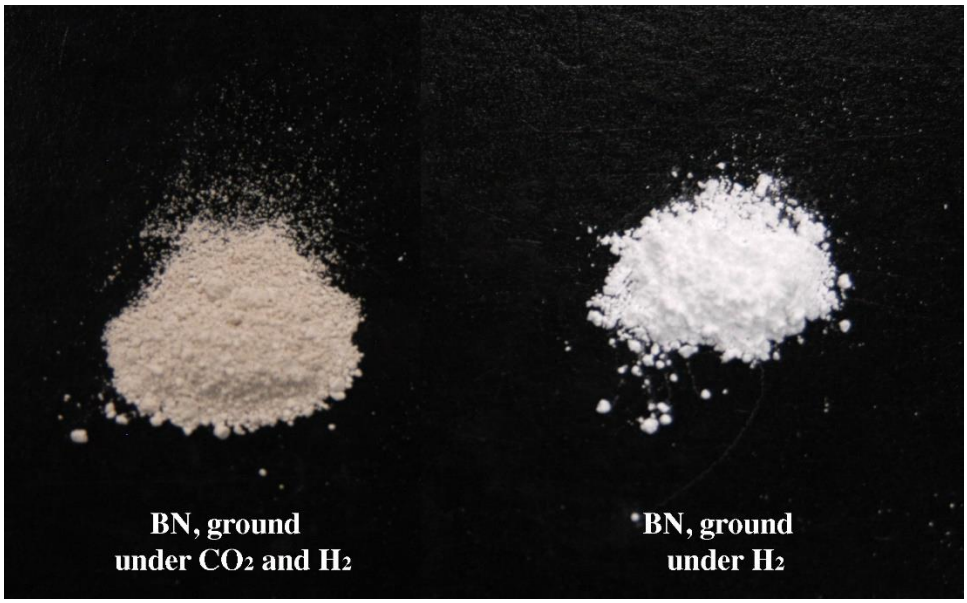

Figure 27: Defect-laden *h*-BN processed under H_2 and CO_2 produced low volatility side products that colored the catalyst. The same catalyst processed under hydrogen alone did not develop this color.

Table 6: Estimation of TON and Yield at 20 °C.

	Cycle					Notes
	1	2	3	4	5	
P start (psig)	69.464	70.398	70.132	70.332	70.070	Starting pressure
P end (psig)	19.935	29.066	33.873	35.523	42.398	Pressure at 22 h, Cycle #5 at 16 h
P start (psia)	84.16	85.09	84.83	85.03	84.77	
P end (psia)	34.63	43.76	48.57	50.22	57.09	
P_H_2 start (psia)	34.73	35.20	35.07	35.17	35.04	
P_CO_2 start (psia)	49.43	49.90	49.76	49.86	49.73	
Temperature (K)	293.15	293.15	293.15	293.15	293.15	
Moles of H_2	0.0347	0.0352	0.0351	0.0352	0.0350	Purge with hydrogen first so hydrogen pressure in psia is 1/2 psig + 14.7 psi
Moles of CO_2	0.0494	0.0499	0.0498	0.0499	0.0497	
Total (moles)	0.0842	0.0852	0.0849	0.0851	0.0848	
Final gas (moles)	0.0346	0.0438	0.0486	0.0502	0.0571	
Consumed (mol)	0.0495	0.0413	0.0363	0.0348	0.0277	$CO_2 + 3H_2 \rightarrow CH_3OH + H_2O$. Every 4 moles are consumed, 1 mole of CO_2 is hydrogenated.
Consumed CO_2	0.0123	0.0103	0.0090	0.0087	0.0069	
Consumed H_2 (mol)	0.0371	0.0310	0.0272	0.0261	0.0207	
Yield (%)	**100**	**88.07**	**77.55**	**74.24**	**59.24**	Yield = $\text{Consumed } H_2 / \text{Moles of } H_2$
Max active site	0.000203					From TPD analysis
TON	57	58	58	58	58	Total **TON = 289**

Table 7: Estimation of TON and Yield at 120 ºC.

	Cycle		Notes
	1	2	
P start (psig)	69.066	70.027	Starting pressure
P end (psig)	25.335	38.134	Pressure at 22 hr, Cycle #5 at 16 h
P start (psia)	83.76	84.72	
P end (psia)	40.03	52.83	
P_H_2 start (psia)	34.53	35.01	
P_CO_2 start (psia)	49.23	49.71	
Starting Temp. (K)	297.15	327.15	
Ending Temp. (K)	385.15	385.15	
Moles of H_2	0.0341	0.0314	Purge with hydrogen first so hydrogen pressure in psia is 1/2 psig + 14.7 psi
Moles of CO_2	0.0486	0.0446	
Total (moles)	0.0827	0.0760	
Final gas (moles)	0.0305	0.0402	
Consumed (mol)	0.0522	0.0357	$CO_2 + 3H_2 \rightarrow CH_3OH + H_2O$. 4 moles of gas are consumed when 1 mole of CO_2 is hydrogenated $\text{Yield} = \frac{\text{Consumed } H_2}{\text{Moles of } H_2}$
Consumed CO_2	0.0130	0.0089	
Consumed H_2 (mol)	0.0391	0.0268	
Yield (%)	**100**	**85.36**	
Max active site	0.000203		From TPD analysis
TON	56	52	Total **TON = 108**

Thermogravimetric analysis (TGA) of the recycled *dh*-BN showed continuous linear mass loss up to temperatures of 800˚C with an overall mass loss of 32.9% (Figure 28). TGA of *dh*-BN exposed to the potential reaction products of methanol, formic acid, and acetic acid shows strong affinity for the carboxylic acids with >50% mass loss from the free-flowing dry powder initially produced (Figure 29). Tandem TGA-GC/MS results showed the desorbed gases are largely CO_2 and acetic anhydride at higher temperatures (Figure 30).

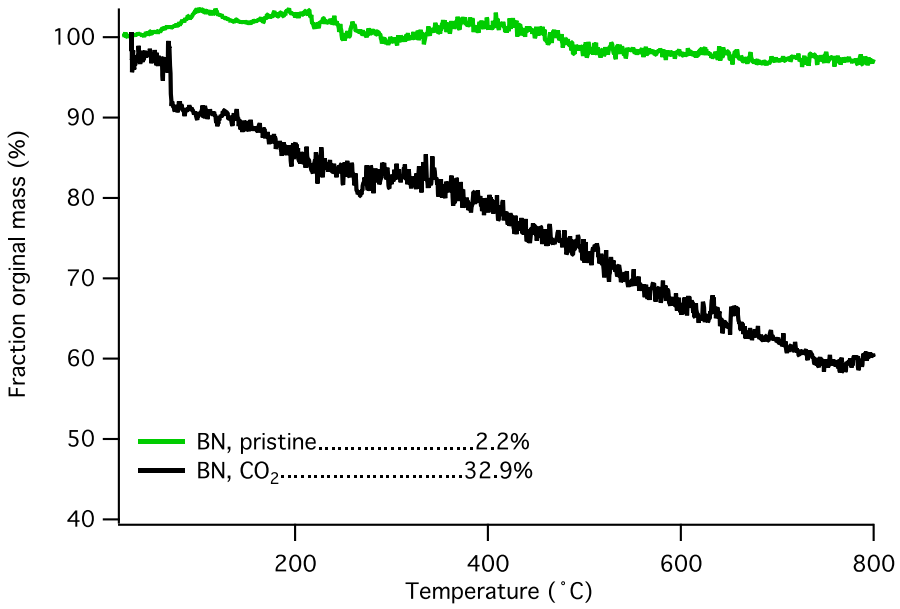

Figure 28: Thermogravimetric analysis (TGA) of spent catalyst. The spent catalyst picks up a large fraction of carbonaceous materials. The spent catalyst is colored and after thermogravimetric analysis returns to white indicating the color is not due to steel incorporation.

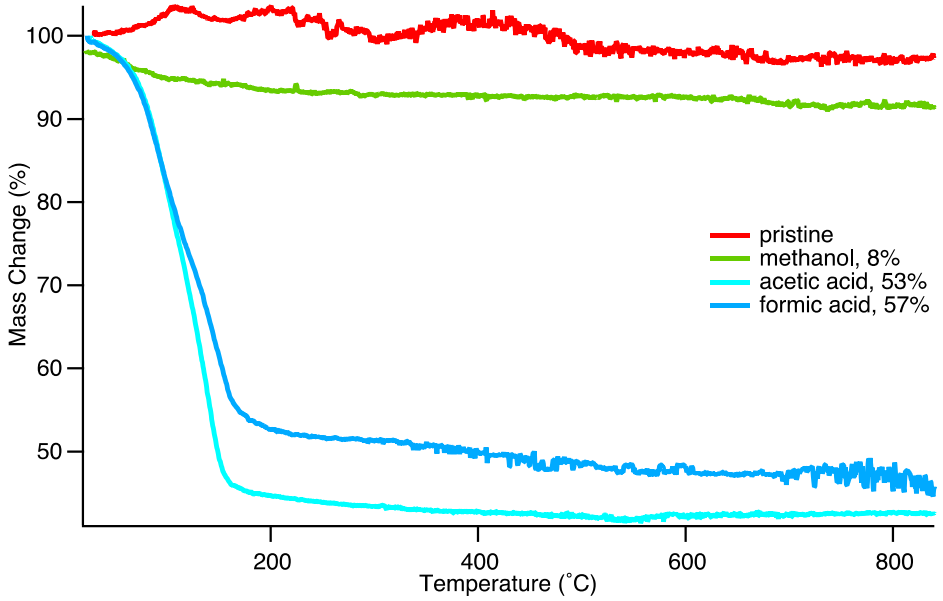

Figure 29: As received, *h*-BN shows little mass loss on heating (pristine). Powders of defect-laden *h*-BN (*dh*-BN) were soaked in pure reaction products and held at room temperature in air until dry free-flowing powders were obtained. The material has a strong affinity for formic and acetic acid and a weak methanol affinity. Complete carboxylic acid desorption was achieved near 165 ˚C suggesting that a portion of the mass loss observed in spent catalyst may be due in part to adsorbed products.

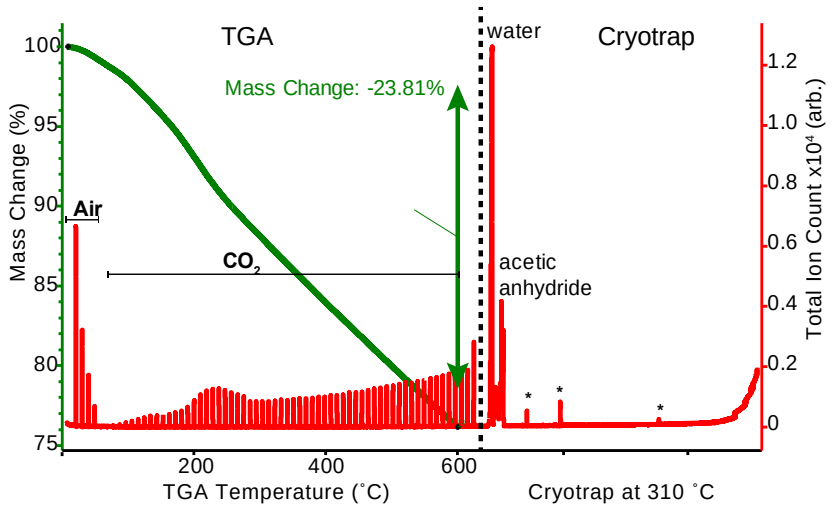

Figure 30: Tandem GC-MS-TGA of spent catalyst shows uniform CO_2 release up to 600 ˚C with acetic anhydride collected in a cryotrap during heating. The peaks marked with the (*) are due to column contaminants.

X-ray photoelectron spectroscopy (XPS) revealed C=O on the surface of recycled *dh*-BN (Figure 31) showed the carbon 1s region. Beside the strong intensity peak at around 284 eV for both as received and spent *h*-BN, which was due to adventitious carbon, the additional peak at 288.5 eV indicated that carbon in the form of carbonyls was deposited on the catalyst surface.

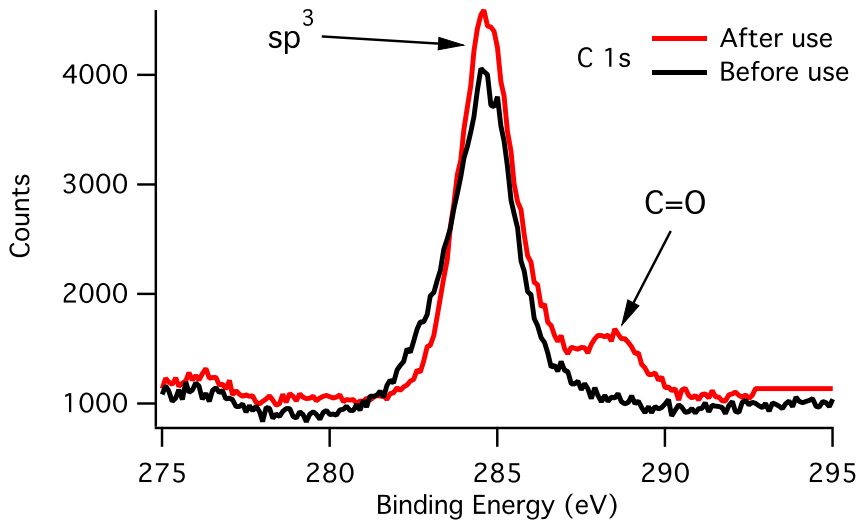

Figure 31: X-ray photoelectron spectroscopy (XPS) of the C 1s region shows the incorporation of carbonyl compounds on the spent catalyst surface.

In addition to XPS, FTIR spectra of spent catalyst showed a multitude of reaction side products on the *dh*-BN surface (Figure 32). Spectra showed evidence of unreacted adsorbed CO_2, and reaction side products. These include reaction with the BN sheet (B-C, B-O-H, and B-N-O), absorbed CO_2, and the formation of alkyne carbons or nitriles.

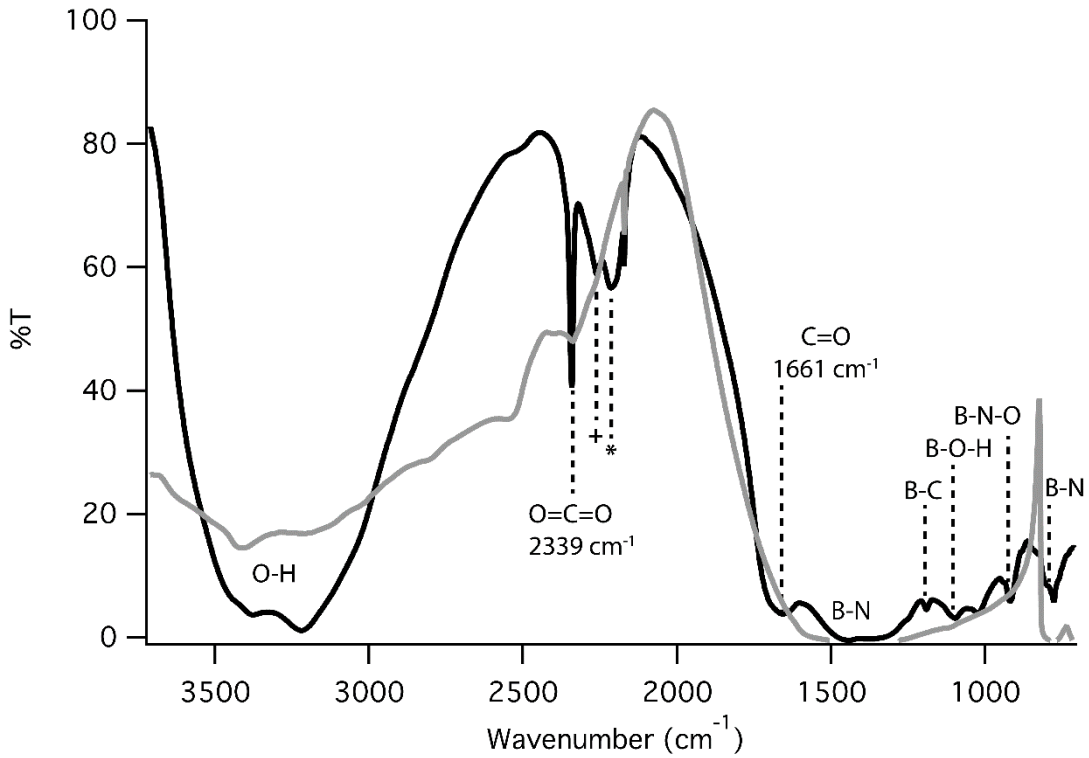

Figure 32: FTIR of pre-reaction *dh*-BN (gray) and spent *dh*-BN (black) catalyst shows significant amounts of carbon compounds. The peaks labeled + and * are either alkyne or nitrile stretches.

2.4 Discussion

2.4.1 Defect Sites and Adsorption onto Boron Nitride

The role of defect (or active) sites in the catalytic activity of solids have been the subject of many studies [63-67]. It is not uncommon for defect sites to be introduced into a material

through the application of force to increase or induce catalytic activity. Ball milling is one convenient method of defect site creation utilizing mechanical force. For boron nitride, the force required to introduce defect sites in the crystal lattice is 41.3 MPa (the compressive yield strength of the material). This criterion can be met in our preprocessing and in the mechanocatalytic reactor. These forces are not realized in a static or agitated plug flow reactor (PFR). Increased processing times should increase the concentration of defect sites present on the *h*-BN sheet and result greater activity. However, prolonged high-intensity ball milling leads to loss of activity as the sheet structure is lost to amorphitization. We observed this phenomena as a loss in CO_2 absorption capacity with increased processing time. Thus, there exists an optimum milling time where a maximum number of active sites are created and a maximum adsorption of gas is observed. Mass % uptake experiments show this optimum mill time to be 1 hour (Figure 33).

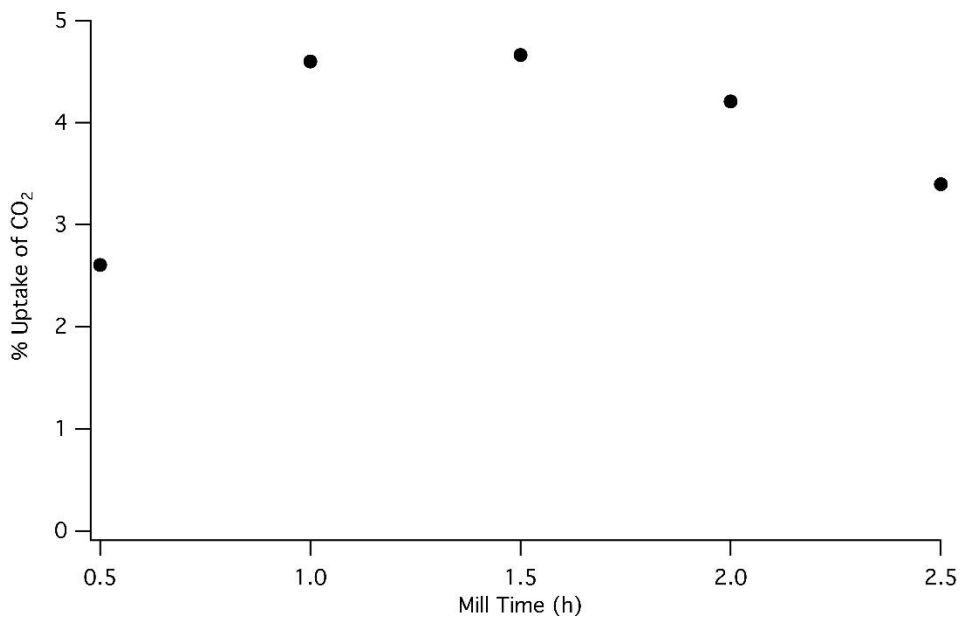

Figure 33: The amount of CO_2 absorbed by milled *h*-BN increases with processing time as defects are generated and increased surface area is realized. However, as processing continues amorphitization occurs and a loss in CO_2 capacity is observed.

BET analysis indicated enhanced CO_2 uptake for *dh*-BN and a surface area increase from 10 m^2/g ,for as received, to 135 m^2/g, for material processed 1 hour (Figure 34).

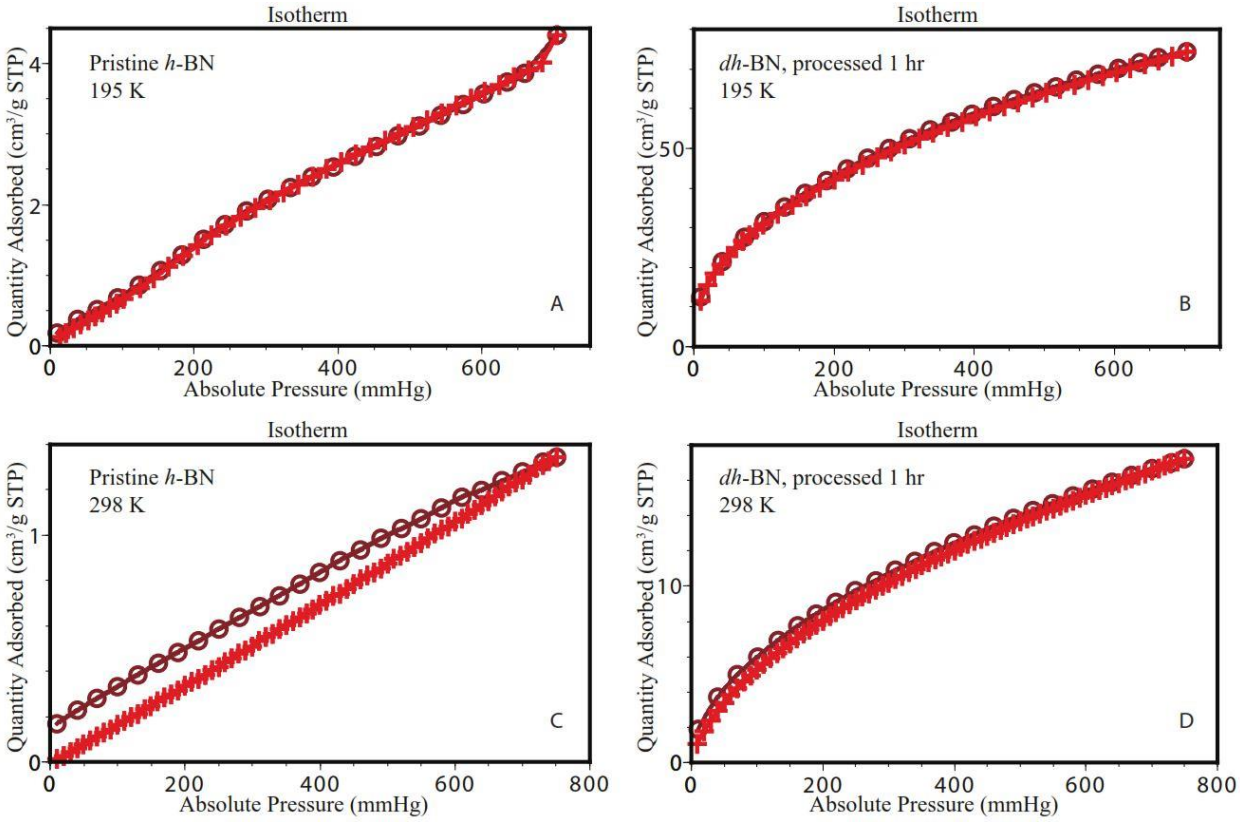

Figure 34: With a BET surface area of ~10 m2/g, as received *h*-BN is nonporous. Negligible CO_2 uptake was measured at 195 K and 298 K (A and C). Processing for 1 hour produces *dh*-BN with a BET surface area of ~135 m^2/g. Enhanced CO_2 uptake was observed at 195 K and 298 K (B and D).

Delamination and size reduction, after processing, is clearly observable in transmission electron microscopy images (Figure 35). Although milling reduced the starting materials crystallinity, there was still order in the c-direction (Figure 36). To alleviate amorphitization issues, continuous low-energy ball milling (via pebble mill) is utilized in tandem with hydrogenation to apply strain to the catalyst without amorphitization. This keeps the needed sheet structure for catalysis while providing a high-energy non-equilibrium surface for enhanced catalysis. This phenomena has been observed in systems other than BN. [67]

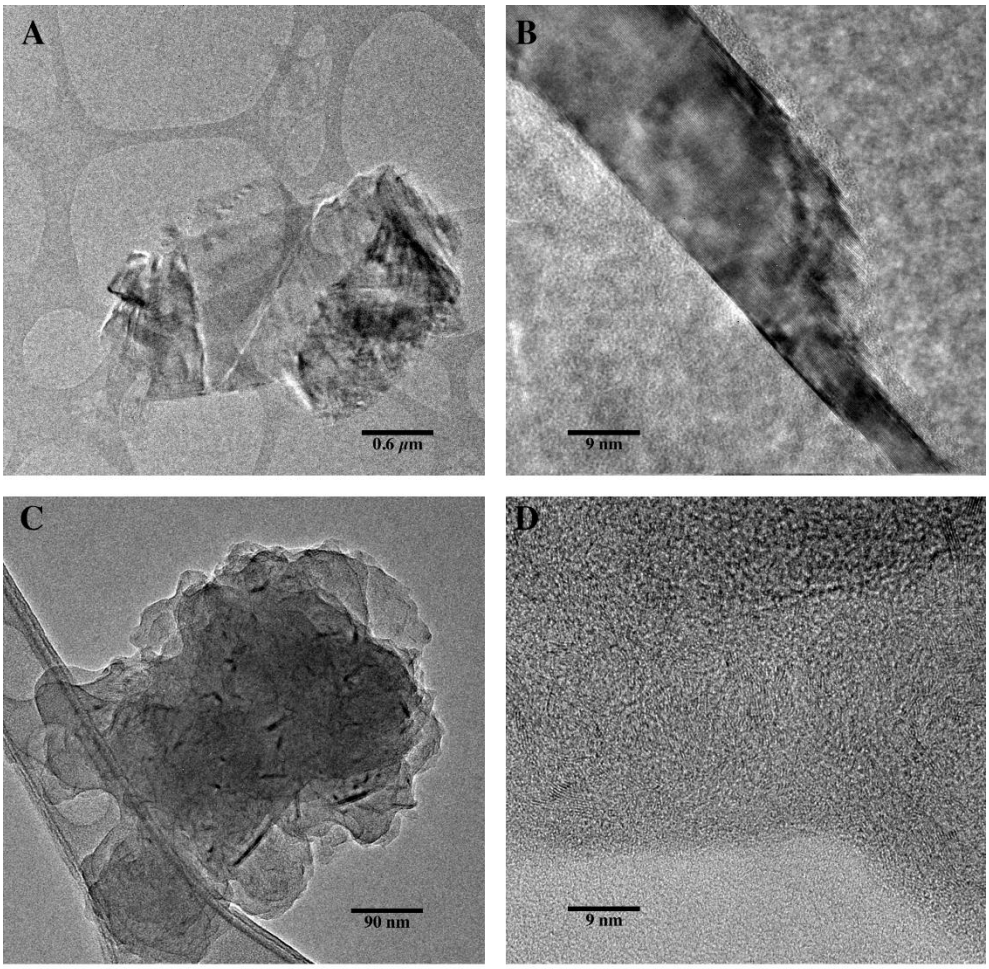

Figure 35: Transmission electron microscopy images of as received and 1 hour processed *dh*-BN. The as received material has large flakes (A) with well-ordered BN layers (B). The *dh*-BN consists of smaller and thinner flakes (C) with less order in the c direction. Delamination and curling of the BN sheet can be seen in C.

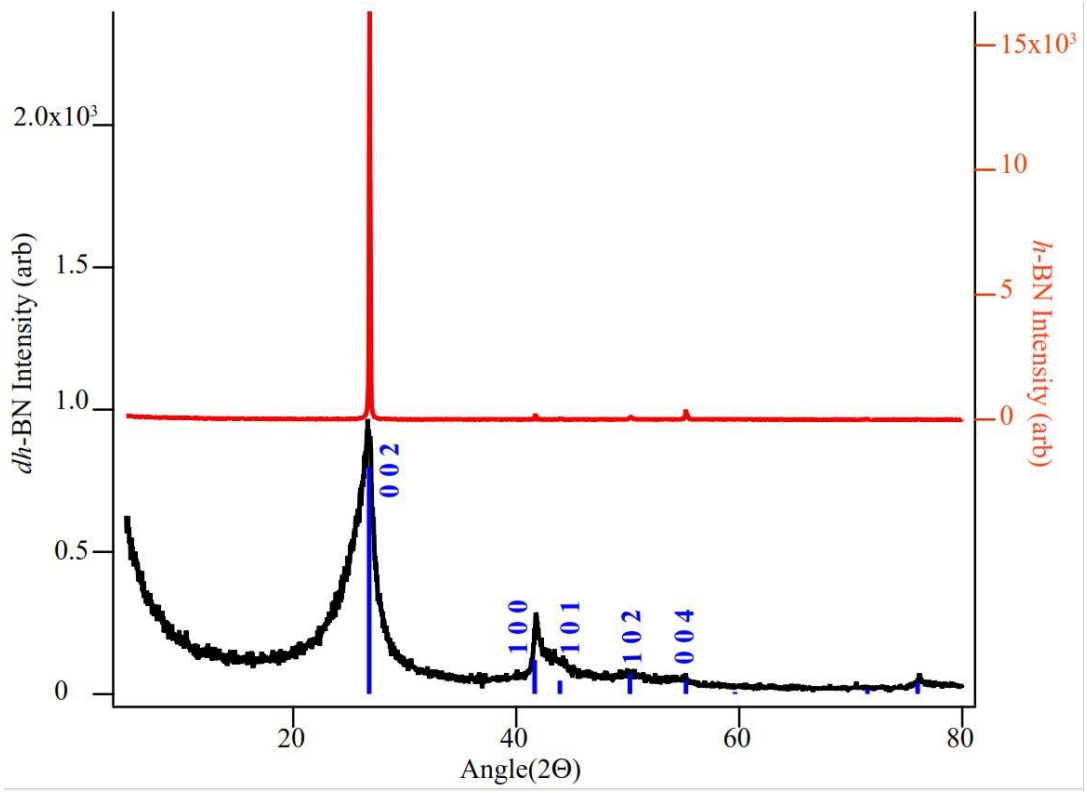

Figure 36: As received *h*-BN (top, red) and *dh*-BN (bottom, black) shows reduction of crystallinity with the c direction still indicating order. A reference pattern for *h*-BN (JC-PDS 34-421) and Miller indices are included in blue.

By performing the hydrogenation reactions under continuous milling conditions, the reduction of CO_2 shows significant increase as compared to static (non-milling) reactions using identical *dh*-BN. The benefit to simultaneous defect site creation and hydrogenation is two-fold: 1) the continuous formation of new defect sites without lattice destruction, and 2) the low-energy mechanocatalysis likely facilitates desorption of gaseous products through plastic deformation of the BN sheets, leading to renewed site availability. Desorption enhanced by shear is observed with polymers adhering to surfaces [68] and was also observed in water release during the large scale mechanocatalytic processing of biomass. [69]

Different types of defects are likely produced from these milling methods (Figure 16) and some defects have more favorable binding energies for CO_2 than others (Table 8). DFT calculations show the highest binding energy of CO_2 occurs within a nitrogen vacancy (V_N), suggesting it to be the most active for CO_2 reduction. This defect site is also favored for the hydrogenation of olefins. [17] But TPD results indicate this may not be the only defect to effectively bind carbon dioxide.

Table 8: Calculated binding energy for ethene, propene, hydrogen, and CO_2 on defects in *h*-BN. Ethene and propene values are from a previous publication. **[17]**

Defect	**Binding Energy (eV)**			
	Ethene	**Propene**	**Hydrogen**	**CO_2**
V_B	-3.71	-3.69	-4.73	-0.69
V_N	-1.90	-1.76	-1.79	-1.97
B_N	-1.95	-2.05	-1.68	-0.21
SW	-0.23	-0.35	1.04	0.43

The TPD of *dh*-BN after CO_2 exposure (but prior to hydrogenation) showed desorption of CO_2 as well as N_2, CO, water, and NO gases. Desorption of gases from defect sites produce peaks in the TPD curves. Two discernable peaks are visible in the CO_2 curve (at temperatures 105˚C and 211˚C) and the mass 28 curve (at temperatures 111˚C and 198˚C) (Figure 23). DFT calculations show that the sites B_N, V_B, and V_N bind CO_2 with energies: -0.21 eV, -0.69 eV, and -1.97 eV, respectively (Table 8). Two of these defects likely correspond to the two CO_2 desorption peaks, with the higher temperature desorption corresponding to a defect with stronger binding energy. The mass 28 desorption curve shows signal for either N_2 or CO gases. However, the similarities in desorption peaks in the CO_2 and CO curves suggest that this signal comes from CO rather than nitrogen and is produced from already adsorbed CO_2. Both curves show close matching

temperatures of desorption on the average of 108˚C ± 3.7˚C and 205˚C ± 8.8˚C, potentially indicating both CO_2 and CO gas molecules desorbed from the same defect sites at similar temperatures. Carbon monoxide has stronger binding affinity in these defects than does CO_2, making it questionable for desorption at the same temperature unless this carbon monoxide originated as CO_2. A surface reaction between a BN defect and CO_2 could produce carbon monoxide gas if a molecule of CO_2 bound to a defect site through an oxygen atom cleaved one C-O bond. This would produce gaseous CO and leave behind a bound oxygen atom in the defect site.

A previous study of the effects of oxygen on *dh*-BN showed strong binding of molecular O_2 in defect sites V_N and V_B of -4.28 eV and -1.38 eV, respectively[18]. Nevertheless, TPD produced no oxygen desorption signals. The binding energies of dissociated oxygen in V_N and V_B defect sites are strong: -9.32 eV and -2.86 eV, respectively. [18] This strong binding energy suggests any atomic oxygen trapped in nitrogen vacancy (thus, bound to B atom) will surely remain trapped. However, atomic oxygen trapped in a boron vacancy (bound to N) has a possibility for desorption as NO gas at elevated temperatures.

SSNMR results further refine the defect site possibilities identified using DFT calculations. Four theoretical model structures were created as possible binding sites for CO_2. These structures are designated as B_N, V_B, V_N conformation 1 and V_N conformation 2 (Figure 37).

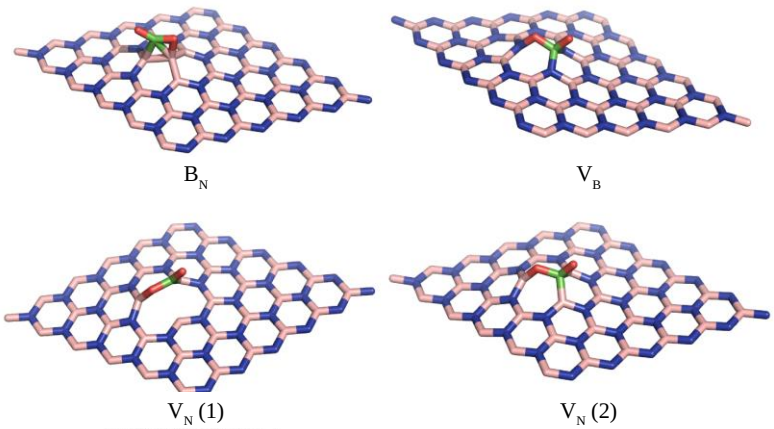

Figure 37: The four model structures considered as binding sites for CO_2.

For each model structure, ^{13}C NMR chemical shifts were computed at the B3PW91/D95** level of theory. Computed shifts for each model are illustrated in Figures 24 and 25. These data show that candidate structures B_N and V_N (2) are in excellent agreement with experimental data. Although V_B gives a less accurate fit to experimental data, it is the next best fit the experimental data and is thus proposed as the third binding site. Model V_N (1) is a poor fit to experimental data and is the least feasible binding site, based on NMR evidence.

2.4.2 CO_2 Reduction

Catalysis using fresh *dh*-BN shows the largest conversion of CO_2 (Figure 26) and with each recycle of the catalyst, the reaction rate decreased. This reduction in activity can be attributed to the formation of strongly adsorbed carbon products (coking) on the catalyst surface, which block active sites and hinder adsorption. XPS and FTIR of post-hydrogenation boron nitride detect these carbon species, which can be bound within the defect sites themselves, as is evident from B-C bonds detected by FTIR (Figure 32). Analysis of cryotrap components from tandem GC-MS-TGA showed the presence of acetic anhydride and water. Early steps in the pathway to non-volatile

adsorbates would be through the formation of acetic anhydride. Starting with the decomposition of adsorbed formic acid (Equation 2.4) to carbon monoxide and water, methanol (formed by the reaction in Equation 2.2) is then carbonlyated to acetic acid (Equation 2.5). Finally, acetic acid is dehydrated to realize acetic anhydride (Equation 2.6).

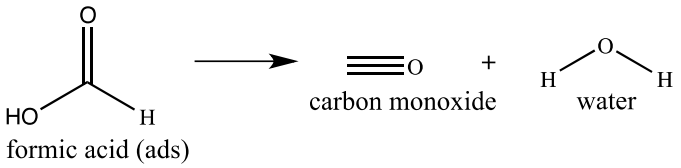

(2.4)

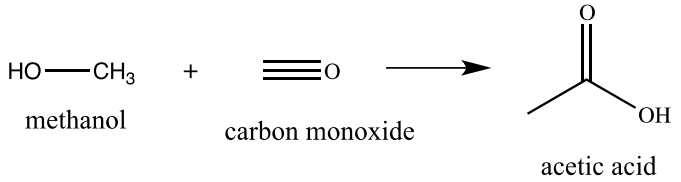

(2.5)

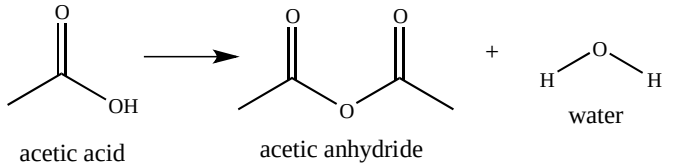

(2.6)

More complex steps may be occurring as the TGA shows continuous mass loss to 800˚C suggesting that the non-volatile coking formed on the *dh*-BN surface is potentially due to C=O containing polymers.

Prior to coking of the catalyst, GCMS analysis found that carbon dioxide processed via batch-mode was converted into methanol (at 20°C and 120°C) and formic acid (at 160°C). Methanol product was observed simply by sampling the headspace gas from the batch-mode reactor, while formic acid required capturing via an activated charcoal trap. TGA of *dh*-BN soaked in methanol, formic acid and acetic acid then air-dried is shown in Figure 29. There is a clear

binding preference for formic acid over methanol that explains the difficulty in sampling formic acid in the reactor headspace. Once formed, formic acid remains bound to the catalyst surface.

In fact, process intensification for formic acid realization may be successful up to temperatures near 700˚C (red heat). Although, above that temperature *h*-BN may not be active for formic acid production as CO_2 is a product of BN synthesis from B_2O_3 and urea (NH_2CONH_2). [70] At such temperatures, reverse water-gas shift (RWGS) products may dominate.

2.4.3 Catalyst Reactivation

Although *dh*-BN shows a decrease in catalytic activity after a few reduction cycles, it has strong potential for regeneration to its original state. Coke products blocking the catalytic active sites can be removed by heating to sufficiently high temperatures. TGA of spent (post-hydrogenation) catalyst, such as that shown in Figure 28, shows significant mass loss and a return of the yellowed *dh*-BN to its original white color after heating to 800°C. This physical color change implies the complete or partial removal of carbon products located on the catalyst surface.

In practice, the *dh*-BN and milling media will be mixed, which should not hinder the regeneration process. Stainless steel media can be heated to high temperatures without consequence, and the bearings can act to enhance the exposed surface of the catalyst, speeding up regeneration.

2.4.4 Presence of Oxygen

It is important to note that the presence of oxygen on defect sites inhibits hydrogenation. [18] The anoxic conditions required for *dh*-BN activity are ideal for CO_2 reduction as the presence of oxygen in a CO_2 stream would reduce overall reaction efficiency, as combustion of hydrogen would be favored over reduction of CO_2.

2.5 Conclusion

Engineering catalytic activity into a solid through the introduction of defects is an important step toward realizing rationally designed heterogeneous catalysts. In this work, defects were induced in *h*-BN through an initial high-energy ball-milling step, which is energy intensive. Previous work found that the low-energy rolling mill produced sufficient impact forces to induce catalytically active defects in *h*-BN. However, the first cycle exhibited a prolonged induction period. [17] Laboratory-scale implementation of this reaction, at room temperature, is not energy efficient. A single cycle consumes 3168 kJ (0.880 kWh) of energy to produce 8.86 kJ worth of methanol. However, the energy consumption of mechanochemical reactors scale favorable as energy consumption does not scale as the cube of the reaction volume. [71] Significant energy costs per kilogram of process material are realized at the 100 kg scale or larger. Scaling of this system would require higher impact frequencies to reduce the dwell time in the reactor as was a gas flow. Flow adapted attrition (Union Process) and agitator mills (Netzsch) would enable this catalysis with few modifications from stock.

Through exploitation of defects, a heterogeneous catalyst for the reduction of CO_2 to methanol and formic acid was realized. Defects in *h*-BN are extremely active toward the formation of low volatility compounds. Increased reaction temperatures or implementation in a plug flow reactor may alleviate this issue. Recent work by Ting *et al* summarizes CO_2 to methanol homogenous and heterogenous efforts.[16] The *dh*-BN system catalyzes the formation of methanol at much lower (by an order of magnitude) CO_2 partial pressures and temperatures (room temperature). The maximum TOF of 56.62 ± 0.60 h^{-1} (1.52±0.02 x 10^{-2} s^{-1}), based on active sites measured by TPD, is better than many hetero- and homogeneous metal-based catalysts Similarly, a total TON of 234 (Tables 6 and 7) is better than many heterogeneous catalysts investigated for the same process (Table 9 and an extensive table compiled by Ting *et al.*[16]).

Table 9: Literature values of the TON and TOF numbers of select catalysts.

Catalyst	T °C	CO_2:H_2	t (h)	TON	TOF (h^{-1})	Product	Reactor	Ref.
dh-BN	20	1:1		234	54.62 ± 0.60	methanol	Ball mill	This work
	120	1:1		108	272.48	methanol	Ball mill	This work
Mo_2C	135	1:3	2	0.4	0.2	methanol	Parr Micro 5500	[72]
Cu/Mo_2C	135	1:3	2	1.5	0.8	methanol	Parr Micro 5500	[72]
Pd/ Mo_2C	135	1:3	2	1.7	0.8	methanol	Parr Micro 5500	[72]
Co/ Mo_2C	135	1:3	2	1.4	0.7	methanol	Parr Micro 5500	[72]
Fe/ Mo_2C	135	1:3	2	1.1	0.5	methanol	Parr Micro 5500	[72]
Cu/$CuCr_2O_4$	140	1:1	5	4.10	2.06	formic acid	Fixed bed	[73]
Cu/ZrO_2/CNT-N	220	1:3	-	-	13.32	methanol	Fixed bed	[74]

The mild reactions conditions are similar to typical electrocatalytic work. [75] These conditions are easier to apply in the field where the storage of solar energy or capture of CO_2 must proceed without the need for constant maintenance. The production of formic acid and methanol are attractive method for energy shifting electrical production from solar and wind sources. Both are useful, liquid fuels that can be used to power small turbines for energy generation at peak demand and the subsequent CO_2 combustion product can be again captured and reused. If active site concentration could be increased from 0.2 mol% to 1 mol%, 4700 m^3 of *dh*-BN would be sufficient to capture and utilize the world's yearly production of carbon dioxide (Table 10). This would translate to a little over 200 catalysts beds smaller than a small shed. Assuming production from borax, this amount would consume less than 1% of the world's yearly boron production – once (Table 11) [76]. Catalysts such as *dh*-BN can provide a pathway toward reduction of global CO_2 release by commoditizing CO_2 thereby encourage utilization versus disposal.

Table 10: Estimation of boron nitride catalyst for converting annual CO_2 production of the world at 120 ˚C.

Value	Unit	Note
37100000000	metric tons	total CO_2 produced in 2018
8.43182E+14	moles	moles CO_2
6.69E+17	seconds	Seconds for 2.5 g *dh*-BN to process all CO_2
8.49E+03	years	Years for a metric ton of *dh*-BN to process all CO_2
8488	metric tons	Tons of *dh*-BN required to process a years worth of CO_2
4042	m^3	Volume of *dh*-BN
22.7	m^3	Volume of a single distributed unit
179	units	Total units required

Table 11: Estimation of boron ore needed for production of the required amount of *dh*-BN calculated in Table 10.

$Na_2B_4O_7 \bullet 10H_2O + H_2SO_4 \rightarrow 2B_2O_3 + 11H_2O + Na_2SO_4$		
$B_2O_3 + 2NH_3 \rightarrow 2BN + 3H_2O$		
Value	**Unit**	**Note**
4250	metric kilotons	World boron production as $Na_2B_4O_7 \bullet 10H_2O$
8488	metric tons	*dh*-BN required
341981249.9	moles	
85495312.47	moles	$Na_2B_4O_7 \bullet 10H_2O$ required
32600	metric tons	
0.77%		Fraction of world yearly production

2.6 Supplemental Information

2.6.1 Mechanocatalytic Batch-Mode Reactor

Batch-mode reactions were performed in a stainless-steel custom pebble mill using a gas-tight reaction vessel shaped as a double truncated cone to provide optimal tumbling of the milling media in the central region of the reaction vessel (Figure 17 and 18a).

Two Conflat flanges (A&N Corporation CF275 flanges with a 1.5 in bore, 275-162) of 2.75 in. were welded onto two 1.5 x 3 in^2 conical reducers (A&N Corporation 300X150-WCR) end to end to build the reaction vessel. Gas-tight conditions were maintained throughout milling by implementing Deublin rotary feedthroughs (1005-020-019, 1005 Series, RH and 1005-020-039, 1005 Series, LH) retrofit with Kalrez o-rings and Krytox lubricant (GPL 105). These rotary feedthroughs were sealed onto two 2.75 in. Conflat flanges with 10-32 tapped through-holes (A&N Corporation; CF275 blank flanges 275-000) and a copper gasket were utilized between flange and feedthrough to create a seal.

Powder was prohibited from entering the rotary feedthroughs by fitting stainless steel filter frits to the entry and exit flanges. While tumbling, the reaction vessel is enclosed in a furnace with NiChrome heating elements. A K-type thermocouple is used to measure the temperature of the reactor by making contact with the upper, outside surface of the reactor.

2.6.2 Plug Flow Reactor

Plug flow reactions were performed in a 0.5” diameter, 16” long stainless steel tube equipped with mass flow controllers and temperature regulation to allow operation at multiple temperatures and pressures under a flow of hydrogen and carbon dioxide.

2.6.3 Temperature Programmed Desorption (TPD)

The TPD experiment was carried out on *dh*-BN with an Altamira AMI-200 instrument using CO_2 as adsorbed gas. Initially, helium was flowed over sample at 20 sccm and 35˚C for 1 hour before flowing a 5% CO_2/He mixture over sample at 20 sccm and 35˚C for 1 hour. The *dh*-BN sample was briefly exposed to air in the transfer to the TPD from an argon environment.

2.6.4 Gas Chromatography Mass Spectroscopy (GC/MS)

Gaseous CO_2 reduction products were analyzed using GC/MS on an Agilent 6890 GC with an HP PLOT U column (30m x 0.32mm x 10µm) with a particle trap (2.5m x 0.25mm OD) coupled to an Agilent 5973 MS detector. The GC method began isothermal at 70˚C for 1 minute, ramping to 180˚C at a rate of 10 ˚C/min and maintaining isothermal conditions at 180˚C for 4 minutes. Gas samples of CO_2 reduction products were obtained by venting the mechanocatalytic batch-mode reactor through a 50 mL serum vial crimp sealed with a PTFE-lined septum previously purged with argon.

2.6.5 Thermogravimetric analysis (TGA)

Pristine, adsorbed, and post-hydrogenation BN samples were studied with a TGA 2050 (TA Instruments). Adsorbed samples included adsorption of CO_2, methanol, acetic acid, and formic acid on *dh*-BN. Pristine samples were dried at 400˚C for 20 hours. CO_2-adsorbed samples were taken from *dh*-BN after CO_2 mass uptake experiments. Liquid adsorptions (methanol, acetic acid, and formic acid) were taken after soaking *dh*-BN overnight and drying in air. BN samples after hydrogenation were stored in crimped serum vials until TGA was performed. All TGA samples were loaded into the sample pan in air, and TGA experiments were performed under flowing argon.

2.6.6 X-ray photoelectron spectroscopy (XPS)

XPS were recorded on a Physical Electronics 5400 photoelectron spectrometer with a magnesium source.

2.6.7 Fourier-transform infrared spectroscopy (FTIR)

FTIR samples were analyzed by pressing samples in a KBr pellet. Spectra were acquired at 2 cm^{-1} resolution utilizing a Bruker Vector 22 FTIR purged with water and CO_2-free air.

2.6.8 Solid-State Nuclear Magnetic Resonance (SSNMR)

Defect-laden *h*-BN was loaded into pressure vessels consisting of 1" triclamp fittings and a 3" long triclamp spool. In a glovebox, one gram of material was placed in an open glass vial in the vessel under argon, evacuated to 20 mtorr, and pressurized with 122 kPa of $^{13}CO_2$ (Icon Isotopes). The ^{13}C spectrum was acquired on a CMX-200 Chemagnetics spectrometer operating at 50.31(^{13}C) and 200.04 (^{1}H) MHz. All spectra employed SPINAL-64 ^{1}H decoupling [77] with a pulse duration of 9.1 μs and an initial phase modulation angle of ± 7°. Cross polarization was employed using a spin-locking field of 62.5 kHz of 1 H and 56.0 kHz on ^{13}C. Other parameters included a 15 s recycle time, a spectral width of 12.5 kHz, a spinning rate of 7.0 kHz and an RF power of 83.3 kHz for the initial ^{1}H excitation. The spectrum was referenced to the methyl peak of hexamethyl benzene at 17.35 ppm. Because the total CO_2 content was low, a total of 25344 scans were acquired to obtain a suitable signal-to-noise ratio. The total experimental time for the analysis was 4.4 days.

Fitting of model peaks to the spectrum was performed using the peak deconvolution software available on the spectrometer (i.e. Spinsight 4.1.3). Three visually distinguishable peaks were present in the spectrum and a peak was fit to each. All peaks were fit as pure Lorentzian

lines with no Gaussian contributions. Peaks were first manually added and adjusted followed by optimized using an automated process than minimizes residuals. Relative peak areas of 3.1:2.5:1.0 were obtained from the fitting for the peaks at 161.7, 156.3 and 151.7 ppm, respectively. The final fit to the spectrum is illustrated in Figure 25.

Theoretical ^{13}C shifts were obtained using Gaussian 16. Shieldings were calculated at the B3PW91/D95** level of theory [78, 79]. Computed shieldings were converted into shifts using the relationship, shift = (shielding – 194.93)/(-1.01). This conversion factor has been demonstrated [80] to give accurate computed shifts for carbons in similar bonding environments.

2.6.9 TG-GC-MS Measurements

Combining thermogravimetry with spectroscopic methods such as GC-MS, FTIR and/or MS, enables the identification of the evolved gases. Temperature-dependent mass changes including gas analysis employed a NETZSCH TG 209 F1 Libra simultaneously coupled to an Agilent 7890A gas chromatograph and the Agilent 5975 MSD (mass selective detector). The Thermo-Microbalance NETZSCH TG 209 F1 Libra, with an effective resolution of 0.1µg, enables highly precise measurements under pure gas atmospheres from ambient temperatures up to 1100°C. Internal mass flow controllers (MFC) guarantee a highly precise gas flow control of three different gases. For control of the measurements as well as for data acquisition, digital electronics and the NETZSCH PROTEUS 32-bit software was employed. The evolved gases are injected over a heated transfer line (up to 300°C) into a heated JAS valve box of the Agilent GC, where, with the help of a carrier gas (usually helium), they are sampled at specified times and transferred to a heated column. The components of the gas mixture are separated on the GC column according to their interactions with the column material (retention time) and are then detected by the Agilent mass selective detector.

The sample underwent continuous mass loss from the start of the measurement. Small leaks in the system inevitably introduce some air into the measurement. The background signals due to air were subtracted from the TIC; however, the presence of air was still apparent at the beginning of the TIC. This is probably due to the elimination of some air from the sample and due to the introduction of some air when sample was inserted in the furnace. Minimal purging was performed after sample insertion so that the mass loss could be captured as soon as possible. All other peaks in the TIC were identified as carbon dioxide.

To determine if organic species may have been present in quantities that were too small to detect in the quasi-continuous measurement, another measurement employing the cryotrap was performed. The purpose of the cryotrap is to concentrate condensable evolved gas species, which are then analyzed off-line. Besides carbon dioxide, the second measurement revealed the presence of acetic anhydride in the material collected in the cryotrap. A large water peak is always observed in these measurements and arises from water adsorbed on interior surfaces of the instrument as well as possibly from water in the sample itself. Despite the apparent complexity of the chromatogram following the water peak, all peaks in that region yielded extracted ion chromatograms consistent with acetic anhydride.

2.6.10 Adsorption Measurements and Pore Size Distribution

Gas adsorption measurements of CO_2 at 195 K and 273 K were collected for surface area and porosity determination on a Micromeritics 3Flex instrument. BN-pristine-dry was shown to be nonporous as indicated by the negligible CO_2 uptake at 195 K with BET surface area of ~ 10 m^2/g. On the other hand, *dh*-BN-milled-1hr showed appreciable uptake for CO_2 at 195 K with BET surface area of ~135 m^2/g.

CHAPTER 3: THERMAL DEGRADATION OF BIOFUELS IN CONTACT WITH HOT METAL SURFACES

Portions of the work in Chapter 3 have been previously published by the following authors: K.L. Chagoya, A. Felix, F. Torres, N. Ciaffone, T.E. Pitts, A. Curbelo, L. Tetard, J. Kapat, R.G. Blair with the title "Thermal degradation of biofuels in contact with hot metal surfaces". They were published by ASME Turbo Expo: Power for Land, Sea, and Air, Volume 4B, on November 5, 2019.

3.1 Introduction

The implementation of biofuels as an energy alternative to conventional fossil fuels is an important step for the adoption of more sustainable sources of power. Unlike the manufacturing of conventional hydrocarbon fuels used in the transportation industry, biofuels can be manufactured above ground from plant and animal waste materials. Although the combustion of any hydrocarbon fuel (biofuel or otherwise) produces GHG emissions, any replacement fuel that does not require drilling or hydrolic fracturing would decrease emissions which arise from obtaining fuels from underground (Figure 38). However, to begin utilizing biofuels in existing engine systems, a study of their thermal degradation and fuel compatibility is needed.

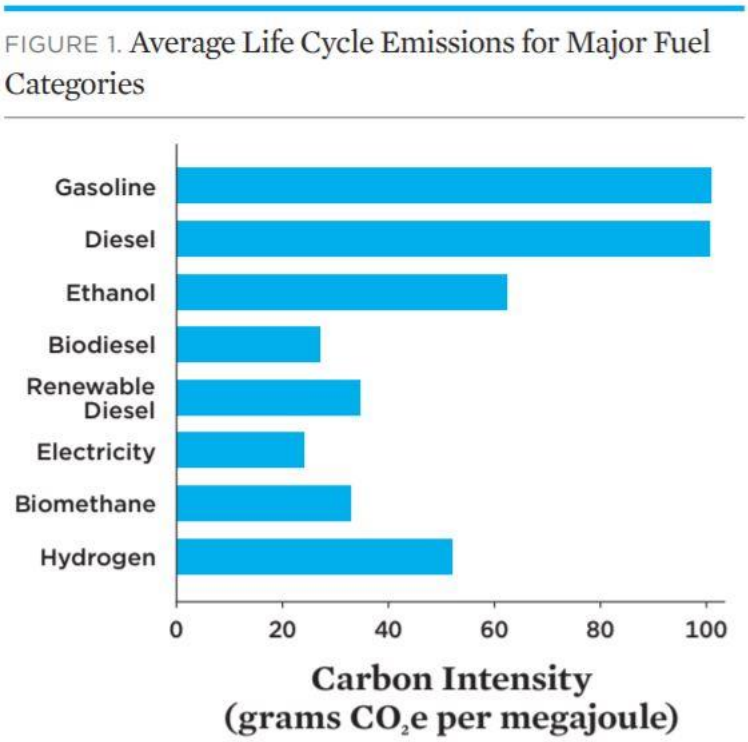

Figure 38: Volume-weighted average carbon emissions for different fuel categories based on 2019 fuel sales in California. Data source: CARB 2020A, CARB 2020B. Image credit: Union of Concerned Scientists (UCS)

Thermal degradation of petroleum-derived fuels to form coke deposits has been a topic of study for decades. [25] The formation of carbon deposits within engines clogs fuel injectors and lines, decreases fuel efficiency, results in costly repairs or replacement of engine components, and produces plumes of black smoke from tailpipes, causing atmospheric and environmental pollution. The combustion of any hydrocarbon fuel will result in these carbon deposits, but for new and emerging biofuels, the extent of this carbon formation for different blends is yet unknown. It is possible that during or after the manufacturing process, fuel mixtures can be chosen which select for chemistries that produce the lowest carbon quantities.

The thermal decomposition of air-saturated hydrocarbons occurs via autoxidation at temperatures between 150 ˚C (300 ˚F) and 480 ˚C (900 ˚F). [81] During autoxidation, free-radical species are formed through the interaction of dissolved oxygen with hydrocarbons, continually

initiating free-radical chain reactions that ultimately result in deposit formation (Equation 3.1). Free-radical chain reactions can also occur in oxygenated hydrocarbons, as shown in Equation 3.2. Above 480 ˚C, soot formation is driven by pyrolysis, in which small carbon species are formed via the breaking of C=C bonds, as opposed to free-radical formation. [82] However, it is unclear if particular hydrocarbon compounds containing certain functional groups are more susceptible to these mechanisms than others.

$$C_xH_y \underset{\Delta}{\rightarrow} \cdot C_xH_y \underset{\Delta}{\rightarrow} C\ (s) + H_2(g) \tag{3.1}$$

$$C_xH_yO_z \underset{\Delta}{\rightarrow} \cdot C_xH_yO_z \underset{\Delta}{\rightarrow} C\ (s) + H_2(g) + CO\ (g) \tag{3.2}$$

A suggested pathway to eliminating these free-radical chain reactions potentially lies in deoxygenation of the fuel blends, or complete removal of dissolved oxygen. It has been shown that deoxygenation of fuels results in a reduction of carbon deposition by autoxidation, and formation becomes negligible at oxygen levels below that of 1 ppm. [83] Studies by Spadaccini and Huang have sought realistic methods for large scale removal of oxygen [82] in an effort to circumvent the need for more complicated routes of soot mitigation. However, most large-scale degassing is too costly for industrial implementation and thus, alternate means of carbon mitigation are still necessary.

In the situation where a hydrocarbon comes into contact with a metal surface, the metal-hydrocarbon interaction can completely alter the decomposition chemistry. Unlike decomposition resulting from standard autoxidation or pyrolysis, the binding energy and location of the hydrocarbon to the metal can cause more unique degradation results. Each hydrocarbon compound will have a specific binding affinity to a metal, and that binding energy may differ significantly

between different elemental metals. The elements Fe, Co, Ni, Cr, and Cu can catalyze carbon production (Equation 3.3) while the elements Al, Ti, Nb, Ta, and Mn have shown resistance to carbon deposition. [84, 85] Moreover, alloys containing multiple of these elements may have more complex interactions with different organic compounds (hydrocarbons).

A promising path to mitigating these unfavorable catalytic interactions could be the coating of high temperature surfaces with metal oxides or other materials. Since metals and non-metals can be catalytically active for carbon formation, metal oxide coatings have been seen to decrease the degradation of fuels over extended periods of time. [86-88]

$$C_xH_yO_z \xrightarrow[Ni,\ \Delta]{} C\ (s) + H_2(g) + CO\ (g) \tag{3.3}$$

Common testing methods for the study of soot deposit conditions are continuous flow dynamic test rigs and static test rigs. [89] Continuous flow test rigs involve the flow of liquid fuel through heated tubes of varying inner diameter, temperatures, pressures, and flow velocities. Soot formations using this method are quantified by cutting sections of the heated tubing and measuring by carbon burn-off or mass difference. Static tests involve a heated fuel reservoir through which oxygen is bubbled. [89] Formation of soot in this method is measured via gravimetric analysis, which requires considerable generation of carbon to analyze directly. To produce this quantity of carbon, temperatures are typically run high and oxygen is bubbled liberally to generate measurable amounts of soot. Thus, continuous flow rigs more closely resemble that of real fuel conditions, since oxygen content is precisely that which is contained in the fuel. Experiments for both static and flow reactors can take hours to complete for one fuel. In the interest of shortening sample times, we have devised a new test rig for measuring the formation of soot involving impingement

of the fuel onto the surface of a heated coupon. This impingement design allows for quantification of carbon deposits with the benefit of reduced sample volume and test duration.

A detailed investigation of the sooting tendencies of biofuels is needed if they are to be utilized as a practical fuel alternative. The chemical composition of biofuel blends may vary from that of conventional fuels, and it is desirable to understand the effects these variations may have in a typical engine environment. Depending on the nature of these compositional differences, thermal degradation may increase or decrease, especially with variations in compounds within different hydrocarbon classes. [27] Furthermore, accomplishing these characterization studies relies on the existence of a rapid testing and screening for promising biofuel candidates, as well as insight into which specific compounds are causing low performance of the blend. If possible, it is desirable that such assessments do not require exceedingly long sampling times.

The compounds tested in this study were chosen based on biomass-derived gasoline and diesel blendstocks identified by the US Department of Energy Co-Optima intiative [90], while taking care to include molecules spanning a variety of chemical functional groups. The five biogasoline compounds investigated are listed in Table 12 and five biodiesel compounds are listed in Table 13. Of the compounds, diisobutylene, butylcyclohexane, n-dodecane, and dodecanes are not oxygenates. In addition, both diisobutylene and dodecanes are inherently chemical mixtures. Diisobutylene contains a mixture of 2, 4, 4- trimethyl-1-pentene and 2, 4, 4-trimethyl-2-pentene, which are both olefins. Dodecanes contains a mixture of C_{12} isomers. The remaining compounds are all potential oxygenation additives, ethanol being a widely used choice in gasoline to suppress soot precursor formation, and in this study provides an alcohol functional group along with 1-nonanol. Cyclopentanone, 2- methylfuran, and methyl acetate are each also biomass-derived fuels [91-93] and contain a ketone, ether, and ester functional groups, respectively.

3.2 Methods

3.2.1 Experimental Procedure

Biogasoline and biodiesel compounds (Tables 12 and 13) are to be characterized for their carbon-forming tendencies on stainless steel, nickel, and aluminum metal. The fuels are not tested as mixtures, but as pure compounds.

Table 12: List of biogasoline compounds tested for coke formation, and their corresponding functional groups and chemical structures.

Bio-Gasoline Component	Functional Group	Chemical Structure
Ethanol	Alcohol	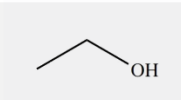
Cyclopentanone	Ketone	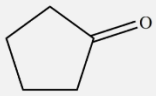
Methyl Acetate	Ester	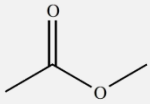
2-Methylfuran	Aromatic Ether	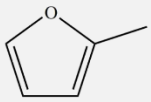
Diisobutylene	Olefin	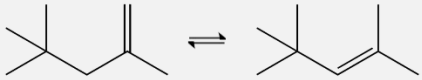

Table 13: List of biodiesel compounds tested for coke formation, and their corresponding functional groups and chemical structures.

Bio-Diesel Component	Functional Group	Chemical Structure
1-Nonanol	Alcohol	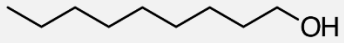
Butylcyclohexane	Cyclic Alkane	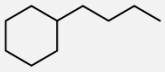
Dibutoxymethane	Diether	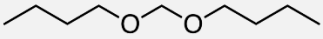
n-Dodecane	Alkane	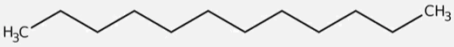
Dodecanes	Alkane Blend	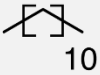

Carbon deposits are formed by spraying individual fuel compounds through an injector (Bosch EV14, PN 0 280 158 038) onto a metal coupon using the impingement test rig in Figure 39. Each metal coupon is placed on a small coiled heater which maintains a coupon temperature of 350 ˚C (Figure 40). A ceramic cup holds the heater and coupon within the injector spray cone (Figure 40). Pressurized argon at 68.95kPa pumps fuel into the injector from a stainless steel reservoir. A 12V pulse circuit controls the release of fuel from the injector which then impinges onto a coupon of either 18-8 stainless steel, nickel, or aluminum. Each coupon recieves a total of 200 fuel pulses of 10 ms each, with a delay of 2500 ms between pulses. Prior to spraying, the impingement chamber containing the metal coupon sample is sealed and purged with argon for 5 minutes to evacuate air from the test environment. Thereafter, a constant flow of argon runs through the chamber for the duration of the experiment and throughout subsequent cooling to room temperature. Excess fuel, which has not decomposed on the coupon, either runs off to the fuel

recovery reservoir or is vaporized and recovered in a trap. The entire experimental setup is shown in Figure 41.

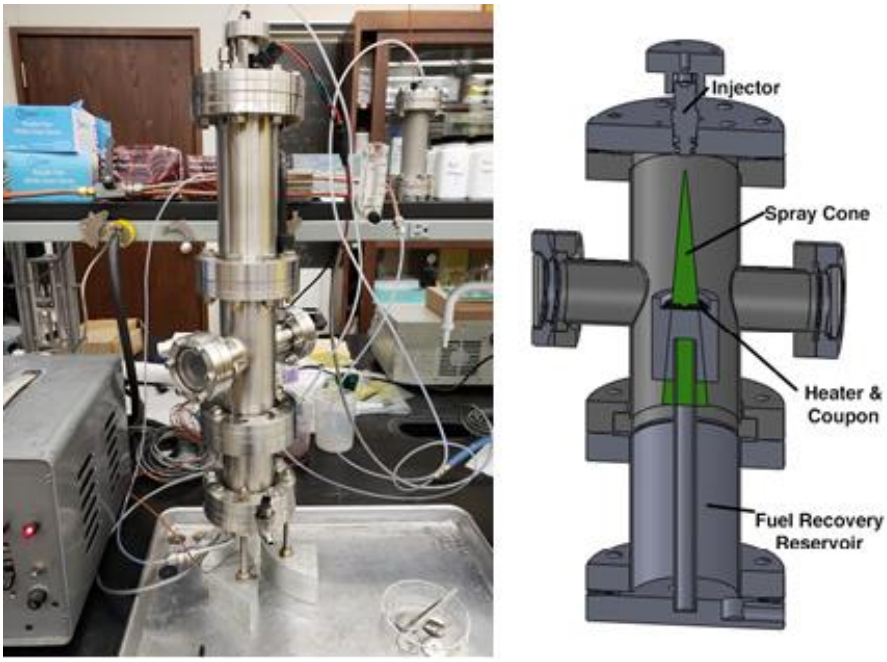

Figure 39: A side-by-side view of the impingement chamber (left) and a schematic of the interior of that chamber (right) showing the placement of the coupon beneath the spray cone.

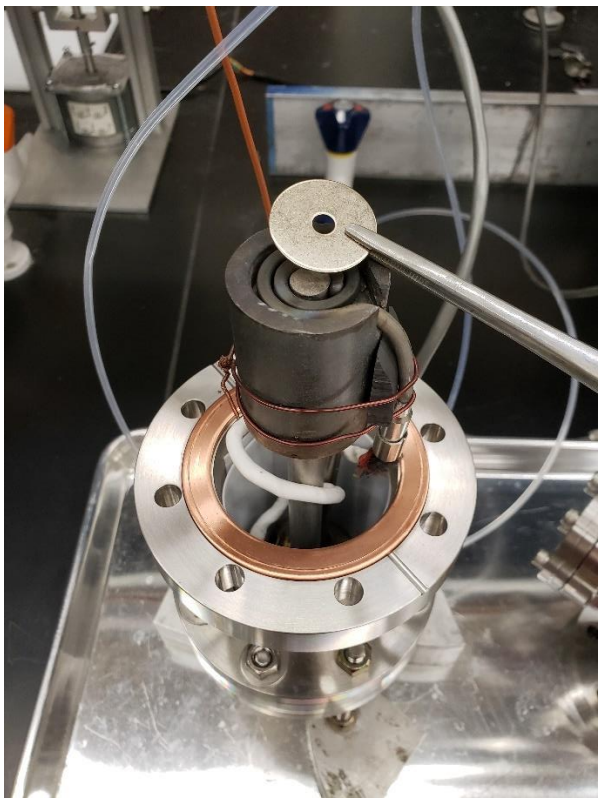

Figure 40: A open view of the inside of the impingement chamber. The metal coupon (here, a steel washer) sits on top of a coiled heater. The heater is held in place by a ceramic fixture. Any fuel that does not degrade to soot on the coupon runs off the ceramic fixture and collects in the base of this chamber.

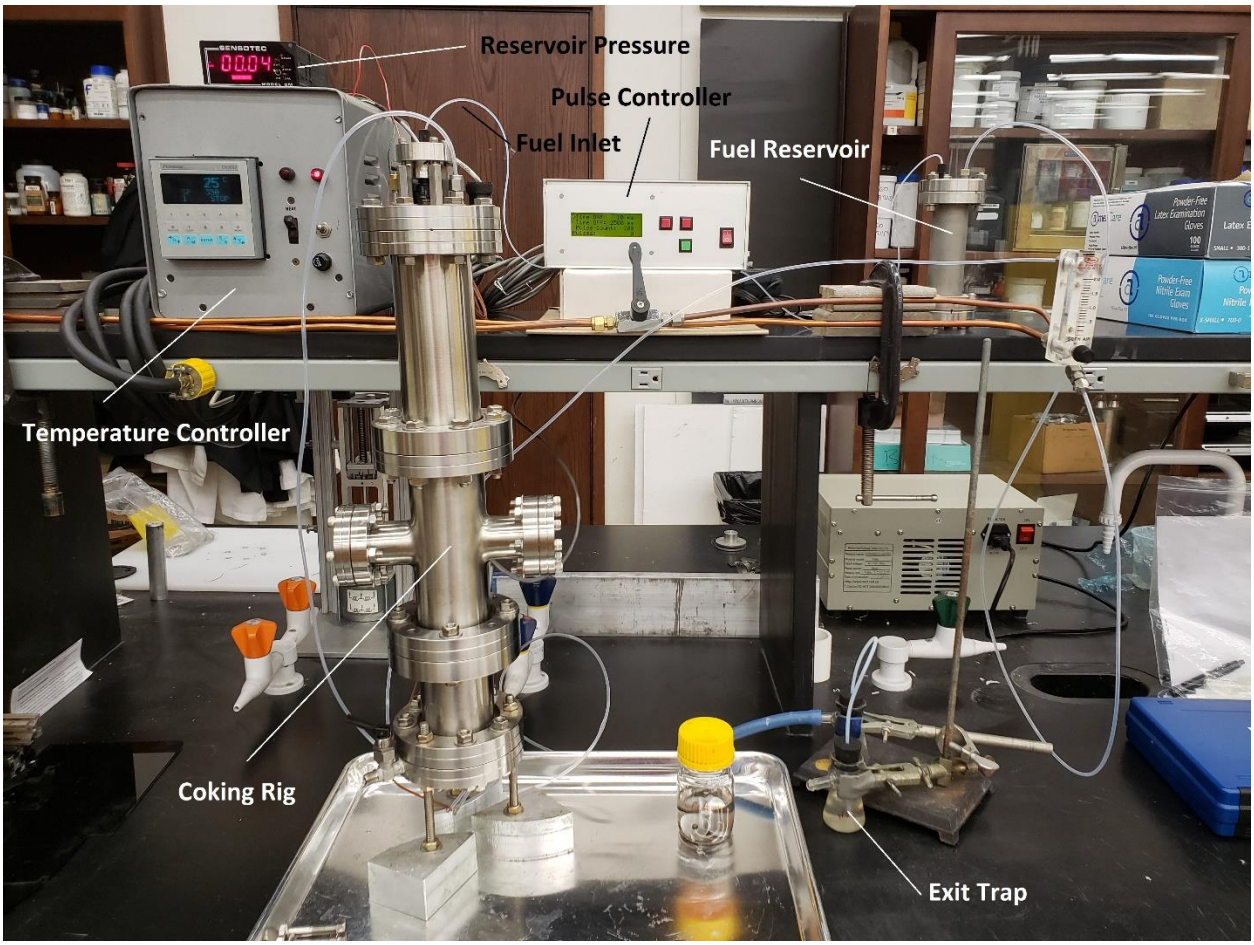

Figure 41: The experimental setup includes the impingement chamber, which consists of a fuel injector located at the very top of a tall steel spray chamber. The height of the chamber allows room for fuel to be sprayed downward onto a surface as well as room for collection of used fuel at the bottom. Fresh fuel sample is contained in the fuel reservoir, and is pumped via teflon tubing to the injector. A pulse controller opens and closes the injector at designated time intervals. A constant stream of argon flows through the impingement chamber which enters the bottom, exits the top, and bubbles through a water trap.

3.2.2 Soot Quantification

Formation of soot is quantified by Raman spectroscopy. The carbon coating accumulated on each metal coupon is analyzed using a Witec Alpha 300 confocal Raman spectrometer with a 532 nm excitation source. An 1800 groove/mm grating and a minimum channel collection width of 0.9 cm-1/pixel were utilized along with a 50x objective lens. Spectra are taken 10 times in a single location to obtain an average scan with low signal to noise ratio. A scan is obtained at 5

different random locations on the coupon. The accumulation of soot can be seen visually after removal of coupon from heater (Figures 42 and 43).

Figure 42: A visual comparison of coupons of 18-8 stainless steel kept at 350°C without hydrocarbon impingement (A) and after 200 pulses of cyclopentanone (B) and 2-methylfuran (C) impingement at 350°C.

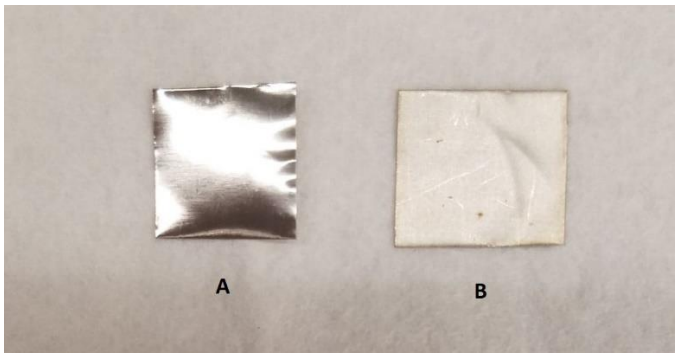

Figure 43: A visual comparison of nickel test coupons kept at 350°C without hydrocarbon impingement (A) and after 200 pulses of 2-methylfuran impingement (B) at 350°C.

3.3 Results

Raman spectral measurements were utilized to measure the layering depth of surface graphitic carbon formation. The blue curve in Figure 44 shows the Raman spectrum of carbon deposition on an 18-8 steel coupon. A pristine coupon prior to impingement with fuel is shown in black for comparison. Post-impingement carbon formation with cyclopentanone reveals disordered (D) and graphitic (G) carbon peaks at the anticipated energies of 1387.72 cm^{-1} and

1591.04 cm^{-1}, respectively. [94] The locations of the disordered and graphitic carbon peaks, D/G ratios, and depth of graphitic carbon layers resulting from each fuel are listed in Tables 14 – 15.

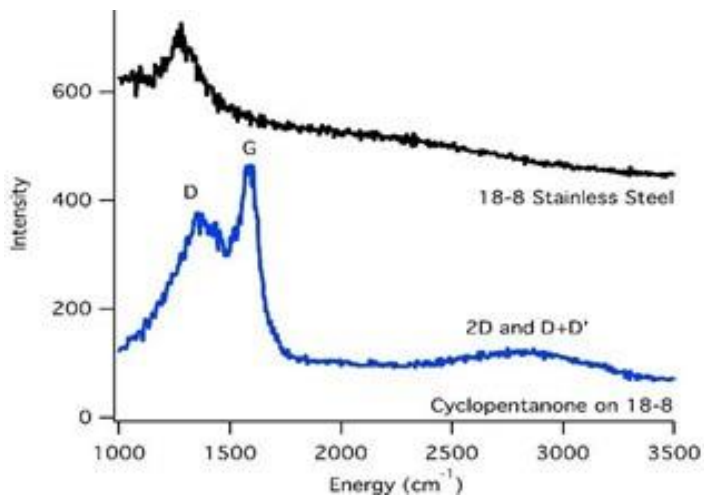

Figure 44: A comparison between the Raman spectra of a blank 18-8 stainless steel coupon after heat treatment without fuel impingement (black) and a stainless steel coupon after impingement with cyclopentanone at temperature (blue) shows the formation of graphite.

The formation of both ordered and disordered graphitic carbon layering was observed for all tested hydrocarbons. Formation of any amorphous carbon was not analyzed. Within the gasoline analog compounds, 4 out of 5 fuels (all but ethanol) exhibited more graphitic carbon formation on nickel than on stainless steel. Ethanol showed slightly larger graphitic carbon formation over steel (2.08 for nickel vs. 2.27 nm for stainless steel). Diesel compounds consistently generated larger quantities of carbon over stainless steel than nickel metal. Across all gasoline and diesel compounds, the largest formation of graphitic carbon was displayed by diisobutylene over nickel metal. The smallest formation of graphitic carbon resulted from methyl acetate decomposition over stainless steel. 1-nonanol, dodecanes, and n-dodecane each resulted in similar carbon formation for both metal coupons, as did dibutoxymethane and butylcyclohexane. Raman spectra from aluminum coupons revealed no signals indicating deposited carbon, and therefore are not included in the tables.

Table 14: A listing of the D (disordered) and G (graphitic) carbon peak locations (energies) and ratios for each fuel tested on nickel in order of decreasing graphitic carbon length.

Fuel	Peak: D Energy (cm^{-1})	Peak: G Energy (cm^{-1})	D/G ratio	Graphitic layer thickness (nm)
diisobutylene	1382.05 ± 10.55	1580.74 ± 2.55	1.22 ± 0.004	2.81 ± 0.01
2-methylfuran	1347.60 ± 6.23	1580.61 ± 1.01	1.06 ± 0.15	2.43 ± 0.36
methyl acetate	1366.93 ± 36.13	1581.95 ± 7.07	1.11 ± 0.53	2.40 ± 1.26
cyclopentanone	1382.53 ± 10.04	1585.82 ± 3.35	1.02 ± 0.26	2.33 ± 0.61
dibutoxymethane	1365.54 ± 8.25	1592.41 ± 9.49	0.92 ± 0.13	2.09 ± 0.30
ethanol	1348.06 ± 4.13	1583.53 ± 4.20	0.93 ± 0.23	2.08 ± 0.54
butylcyclohexane	1381.28 ± 40.65	1580.74 ± 37.09	0.89 ± 0.14	2.04 ± 0.33
1-nonanol	1374.37 ± 16.76	1597.06 ± 30.70	0.97 ± 0.14	1.99 ± 0.37
dodecanes	1366.91 ± 9.76	1584.15 ± 7.90	0.84 ± 0.14	1.92 ± 0.33
n-dodecane	1365.66 ± 9.57	1608.11 ± 18.99	0.83 ± 0.10	1.89 ± 0.22

Table 15: A listing of the D (disordered) and G (graphitic) carbon peak locations (energies) and ratios for each fuel tested on stainless steel, in order of decreasing graphitic carbon length.

Fuel	Peak: D Energy (cm^{-1})	Peak: G Energy (cm^{-1})	D/G ratio	Graphitic layer thickness (nm)
butylcyclohexane	1390.66 ± 14.98	1579.42 ± 5.66	1.04 ± 0.08	2.39 ± 0.18
dibutoxymethane	1372.62 ± 26.03	1592.15 ± 15.71	1.04 ± 0.30	2.38 ± 0.69
ethanol	1372.10 ± 3.06	1586.91 ± 0.26	1.03 ± 3.0%	2.37 ± 0.031%
cyclopentanone	1390.60 ± 2.12	1587.48 ± 1.32	1.03 ± 5.8%	2.37 ± 0.059%
diisobutylene	1376.54 ± 8.11	1582.81 ± 4.17	0.98 ± 18%	2.24 ± 0.185%
dodecanes	1371.10 ± 22.90	1586.54 ± 7.45	0.93 ± 0.18	2.13 ± 0.36
1-nonanol	1356.93 ± 8.10	1587.56 ± 1.66	0.93 ± 0.06	2.12 ± 0.15
n-dodecane	1358.36 ± 6.68	1588.74 ± 2.16	0.93 ± 0.04	2.12 ± 0.10
2-methylfuran	1377.92 ± 4.55	1583.33 ± 2.77	0.83 ± 0.7%	1.90 ± 0.008%
methyl acetate	1389.98 ± 7.81	1578.61 ± 7.54	0.60 ± 20.9%	1.35 ± 0.219%

3.4 Discussion

3.4.1 Modes of Fuel Degradation

For standard combustion of hydrocarbons in a flame, the dependence of soot formation on oxygen content and chemical functional groups is well established. [95, 96] However, outside an ignition zone, the introduction of a catalytic or inhibiting surface (such as the walls of engine components) will significantly alter the mechanism of carbon formation. As the hydrocarbon

compounds interact with the metal surface sites, fuel molecules have the potential to bind to the metal surface, altering their bond energies, and causing reactions. While actual ignition and combustion of fuels relies more strongly on the concentration of oxygen and oxygenated additives in the fuel blend, the presence of a catalytic surface shifts importance directly on the chemical functional groups of the hydrocarbons themselves, since these are the binding locations of the fuel molecules to the surface. For standard fuel degradation and formation of carbon, the creation of precursors and polycyclic aromatic hydrocarbons is the initial step in production. [97] This step is initiated via the formation of free-radicals and hydrogen abstraction, with a chain terminating step of removal of the oxygen atom as CO_2 or CO formation, which do not proceed further in the chain reaction. [95] However, chemisorption of a fuel molecule to a surface site may be more predictable than the free-radical mechanism. Thus, catalytic degradation of hydrocarbons may be more predictable than other modes of degradation. The binding of a substrate to a surface site will decrease the energy required to cleave bonds, leading to carbon formation.

3.4.2 Interactions on Metal Surfaces

Nickel is a known catalytic surface for a number of reactions. The fact that it is composed of a single type of atom (nickel atoms) indicates the interactions over its surface are significantly simplified as compared to a metal alloy consisting of many elements (such as steel). Similarly, aluminum metal, although inhibiting by nature and not catalytic, offers a comparable simplicity. Unlike nickel and aluminum, stainless steel contains more than one potentially catalytic element (i.e. iron, chromium). However, this does not imply increased catalytic activity for carbon formation over nickel or any other individual metal. It does, however, increase the complexity of the material, as it is unclear which catalytic element contributes the most or if there are interatomic

interactions. The nickel, aluminum, and stainless steel chosen for our experiments offer a uniform catalytic surface, a uniform inhibiting surface, and a surface mixture, respectively.

3.4.3 Functional Group Contribution

Over our ideal catalytic surface (nickel), olefins which contain a C=C double bond (diisobutylene and 2-methylfuran) are observed to have the largest graphitic carbon formation. From Figure 45, you can see this is closely followed by molecules with the bonds C=O (methyl acetate and cyclopentanone), C-O (dibutoxymethane), C-OH, and C-C. To identify a correlation between carbon formation and surface binding affinity, the individual binding energies of each of our fuel molecules would prove useful. In place of these energies for our specific fuels, Table 16 shows literature values of the binding energies of simple representative molecules over nickel surfaces. Methanol, ethylene, formaldehyde, and furan are the simplest representations of alcohol, olefin, C=O molecules, and furans, respectively. The strongest binding energy of -217.57 kJ/mol corresponds to furan, which is not surprising, as it contains multiple sites from which it could bind. Formaldehyde, ethylene, and methanol are of subsequently smaller binding energies, methanol coming in last place with the relatively weaker energy of -25.48 kJ/mol.

Table 16: Literature values for the binding energies of methanol, ethylene, formaldehyde, and furan over nickel metals.

Binding Site	**Binding Energy (kJ/mol) from Literature**			
	Methanol	**Ethylene**	**Formaldehyde**	**Furan**
	–OH	C=C	C=O	Ring
Nickel	-25.48	-79	-149.81	-217.57
Ref.	[98]	[99]	[98]	[100]

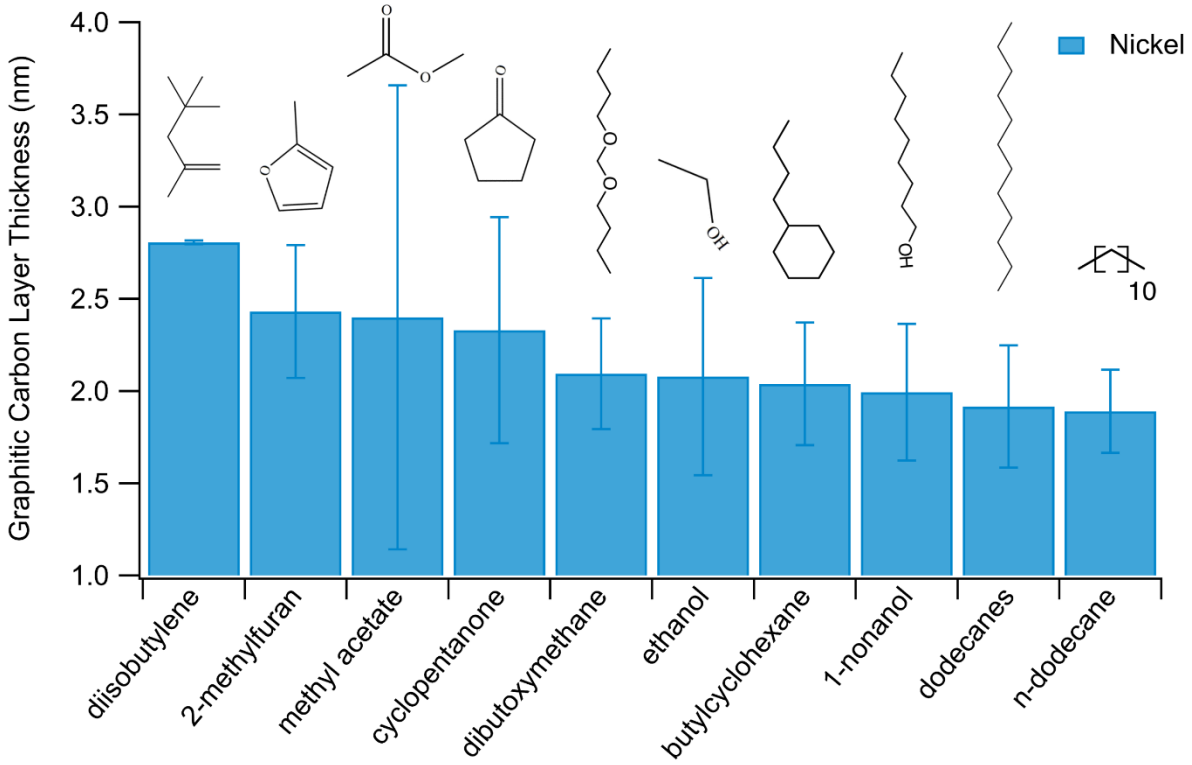

Figure 45: Comparison of carbon spot size on nickel coupons for each fuel.

A strong binding energy, such as that exhibited by furans, would allow compounds such as 2-methylfuran to adhere longer on the surface, accumulating graphitic carbon fragments to achieve more ordered carbon structures. The literature binding energies depicted in Table 16 correlate exceptionally well with our results with the exception of ethylene, or the C=C (olefins). Where the table suggests olefins should have the second weakest binding energy, diisobutylene is nevertheless our largest former of graphitic carbon. Of course, binding affinity may not be the only factor at play. Other processes occurring simultaneously with catalysis may inflate the quantity of graphitic carbon. As an example, if free-radical formation were occurring in tandem with catalytic degradation, the carbon from both processes would be present. The specific chemical structure of

diisobutylene makes it particularly susceptible to forming radicals, since it allows for multiple resonance-stabilized radicals. It has been shown that branching tends to increase the formation of carbon. [101]

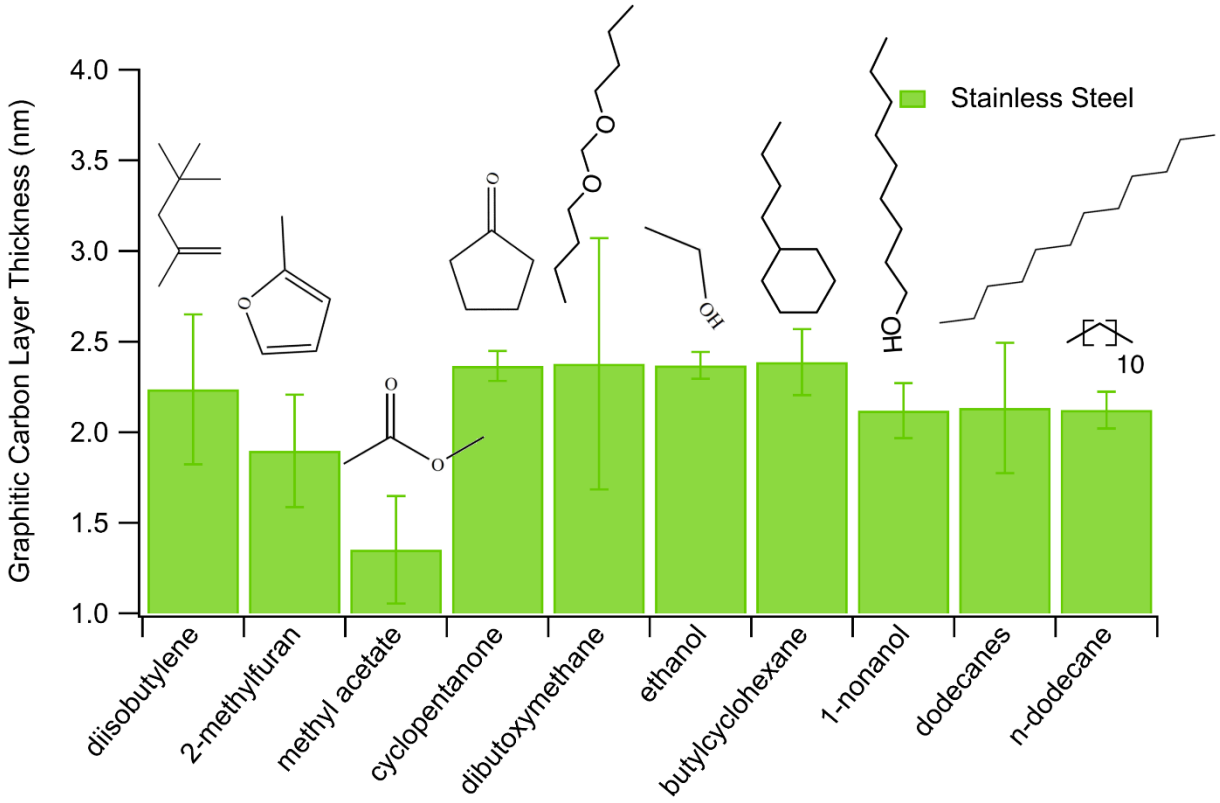

Figure 46: Comparison of carbon spot size on stainless steel coupons for each fuel.

Although diisobutylene is the most susceptible to free-radical formation of all our fuel compounds, other molecules also exhibit some degree of vulnerability. The structure of cyclopentanone offers multiple locations for hydrogen abstraction to occur. With varying possible locations for the cleavage of the ring, cyclopentanone is likely to produce a variety of free radical intermediates which could propagate to form larger carbon layers.

Inspection of the reaction pathways for the decomposition of methyl acetate shows much fewer possible degradation products than cyclopentanone. [102-104] Hydrogen atom abstraction occurs from the methoxy and acetyl groups on the molecule, resulting in the formation of formaldehyde and ketene, which are small molecules compared to the long-chain radical products of a molecule such as diisobutylene or 2-methylfuran. This is a direct result of the high oxygen content of methyl acetate, as well as the placement of that oxygen within the molecule. The linked oxygen atom in esters prevents carbon from forming soot precursors, and instead forms CO_2. [95] Formaldehyde and ketene have the ability to further decompose into even smaller radicals that terminate at CO and C_2H_6. Thus, methyl acetate has a low potential of degradation via free-radical chain reactions relative to other compounds. The introduction of a catalytic surface allows a methyl acetate molecule to bind more strongly than a cyclopentanone molecule to nickel, decreasing bond strength and resulting in higher degree of decomposition for methyl acetate. However, in stainless steel, this may account for methyl acetate's low graphitic carbon formation.

Among the fuels, the hydroxyl group is present in only ethanol and 1-nonanol, and their resulting graphitic carbon formations are very similar, despite 1-nonanol's relatively long carbon chain. Over transition metal oxides, ethanol can be dehydrated to form ethylene, [105] which is soot- forming, [106] but does not proceed via free radical chain reactions. Mechanisms for the thermal decomposition of basic alcohols such as ethanol have been studied over nickel- copper catalysts. Although degradation mechanisms in the autoxidation regime typically require free radical formation, it has been shown that ethanol can utilize alternative pathways in the formation of soot. [107, 108] These additional pathways could cause an increase in carbon formation for ethanol, but the results show strong similarity between the compounds. Stainless steel degradation results are shown in Figure 46, and are ordered with the same high-to-low carbon formation as

nickel, in order to visualize their stark differences. In the case of steel, methyl acetate had the lowest formation of graphitic carbon though it was the third largest former in nickel. The fact that there is little correlation to nickel coupons illustrates the difficulty with which mixtures of catalytic metals can be predicted.

In both nickel and stainless steel coupons, a high standard deviation most likely results from steep variations in carbon deposit in different locations upon the coupon surface. In addition, variations in fuel viscosity (Table 17) between compounds determines the behavior of droplets during spraying, potentially causing nonuniform distribution of the liquid on the coupons at temperature. Nonhomogeneous coverage of the coupon can result in artificially high or low values for soot formation, depending on the chosen location of the Raman laser. To reduce this effect, the measurement of 5 locations on the metal coupon surface are averaged. Each fuel/metal interaction was analyzed in triplicate. The size of the soot deposits were calculated based on methods by Reich and Thomsen. [94]

Some physical properties of the 10 fuels are listed in Table 17 in order to visualize a the trends in these physical parameters and how they might have been influential in their carbon formations. Yet, the carbon and oxygen number seem to have no bearing on the degradation results. Neither do the boiling point, nor the viscosity of the liquids.

Table 17: Properties of gasoline and diesel analog compounds.

Fuel	Chemical Formula	MW (g/mol)	Boiling Pt. (°C)	Viscosity (cP)	Carbon Number	Oxygen Number
ethanol	C_2H_6O	46.068	78	1.099	2	1
methyl acetate	$C_3H_6O_2$	74.08	57.4	0.353	3	2
cyclopentanone	C_5H_8O	84.12	130	1.125	5	1
2-methylfuran	C_5H_6O	82.1	64	0.374	5	1
diisobutylene	C_8H_{16}	112.21	102	0.388	8	0
1-nonanol	$C_9H_{20}O$	144.25	215	9.682	9	1
dibutoxymethane	$C_9H_{20}O_2$	160.25	180	1.02	9	2
butylcyclohexane	$C_{10}H_{20}$	140.27	179	1.196	10	0
n-dodecane	$C_{12}H_{26}$	170.33	216.3	1.376	12	0
dodecanes	$C_{12}H_{26}$	170.33	216.3	1.376	12	0

3.5 Conclusion

An impingement-style apparatus has been developed to quantify the graphitic carbon formation of liquid fuels using Raman spectroscopy. The method involves spraying of the fuel onto a heated metal coupon, which in this study are nickel, aluminum, and stainless steel. We have examined 5 biogasoline analog fuels: ethanol, diisobutylene, methyl acetate, 2-methylfuran, and cyclopentanone and 5 biodiesel analog fuels: 1-nonanol, dibutoxymethane, butylcyclohexane, dodecanes, and n-dodecane, which have all been chosen based on the recommendations of the US Department of Energy Co-Optima initiative. In addition, each of the fuels chosen represents a separate hydrocarbon class, or chemical functional group. We have found that diisobutylene produced the most carbon over a catalytic nickel surface using this method, followed by 2-methylfuran and methyl acetate. This result agrees with literature binding energies of these compounds on nickel surfaces. Aluminum metal coupons successfully inhibited formation of graphitic carbon, to the extent that raman spectroscopy could detect no signal. Stainless steel coupons showed a wide variation of results as compared to nickel, with the highest carbon former being butylcyclohexane (narrowly) and the lowest former being methyl acetate. The complexity of the stainless steel surface (being a mixture of catalytic elements) renders it more difficult for

predicting and analyzing trends without the knowledge of the catalytic results of those elemental components (iron and chromium) for our fuel compounds. Elucidating these trends would be an interesting future study.

CHAPTER 4: HARVESTING HEAT FROM SAFER, ENERGY-DENSE SLOW PYROLANT MIXTURES FOR FUTURE SPACE MISSIONS

4.1 Introduction

4.1.1 Human Space Exploration

Since the start of human space exploration in the late 1950s, the number of space programs and agencies across the globe have grown, humans have sent probes and spacecraft to distant parts of the solar system, and humans themselves have left the planet. It can be said that the past 65 years of space travel and discovery have provided humanity with some of the greatest technological and scientific advancements of any other age. [109] However, it can also be said that space exploration is not occurring fast enough, since high impact missions are launched typically on the order of years or decades. Political, [110, 111] legal, [112-114] and societal [115] challenges and constraints are commonly debated as potential explanations for humanity's slow space colonization progress. However, construction of a spacecraft and its components are non-trivial and complex, not to mention the physical human limitations [116-118] which are now in the spotlight as conversations turn to increased manned missions and long-term outer space habitability.

Currently, the United States' National Aeronatics and Space Administration (NASA) is the most active and funded space organization on Earth. [119] A mission to space within NASA's Planetary Missions Program will fall into one of three groups: Discovery, New Frontiers, or Solar System Exploration (Table 18). [120] Small missions which require few resources and short development times fall into the Discovery class, which can potentially launch a spacecraft from Earth in as little as 36 months (3 years) of the mission's conception. These Discovery class missions define today's standards for "frequent" human space exploration. However, our most

ambitious and compelling missions do not have such short development times, nor do they have comparable budgets. Missions involving high-priority science objectives that strive to investigate a range of questions commonly fall under Solar System Exploration. [120] These are the flagship missions (now called Large Strategic Science Missions) for the Planetary Science division, and their costs enter the range of billions of dollars. [120]

Table 18: NASA's Planetary Missions Program classifies missions into 3 groups. [120]

Program	Mission Budget	Development Time	Class	Description
Discovery	$450 million	36 months	Small missions	➢ Established in 1992 ➢ Missions require fewer resources ➢ Selection process: peer-reviewed competition
New Frontiers	$850 million	60 months	Mid-size	➢ Established in 2003 ➢ Missions bridge gap between flagship and Discovery class ➢ Selection procees: peer-reviewed competition ➢ High-priority Planetary Science Community mission goals
Solar System Exploration	$2 – 3 billion	>5 years	Flagship	➢ High priority targets ➢ Often missions of national importance ➢ Selection Process: None. Missions assigned directly to a NASA center

This high cost and lengthy development time comes in part from the scientific instruments on board, as well as the power system for the craft. Flagship missions typically require robust materials and complex equipment in order to accomplish the ambitious goals of the mission. Although decreasing the costs associated with each analytical instrument onboard a spacecraft is a wide and complicated task, devising low-cost power sources is not outside our reach. A low-cost and versitile mode of energy production could drop some high-priority missions down from Flagship class to a lower class, allowing for more frequent launches to these high-priority targets and shortening the timeline of scientific discovery.

4.1.1.1 Radioisotope Thermoelectric Generators (RTGs)

An RTG can be fueled by a number of isotopes, including americium-241 and strontium-90, which is commonly used at remote locations on Earth. Plutonium-238 is NASA's isotope of choice for spacecraft, and it is provided in the form of plutonium dioxide pellets ($^{238}PuO_2$). Radioisotopes offer power options on the order of tens of kilowatts, which is lower than some chemical fuels and most nuclear power options. However, their lifetimes are far greater, in the range of years, as illustrated in Figure 47. Although the power output capabilities of an isotope degrade over time based on its half-life, Pu-238 retains most of its heat output within half a decade of its creation.

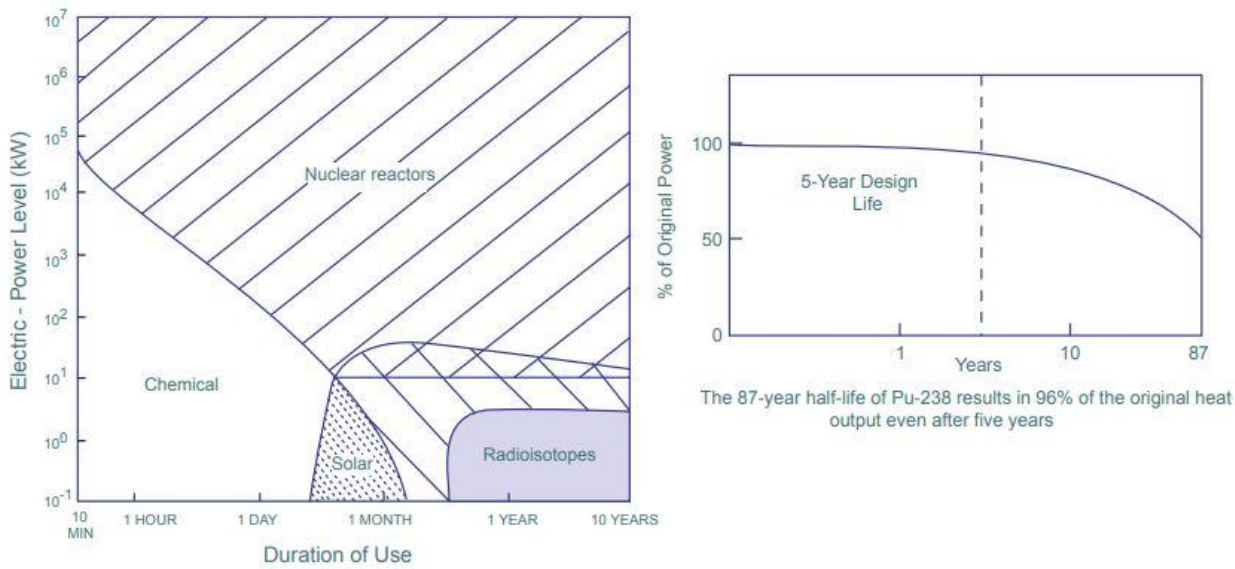

Figure 47: (Left) Lifetime and power output of a radioisotope thermoelectric generator. (Right) The remaining power able to be produced by the RTG accounting for isotope decay.

Over time, there have been several generations of RTG technology to meet the power needs of their spacecrafts. The Systems for Nuclear Auxillary Power (SNAP), one of the first variations, had an initial power output of approximately 40 and 70 W for the SNAP-19 and SNAP-27, respectively. The Multi-Hundred Watt (MHW-RTG) power source employed on Voyager 1 and 2 more than doubled the output of the SNAP-27, at 158 watts of power at the mission start. The

general purpose heat source RTG (GPHS-RTG) is a combination of 18 GPHS modules which provided a total power output of 292 W at the beginning of the Galileo, Ulysses, Cassini, and New Horizons missions. Galileo and Cassini both utilized more than one GPHS-RTGs (2 and 3 for Galileo and Cassini, respectively). [121] The newest generation, named the multi-misson radioisotope thermoelectric generator (MMRTG) was designed to operate not only in the vaccum of space, but also within a planetary atmosphere. The MMRTG (Figure 48) was first utilized on the Curiosity Rover as part of the Mars Science Laboratory mission launched in 2011 and contains 8 GPHS modules, collectively generating about 110 W of power.

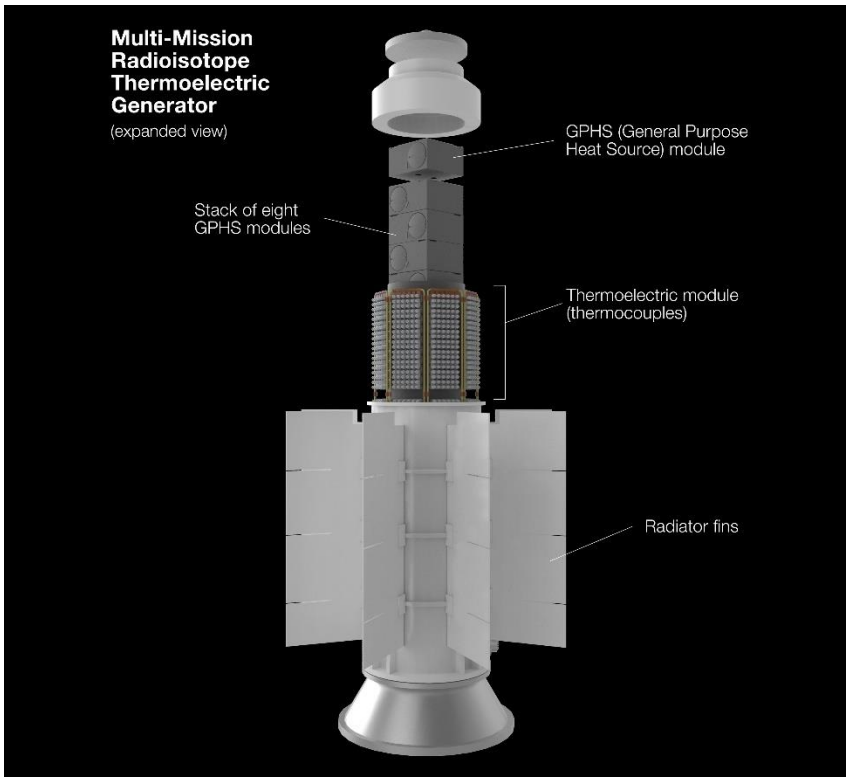

Figure 48: A multi-mission radioisotope thermoelectric generator (MMRTG) consisting of 8 GPHS modules, and thermocouples which convert the generated heat into electricity. Image credit: NASA.

As much as the RTG has fascilitated the most ambitious of NASA's flagship missions, there are grounds for diversifying spacecraft power options. The United States halted it's production of plutonium in 1988, making new plutonium-238 difficult to source . The plutonium

already in the U.S. stockpile could only provide fuel for 3 additional MMRTGs, one of which currently powers the Perseverence Rover which landed on Mars in 2021, and another which is reserved for the future Dragonfly mission to Titan. Although Oak Ridge National Laboratory has since began producing Pu-238 again in small quantities under the US Department of Energy Supply Project, the goal is to produce 1.5 kg/year by 2026. [122] A single MMRTG requires approximately 3.4 kg of Pu-238, whereas the GPHS-RTG requires 7.7 kg. [39]

If NASA is to increase the frequency of its flagship missions, attempts to unrestrict itself from the RTG should be made. The capability of generating a steady flow of heat for a long period of time need not be dominated exclusively by radioisotopes. Solid-state exothermic reactions could potentially provide the necessary heat for electrical power generation, which would provide a similar enclosed, environmentally-resistant power source, allowing for long-distance and long-duration missons at a reduced cost.

4.1.2 Solid State Exothermic Reactions

The heat produced by solid-state exothermic reactions could potentially be harvested as energy to power missions that would otherwise be powered by an RTG. The exothermic condition is met by any chemical reaction which contains a negative value for enthalpy, which can be calculated using Equation 4.1 for a typical chemical reaction. [123]

$$\Delta H^{\circ} = \sum H_{products} - \sum H_{reactants} \tag{4.1}$$

The more negative a value of enthalpy, the more heat produced by a reaction, whereas an overall positive enthalpy value indicates an endothermic reaction, or one which requires heat input. A thorough explantation of the enthalpy calculation for a balanced chemical reaction is provided in the section to follow. We seek to determine chemical reactions with the most negative enthalpies

for potential use as slow burning pyrolants. The enthalpy value for a chemical reaction system can then be utilized to quantify the maximum temperature reached by the burning reactants in a closed system, which is the subject of the next section.

4.1.2.1 Calculating Adiabatic Flame Temperature

It is important to determine the maximum temperature capable of our exothermic reactions in order to assess which reaction should provide the largest quantity of heat able to be harvested. Such a temperature is termed the adiabatic temperature (T_{ad}) and this quantity differs from a reaction's enthalpy. Although an exothermic chemical reaction may produce heat upon completion, not all of this energy is released as heat or is usable for work. The energy produced from reagents can be absorbed by the products in different vibrational modes (the products' heat capacities) as well as in phase changes, if such an event occurs. Therefore, the value obtained from an enthalpy calculation might indicate a larger production of heat than is usable in reality, and can be seen as a theoretical value until heat capacity and other heat sinks specific to a chemical reaction have been accounted for.

The concept employed for this calculation involves initially quantifying the total enthalpy of the reaction. This is accomplished using the chemical reaction containing all starting reagents, and with the general knowledge of the most likely product(s) to be formed. Given a chemical reaction between reagents A and B which produce the products C and D, the stoichiometric coefficients (a, b, c, and d, respectively) must be found by balancing the chemical equation, which should result in something resembling Equation 4.2. The overall reaction enthalpy can then be calculated using Equation 4.3 (which is an expanded version of Equation 4.1), if the enthalpies of formation (H_f) are known for each reagent and product at STP (standard temperature and pressure). [123] The degree sign included in the abbreviation for enthalpy, $\Delta H°$, refers to the standard

enthalpy of formation when the reagents are at STP. Typically, enthalpies of formation for specific compounds can be found at STP in reference texts, literature, or chemical databases such as the National Institute of Standards and Technology (NIST) Chemistry WebBook Database. [124]

$$aA + bB \rightarrow cC + dD \tag{4.2}$$

$$\Delta H^{\circ} = \left(cH_{f,C} + dH_{f,D}\right) - \left(aH_{f,A} + bH_{f,B}\right) \tag{4.3}$$

Once the specific enthalpy (ΔH°) has been obtained, we can begin the process of determining T_{ad}. The following paragraphs will first describe the logic behind the calculation, followed by a handful of formulas needed before we can perform the T_{ad} calculation, and will end with putting the pieces together to obtain T_{ad}.

We must begin with the assumption that products C and D were formed with 100% yield (the reaction went to completion and reagents A and B are no longer present). With a system now containing only products, a series of accounting steps can be taken at small increments of temperature beginning at 298 K (room temperature). For each incremental rise in temperature, ΔT, of products C and D, we will determine the heat (Q) that must have been absorbed by these compounds to increase their temperature, and we will subtract that heat, Q, from the total standard enthalpy, ΔH°. In addition, if one of the products should undergo a phase change at a specific temperature, the heat required for that phase change is subtracted from the total enthalpy, ΔH°, until all the energy produced by the exothermic reaction has been expended (i.e. ΔH°=0). At the point when the internal energy, ΔH°, has been expended, whatever temperature the products C and D have reached is the adiabatic temperature.

Of course, in reality, the chemistry of a reaction is unlikely to proceed in this way. It is unlikely that 100% of the product is formed at room temperature at which point the products begin

to absorb the produced exotherm. It is more plausible that the consuption of reagents to produce products, heat production, heat absorption, and phase changes occur together and at times simultaneously. However, accounting for the order of these events can be impossible as well as unnecessary for bookkeeping the released heat.

Here will be given a general example of the adiabatic temperature calculation for a generic chemical reaction which may look like Equation 4.2. We will discuss a few different heat sinks, or phenomena which would cause the products to absorb heat. However, we will assume adiabatic conditions, meaning we will assume no heat travels outside the system of our compounds to the environment. The heat sinks we will consider are listed in Table 19.

Table 19: Types of heat sinks to consider for adiabatic temperature calculations.

Heat Sink	**Quantity Needed**	**Abbrev.**	**Unit**
Heat absorbtion: storage in molecular vibrational modes	Heat capacity (const. pressure) as a function of temp	$C_p(T)$	J/molK
Phase change: melting	Heat of fusion	ΔH_{fus}	kJ/mol
Phase change: Evaporation	Heat of vaporization	ΔH_{vap}	kJ/mol

Some amount of the heat produced by the chemical reaction will be absorbed by the reaction products C and D, each of which can store the kinetic energy in the form of molecular vibrations. Depending on the bonds contained by the compounds C and D, the heat can be stored in a bond stretching, bending, or twisting, which together we will call the heat capacity, C_p, of that compound or molecule. Heat capacities for different compounds can be found at STP in reference texts and chemical databases. However, to increase accuracy it is best to determine the heat capacity as a function of temperature, $C_p(T)$, which can be found using the Shomate equation (Equation 4.4), where constants L, M, N, O, and P are determined experimentally and for many compounds are often listed in the NIST Chemistry WebBook Database. [124] In Equation 4.4, t is a fraction of temperature described by Equation 4.5.

$$C_p^\circ = L + Mt + Nt^2 + Ot^3 + Pt^{-2} \tag{4.4}$$

$$t = {}^{T}/_{1000} \ (T\ in\ Kelvin) \tag{4.5}$$

For a chemical reaction containing a single product C, calculating the Shomate equation one time to determine $C_p(T)$ for only compound C completes the work required for this step. However, for chemical reactions containing multiple products C + D (or even C + D + E), an average heat capacity must be calculated based on the mass fractions of C and D produced. Since different molecules contain different bond types, each molecule C, D, or E will contain a different value for heat capacity and each need to be considered. The equation for calculating average heat capacity is shown in Equation 4.6, where X_C and X_D are the mass fractions of compounds C and D, respectively. The calculations for obtaining the mass fractions are shown in Equations 4.7 and 4.8, where m indicates the compound's respective masses. Due to the conservation of mass, Equation 4.9 must be true. In addition, the sum of the fractions of all products must equal unity (Equation 4.10). The procedure for determining the final product masses m_C and m_D can be calculated from chemical Equation 4.2 if the molecular weights and stoichiometric coefficients (a, b, c, and d) are known. A detailed explanation of this calculation can be found in any general chemistry textbook.

$$C_{p,avg} = C_{p,C}X_C + C_{p,D}X_D \tag{4.6}$$

$$X_C = \frac{m_C}{m_C + m_D} \tag{4.7}$$

$$X_D = \frac{m_D}{m_C + m_D} \tag{4.8}$$

$$m_{total} = m_A + m_B = m_C + m_D \tag{4.9}$$

$$X_C + X_D = 1 \tag{4.10}$$

Of course, the result of Equation 4.6 ($C_{p,avg}$) is not a measure of heat itself, and cannot be subtracted from ΔH° directly since they are not both measures of energy. The quantity of heat, Q, absorbed by the products in order to increase the temperature by ΔT is dictated by Equation 4.11.

$$Q_{\Delta T} = m_{total} C_{p,avg} \Delta T \tag{4.11}$$

Refering back to Table 19, heat can also be absorbed by the compounds C and D in the event of a phase change, in which the energy will be stored in the general movements of the molecules. The heat of fusion of a compound, C, is the amount of energy *input* required for C to undergo a phase change from a solid to a liquid (melting). Moreover, the heat of fusion can also indicate the amount of energy *released* by C if it were to undergo solidification from a liquid to a solid. For a compound C, this value should be equivalent (but opposite sign) in either direction (melting or solidifying). Similarly, the heat of vaporization of a compound, C, is the amount of energy *input* required for C to undergo a phase change from vaporization of liquid to a gas, or energy *released* in the event of condensation of C from gas to liquid. To calculate the heat absorbed by such a phase change, Equations 4.12 and 4.13 can be used. Q_{melt} or Q_{vap} can also be referred to as the latent heat. [123]

$$Q_{melt,C} = \frac{m_C}{MW_C} \Delta \mathrm{H}_{fus,C} \tag{4.12}$$

$$Q_{vap,C} = \frac{m_C}{MW_C} \Delta \mathrm{H}_{vap,C} \tag{4.13}$$

During any of these 4 types of phase changes, the overall temperature, T, of the products should not change; all the energy should temporarily be directed exclusively to changing the physical state of the compounds and no change in temperature should occur. The heat of fusion or vaporization of a compound can be found in reference texts or chemical databases. The temperature at which these occur are, of course, specific to the melting point and boiling point of the particular compound.

Combining all of these steps, we are finally able to quantify the adiabatic temperature. It may be convenient to use a spreadsheet or other software to calculate each step in ΔT, since it is ideal to use small increments in temperature which may significantly increase the number of calculations necessary. In a generic example in Table 20 below, I will use increments of 10 K, as shown in the first column. The first column defines the temperature of the products. Using this temperature, we can calculate $C_{p,avg}$ for column 2. Then, using the average heat capacity the various Qs in column 3 can be quantified. All that follows is continually subtracting this determined heat quantity, Q, from the $\Delta H°$ "bank account" until the $\Delta H°$ reaches zero (and the bank account is empty). The temperature at which the total internal energy ΔH is depleted, is the adiabatic temperature. It is key to know the melting and boiling points of all products in order to determine the point at which a switch must be made from calculating Q from heat absorbtion to calculating Q_{melt} or Q_{vap}.

Table 20: Example of adiabatic temperature calculation using a spreadsheet. Notice the last calculation should occur when the total enthalpy reaches zero.

$T_{products}$ (K)	$C_{p,avg}$ for C + D	Energy Requirement	ΔH remaining	Heat sink type
T_1	$C_{p,avg\ @T1}$	$Q_1 = m_{products}*C_{p,avg\ @T1}*(T_2-T_1)$	$\Delta H_1 = \Delta H° - Q_1$	Heat absorbtion
$T_2 = T_1 + 10K$	$C_{p,avg\ @T2}$	$Q_2 = m_{products}*C_{p,avg\ @T2}*(T_3-T_2)$	$\Delta H_2 = \Delta H_1 - Q_2$	Heat absorbtion
$T_3 = T_2 + 10K$	$C_{p,avg\ @T3}$	$Q_3 = m_{products}*C_{p,avg\ @T3}*(T_4-T_3)$	$\Delta H_3 = \Delta H_2 - Q_3$	Heat absorbtion
…	…	…	…	…
$T_x = T_{mp,\ C}$		$Q_{melt} = \Delta H_{fus,C}*m_C/MW_C$	$\Delta H_x = \Delta H_{x-1} - Q_{melt}$	Phase change: melting
…	…	…	…	…
$T_y = T_{mp,\ D}$		$Q_{melt} = \Delta H_{fus,D}*m_D/MW_D$	$\Delta H_y = \Delta H_{y-1} - Q_{melt}$	Phase change: melting
…	…	…	…	…
$T_n = T_{ad}$	$C_{p,avg\ @Tn}$	$Q_n = m_{products}*C_{p,avg\ @Tn}*(T_n-T_{n-1})$	0	Heat absorbtion

If the values for C_p or ΔH_f cannot be found, they can be estimated by looking to similar chemical compounds for reference. Heat capacities are quantities based on the amount of heat stored in a molecule's bonds as they rotate or vibrate. Thus, a molecule containing similar bonds can be used as an analog. It is important to consider ionic vs covalent bonds, as well as intermolecular bonds. Heats of formation can depend on the initial phase of the compound as well as its crystal structure if in the solid phase.

4.2 Research Objectives

4.2.1 Solid State Exothermic Reactions as an Energy Source

The central research objective of this study was to find a candidate solid-state exothermic reaction to use as an energy source and determine its propagation speed. The energy densities of several fuel and oxidizer combinations were calculated, and a list of 18 were chosen for

preliminary experimentation (Table 21). The chemical compounds chosen were required to be in the solid phase and were expected to be generally pyrolitic. However, it was critical that at least one reaction could maintain a steady burn rate, rather than expend itself rapidly and all at once. A steady burn rate implies long-duration heat generation if properly managed as well as the possibly for controlled burning. Thus, the ideal pyrolant candidate is one whose propagation rate is naturally slow, and which does not require additives or other heat sinks to slow its propagation to a desirable rate. Although this is the desirable behavior, methods can be employed for pyrolants with rapid burn rates in an attempt to slow them down.

Table 21: List of 18 fuel and oxidizer reaction combinations to test for slow reaction propagation potential.

#	Fuel	Oxidizer	Energy Density (kWh/kg)	#	Fuel	Oxidizer	Energy Density (kWh/kg)
Group 1: Lithium Peroxide				**10**	Al	MnO_2	1.35
1	B	Li_2O_2	2.09	**11**	Al	MoO_3	1.31
2	MgB_2	Li_2O_2	2.83	**Group 3: Magnesium & Teflon**			
3	Mg	Li_2O_2	2.28	**12**	Mg	Fe_2O_3	1.29
4	TiB_2	Li_2O_2	1.68	**13**	Mg	Fe_3O_4	1.2
5	Si (nano)	Li_2O_2	2.83	**14**	Mg	CuO	1.28
6	Zr	Li_2O_2	1.48	**15**	Mg	MnO_2	1.54
Group 2				**16**	Mg + Si	O_2	8.57
7	Ti	B	1.54	**17**	Mg	$(C_2F_4)_n$	4.1
8	Ti	C	0.85	**18**	Li	$(C_2F_4)_n$	3.4
9	Si (nano)	O_2	9.04				

In order to measure burn propagation rates, a test cell was designed to monitor combustion along a length of reaction powder. Prior to any analysis within the propagation test cell, a series of experimental tests were devised to evaluate each of the 18 exothermic reactions. These preliminary evaluations shortened the experimental process considerably, rapidly eliminating reactions that were violently exothermic and avoided breakage of the test cell. For this selection process, reactions were organized into groups roughly according to their chemical compositions in order to distinguish ignition patterns.

4.3 Experimental Methods

4.3.1 Production of Solid Pyrolant Mixtures

Stoichiometric quantities of solid fuel and oxidizer were measured on an analytical balance. The powders were homogeneously mixed by hand-shaking in a glass serum vial, followed by grinding in a mortar and pestle, and then finally loading into an empty steel vial to be shaken for 15 minutes by a mixer mill. The resulting powders are shown in Figure 49.

Figure 49: A view of a select number of the 18 pyrolant powders, after homogenizing the fuel and oxidizer.

4.3.2 Selection of the Ideal Pyrolant Candidate

A selection process was devised to determine the best pyrolant candidates and to narrow down to a suitable number for initial testing. The pyrolants were subjected to 3 preliminary experimental tests: a) a wire ignition and explosivity test, b) thermogravimetric analysis (TGA) and c) a vertical propagation test. Each test was designed to assess one or multiple variables to

select the pyrolant candidate that would require the least amount of manipulation or chemical additives to propagate slowly.

4.3.2.1 Wire Ignition and Explosivity Test

At the outset, pyrolants were analyzed for their ability to be ignited with a nichrome wire, as this is ultimately the ignition device within the propagation reaction chamber. Simultaneously, their physical explosivity was assessed. A coil of nichrome wire was placed at the bottom of a small, open, ceramic crucible (Figure 50). Approximately 0.5 g of pyrolant was placed on top and around the coil, covering it completely. The nichrome wire was heated for 5 seconds by generating a current within it in order to ignite the pyrolant powder.

Figure 50: A post-combustion image of burned solid pyrolant in a ceramic crucible, atop a coiled nichrome wire. The reaction product has hardened around the wire coil.

4.3.2.2 Thermogravimetric Analysis (TGA)

Pyrolants which passed the ignition and explosivity test proceeded to be analyzed through thermogravimetric analysis (TGA). Pure fuel and oxidizer powders were also analyzed. The instrument contained an alumina pan attached to a platinum hang wire (Figure 51). The samples

were heated to 600 °C at a rate of 10 °C/min under a flow of air. The moisture content of the powders, evolution of gases, and ignition temperatures were determined by monitoring mass fluctuations in the powders.

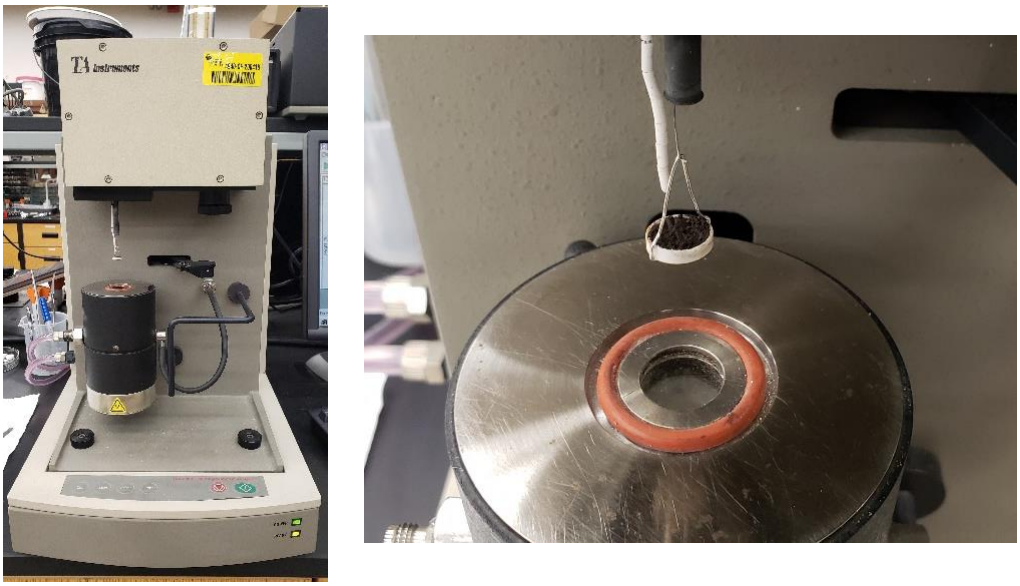

Figure 51: Thermogravimetric analysis (TGA) was used to monitor mass fluctuations of the pyrolants during ignition. The right image shows a sample of titanium and boron pyrolant mixture hanging on the weighing pan.

4.3.2.3 Vertical Propagation Test

Pyrolants which passed the ignition and explosivity test proceeded to a vertical propagation test rig, shown in Figure 52. This rig consists of a cylindrical chamber with removable bottom and top covers, all constructed of POCO graphite. A small channel was machined from the top through the bottom down the long axis of the cylinder, excluding the lid and base (Figure 52a). This chamber contains the pyrolant powder during combustion. Four thermocouples penetrate the side of the cylinder (Figure 52c) and enter the central channel, embedding themselves in the center of the pyrolant powder. The thermocouple holes are spaced 1 cm apart. At the bottom of the cylinder, a hollow alumina tube is inserted horizontally, which holds the nichrome ignition wire (Figure 52b). The alumina tube acts as insulation to shield the ignition wire from the graphite surroundings,

which are highly electrically conductive, and can interfere with wire heating. A hole is cut in the alumina tube where it will lie under the narrow channel so the pyrolant powder makes contact with the ignition wire (Figure 52d), but does not fall through the bottom of the graphite cylinder.

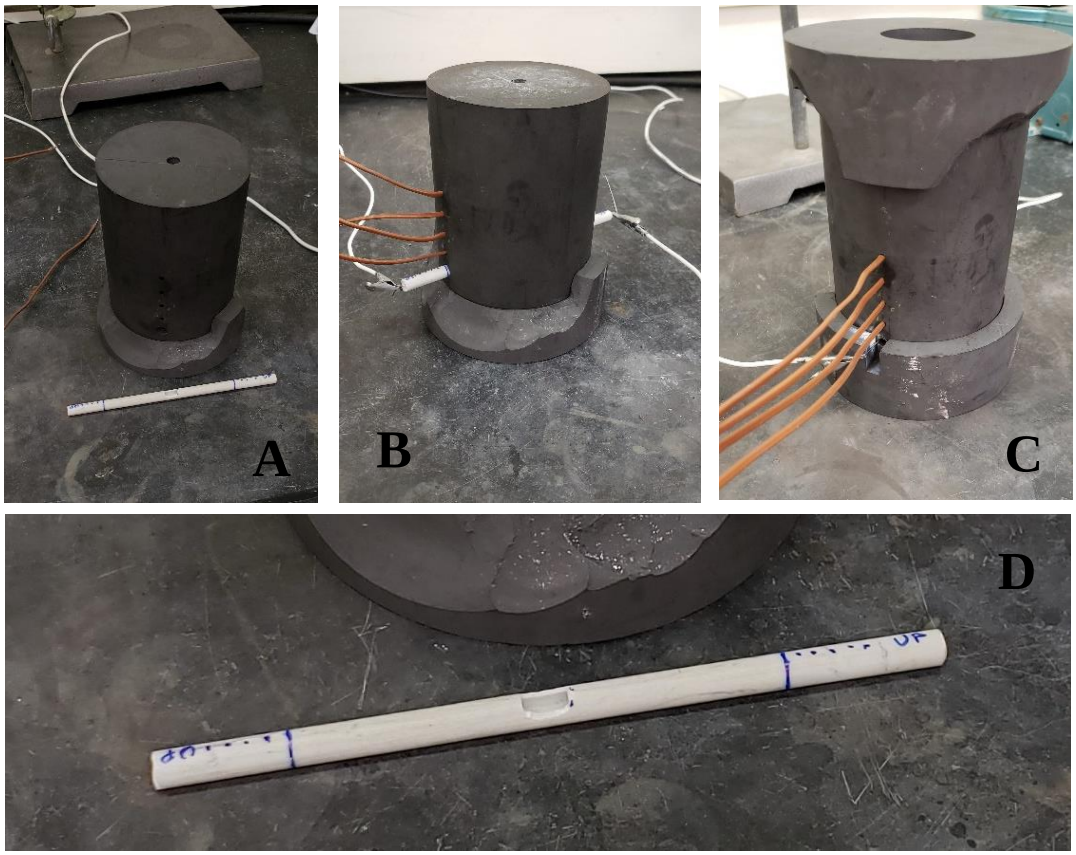

Figure 52: (A) The vertical graphite test chamber, showing the top opening of the channel which holds the pyrolant. (B) A hollow alumina tube hods the ignition wire and is inserted horizontally through the bottom of the graphite cylinder. (C) 4 thermocouples are inserted into the side of the cylinder and reach the interior of the channel where they make contact with the pyrolant. (D) A close-up of the alumina tube, showing a cut hole designed to align with the pyrolant channel.

Thus, the pyrolant placed in this vertical propagation cell ignites from the bottom of the cylinder and propagates upwards. The nichrome wire is heated for 7 seconds to ignite the pyrolant. Pyrolant was packed into the central chamber until it reached 1 cm above the topmost thermocouple.

4.3.3 Thermocouple Coatings

Observations of noise in the temperature readings during pyrolant burning resulted in various attempts to coat thermocouples using different compounds.

Polysilizane was applied to 4 bare, welded thermocouple wires using a cotton applicator, shown in Figure 53a. The liquid was applied heavily and dried in an oven at 180 °C to harden.

A mixture of boron nitride and isopropanol was spray-coated onto 4 bare, welded thermocouple wires using a spray coater attached to compressed air (Figure 53b). These thermocouples were left to air dry.

Figure 53: (A) Stripped thermocouples were coated with polysilizane applied with cotton applicator. (B) Stripped thermocouples were coated with a mixture of boron nitride powder in isopropyl alcohol using a spray coater.

Propagation rates were evaluated for each pyrolant reaction within specially constructed propagation test cells. Two nearly identical cells were machined: one of ceramic and the other of graphite (Figures 54 and 54). Each cell consists of 4 ceramic or graphite blocks which are cut such that when assembled, they create an empty rectangular space between them. A stainless steel base and lid, as well as bolts, hold the 4 blocks in place.

For each experiment, approximately 1 g of pyrolant mixture is loaded into the rectangular chamber space, which when completely closed compresses the powder gently to form a rectangle, as shown in Figure 54c. A nichrome wire at one end of the rectangular chamber is coiled where it is imbedded in the pyrolant, and the wire ends extend out each side of the cell to be connected to a variable AC transformer (Variac); this placement is shown in Figure 54b. As the powder is ignited from one side to the other, thermocouples inserted at 1 cm intervals along the length of the sample measure the heat generated. Ten channels are machined perpendicular to the sample chamber (Figure 54d) which hold the thermocouples at precise intervals from each other and ensure they do not shift during burning. Only 4 of these channels are used at a time, but additional channels allow for changing the thermocouple placement along the pyrolant sample if desired. Each reaction is ignited by heating the nichrome wire for 7 seconds. The equal spacing between the 4 thermocouples allows for a rate calculation as the combustion front passes over each thermocouple. Figure 54d shows the pyrolant chamber after a successful ignition of pyrolant that began looking as that of Figure 54c.

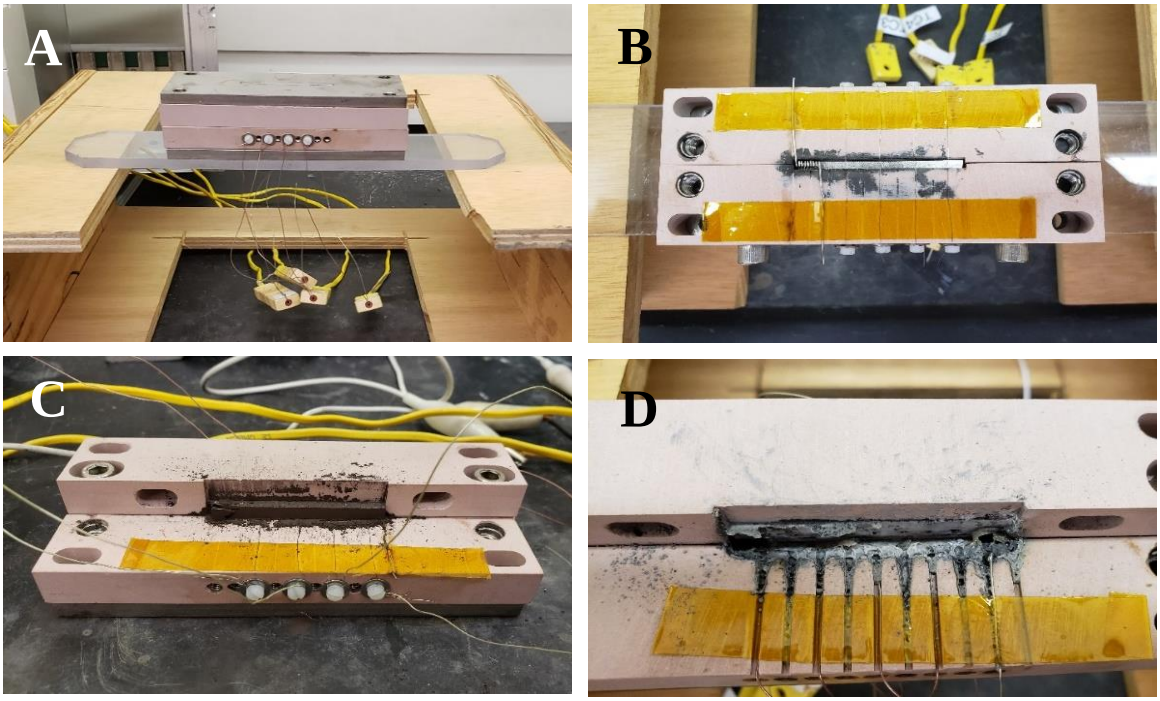

Figure 54: (A) The completely assembled ceramic propagation rate cell. (B) A view to the interior of the cell, showing thermocouples evenly spaced and coiled nichrome wire. (C) One of 4 ceramic blocks removed to show interior compressed pyrolant shape. (D) Post-reaction residue after successful ignition of pyrolant.

The graphite chamber is shown in Figures 55a-d. The interior rectangular chamber of this cell has identical dimentions to that of the ceramic cell in Figures 54a-d. Thermocouple channels machined in this cell are made slightly deeper and wider to accommodate thicker guage thermocouple wire if this is desired.

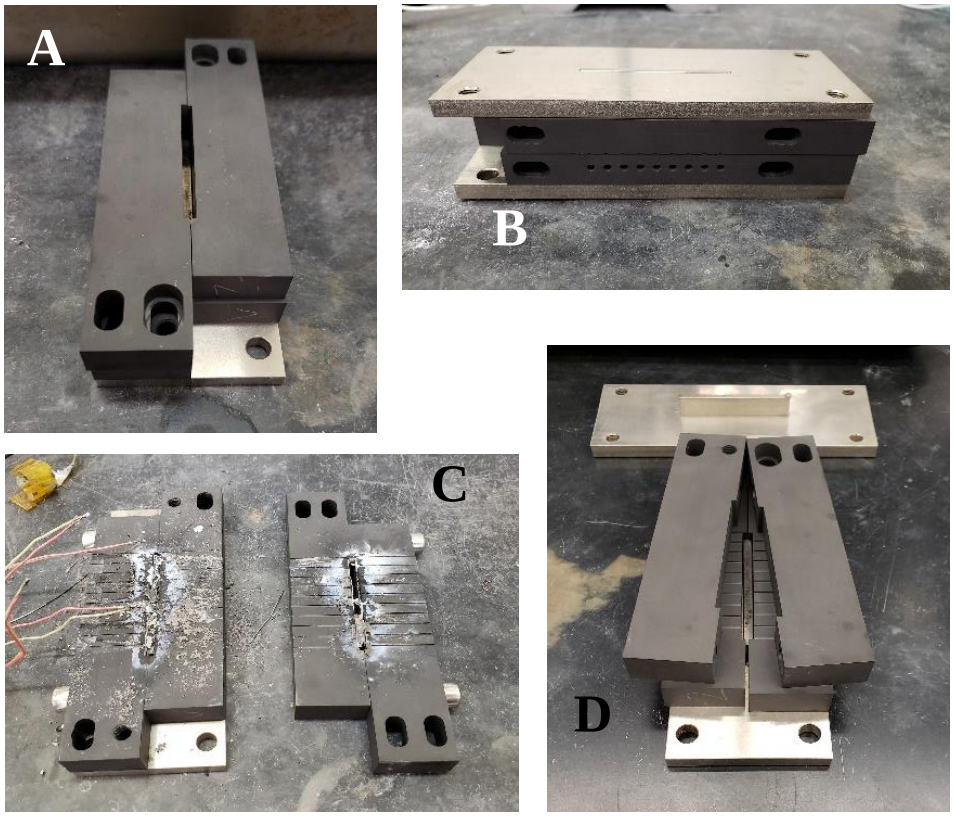

Figure 55: (A) The graphite propagation cell, showing the central test chamber formed from the blocks once they are assembled. (B) The completely assembled graphite propagation cell. (C) Burned pyrolant residue after a successful ignition. (D) View of graphite blocks nearly assembled. The stainless steel top and base contain a protruding slot which fits within the rectangular chamber to contain the pyrolant.

In order to control the atmosphere surrounding the burning pyrolant, a purge box was constructed to house the propagation cell (Figure 56). The box consists of an acrylic enclosure, each side of which is solvent welded at the edges. The box is placed on top of a table which holds the propagation cell and thermocouple ports, and is held tightly onto a gasket (orange) with 8 screws. A gas inlet is located at the bottom of the chamber, and an outlet is placed near the top of one side of the acrylic box which allows a continuous flow of gas to purge the environment of any air (particularly oxygen). The thermocouple and ignition wires are threaded through a port in the bottom of the table which has been made gas-tight by filling with epoxy. Prior to pyrolant ignition,

the box is purged with the desired gas for 15 minutes and gas continues to flow during ignition and burning.

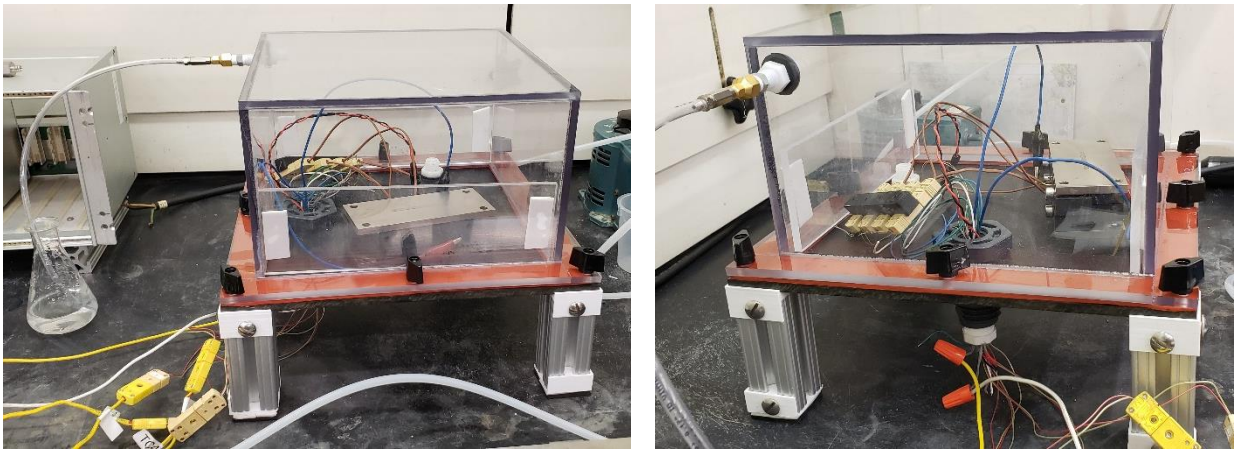

Figure 56: A purge box allows control of the environment surrounding the propagation cell. A continuous flow of gas enters and exits the box, purging of air before and during pyrolant ignition.

4.4 Results

4.4.1 Pyrolant Selection

Although the 18 pyrolant mixtures were chosen based on their high energy densities, it was initially unknown if each pyrolant would ignite via a nichrome wire, how explosively the pyrolants would react, or if any of the pyrolant reactions would incur harmful damage to the main propagation cell or its components. Pyrolants which failed to ignite via the nichrome wire test did not proceed to the next selection test, since they ultimatly would not combust within the propagation cell. Pyrolants which underwent large visual or audible detonations within the crucible were also not selected as immediately viable for propagation experiments. However, such excessively energetic pyrolant mixtures could become useful in the future as additives to slower-burning solid pyrolant reactions in order to speed up reaction propagation.

Groups of pyrolant mixtures which contained similar compounds reacted similarly to each other in the ignition and explosivity tests. The results for all tests are summarized in Table 24.

Reactions between lithium peroxide and titanium diboride (Li_2O_2 + TiB_2; reaction #4) as well as aluminum and manganese dioxide (Al + MnO_2; reaction #10) were unable to be ignited via the nichrome wire method. Pyrolants containing magnesium (Mg), zirconium (Zr), and teflon (C_2F_4) exhibited loud cracking explosions often accompanied by visible flashes of light. Although the reaction between lithium peroxide and silicon (Li_2O_2 + Si; reaction #5) was not characterized as explosive, the reaction combusted rapidly.

Thermogravimetric analysis of the remaining pyrolants resulted in successful ignition and burning for the majority of samples. However, the reaction between titanium and boron (Ti + B; reaction #7) did not result in any ignition at temperatures up to 600 °C. Figure 57 shows the TGA results of all successful pyrolant mixtures containing lithium peroxide. The samples showed insignificant mass loss up to 350 °C, and at approximately 350 °C, all samples exhibited a sharp decrease in mass. Between 400 – 450 °C samples show an inconsistent degree of mass gain, followed by a second decline in mass. The values of these changes are recorded in Table 22.

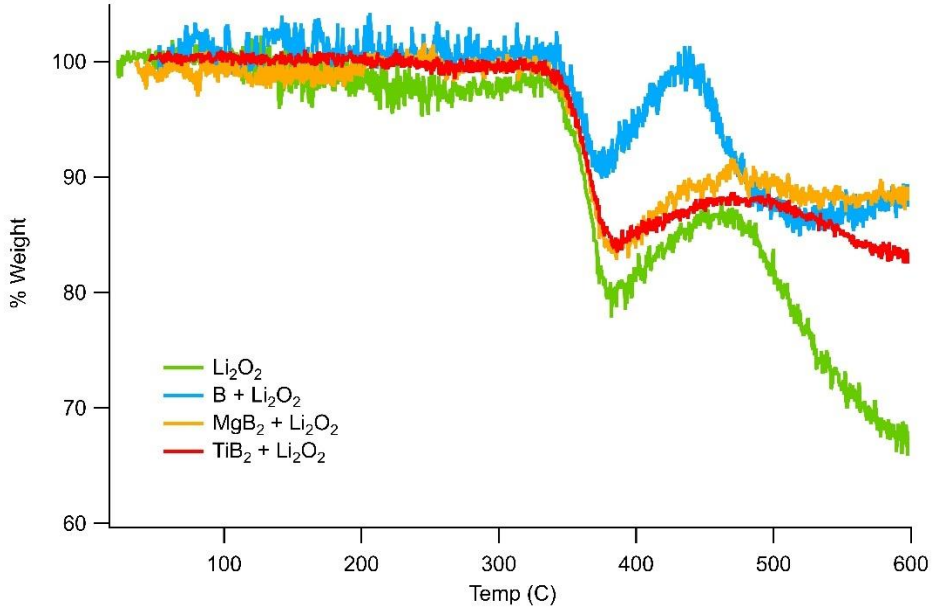

Figure 57: Thermogravimetric analysis (TGA) of pure lithium peroxide powder and 3 stoichiometric pyrolant reaction mixtures.

Table 22: Values of %weight at 350°C as well as sample masses at 600°C for each of the pyrolant samples in Figure 57.

Pyrolant Sample	$M_{350°C}$ (% weight)	$M_{600°C}$ (% weight)
Li_2O_2	81.1	67.2
B + Li_2O_2	90.5	87.2
MgB_2 + Li_2O_2	84.4	88.1
TiB_2 + Li_2O_2	84.8	82.7

Pyrolants which passed the ignition and explosivity test were subject to the graphite propagation test regardless of TGA test results. Experiments in this vertical propagation cell were meant to be analagous to the horizontally-lying propagation cells, and were designed to analyze the interactions between the pyrolant and thermocouples. For all pyrolants, burning of the powders resulted in one or more problematic interactions with the thermocouples. The burn products often formed a hardened mass surrounding the thermocouple junction, melted the thermocouple junction altogether, or the hardened solid product replaced the thermocouple junction after it was melted, all of which can produce false temperature readings. Two examples of thermocouple noise are displayed in Figures 58a and b. Figure 58a is almost ideal, but peaks are closely spaced, indicating a fast propagation rate and thermocouples 3 and 4 (TC3, TC4) seem to experience noise between 1 and 2 seconds. Figure 58b shows temperature curves commonly seen for excessive electrical contact between the 4 thermocouples. Thermocouples 1, 3, and 4 show clear repetition in their peaks, which align with the peaks in neighboring thermocouples in multiple instances. Additionally, thermocouple 4 in Figure 58b also shows the signal produced when a complete breakage occurs in the thermocouple junction. This can be seen at about 9.5 seconds as the temperature curve shoots above the maximum range of a K-type thermocouple.

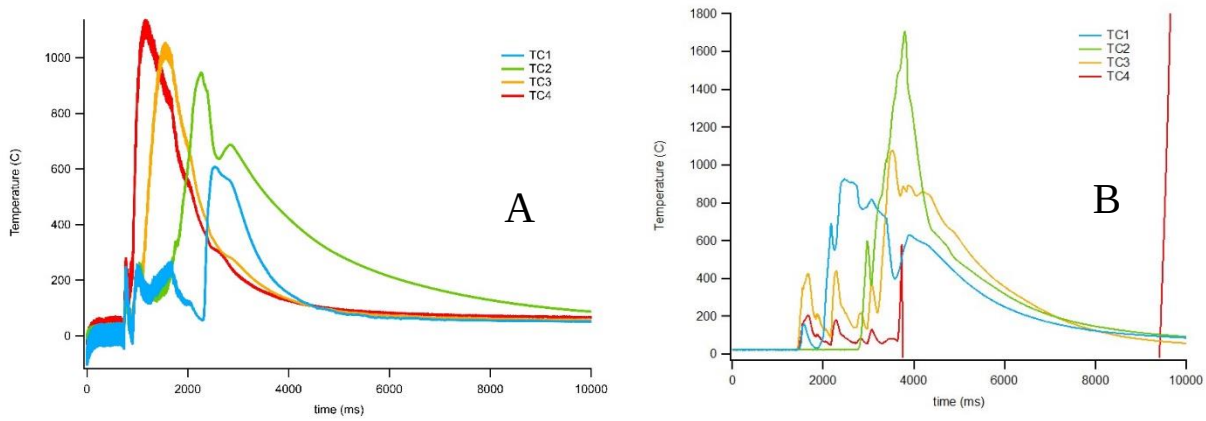

Figure 58: First vertical graphite cell reactions. (A) Reaction monitored with standard thermocouple wires. (B) Reaction monitored with one of the thermocouple wire pairs in electrical contact with the graphite cell.

Thus, of the 18 pyrolant reaction candidates assessed, mixtures with lithium peroxide and boron (Li_2O_2 + B; reaction #1), magnesium diboride (Li_2O_2+ MgB_2; reaction #2), as well as aluminum and molybdenum oxide (Al + MoO_3; reaction #11) were the leading candidates. Reaction 11 was not chosen among the 3 due to its lower energy density as well as the availability of molybdenum oxide. Reaction 1 containing boron oxide was ultimately chosen due to the availability of boron powder.

Table 23: Results of the selection tests for each of the 18 pyrolants. A dash ("-") indicates the reaction did not proceed to that test.

#	Reaction	Nichrome Wire Test	TGA <600°C	Graphite Cell Test
Group 1: Lithium Peroxide				
1	Li_2O_2 + B	✓ Ignition (fizzle)	✓ Burn	TC breakage
2	Li_2O_2 + MgB_2	✓ Ignition (fizzle)	✓ Burn	TC breakage
3	Li_2O_2 + Mg	Ignition (explosive)	-	-
4	Li_2O_2 + TiB_2	No ignition	✓ Burn	-
5	Li_2O_2 + Si	Ignition (rapid, noiseless)	✓ Burn	-
6	Li_2O_2 + Zr	Ignition (explosive)	-	-
Group 2				
7	Ti + B	Ignition (explosive)	No Burn	-
8	Ti + C	*Postponed*	-	-
9	Si + O_2(g)	*Postponed*	-	-
10	Al + MnO_2	No ignition	-	-
11	Al + MoO_3	✓ Ignition (slow)	✓ Burn	TC breakage
Group 3: Magnesium and Teflon				
12	Mg + Fe_2O_3	Mg: too energetic	-	-
13	Mg + Fe_3O_4	Mg: too energetic	-	-
14	Mg + CuO	Mg: too energetic	-	-
15	Mg + MnO_2	Mg: too energetic	-	-
16	Mg + Si + O_2(g)	Mg: too energetic	-	-
17	C_2F_4 + Mg	C_2F_4: too energetic	-	-
18	C_2F_4 + Li	C_2F_4: too energetic	-	-

4.4.2 Thermocouple Noise Reduction

Prevention of thermocouple melting using a liquid polysilizane coating slightly reduced the occurances of complete breakage of the thermocouples. However, application of the coating was imperfect and prone to errors, since the polysilizane dried as a thick crust, which easily crumbled when the thermocouple junction was inserted into the pyrolant powder. As shown in Figure 59, the coating did not eliminate electical noise.

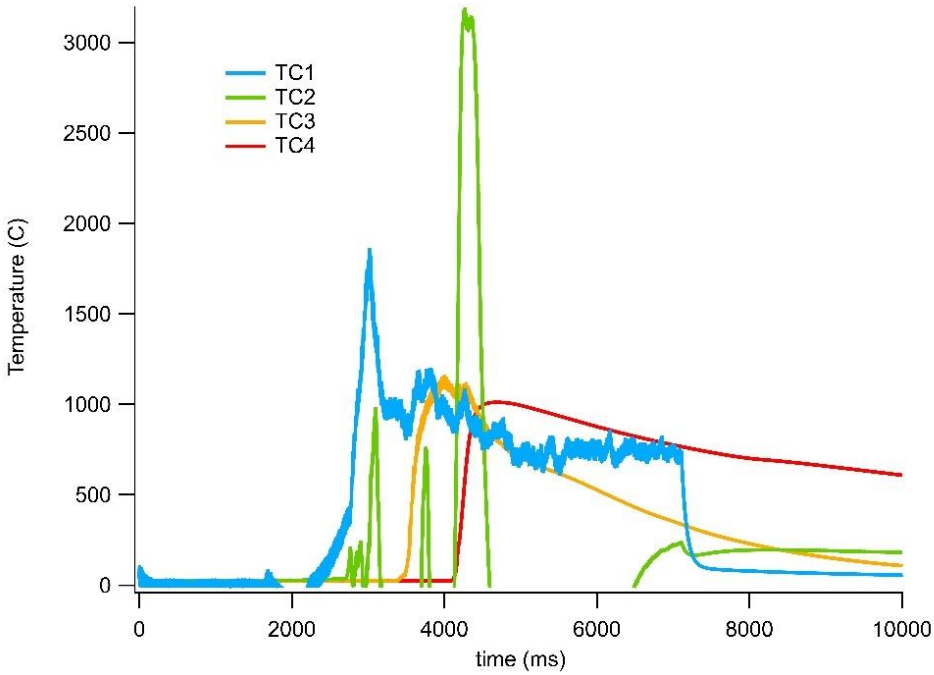

Figure 59: Vertical graphite cell reaction using polysilizane-coated thermocouples to prevent melting.

Coatings of boron nitride suffered less crumbling and remained on the thermocouple wires during insertion into the propagation cell. However, as shown in Figure 60, boron nitride seemed to provide little to no protection for electrical interferance.

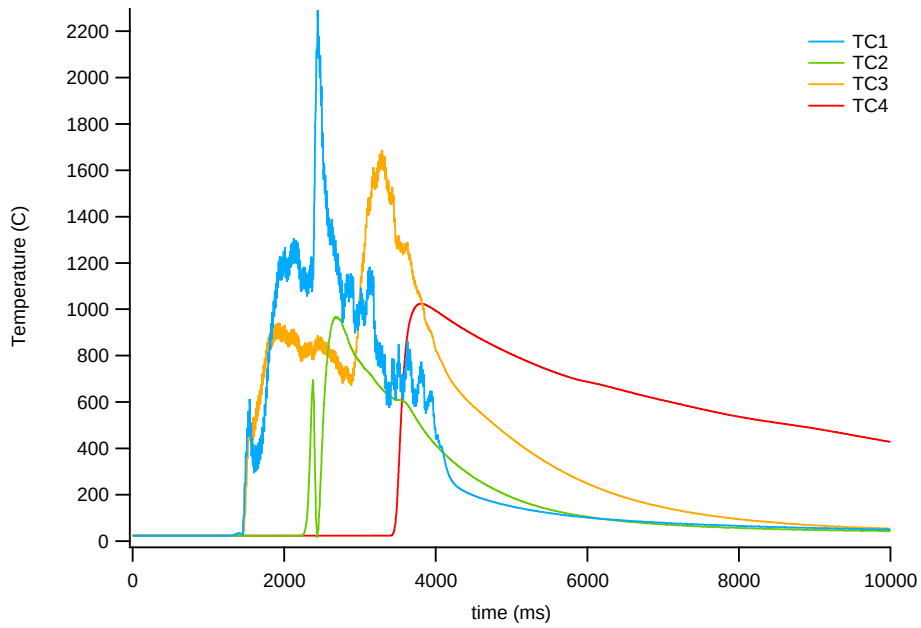

Figure 60: Vertical graphite cell reaction using boron nitride-coated thermocouples to prevent electrical interferance within the pyrolant powder.

4.5 Discussion

4.5.1 Lithium Peroxide + Boron Reaction Mechanism

It was determined via thermogravimetric analysis that the pyrolysis reaction between boron and lithium peroxide proceeds through 3 elementary steps, shown in Equations 4.14-4.16. Equation 4.17 shows the summation of these elementary steps to form the overall chemical equation. The first two elementary steps both involve the evolution or sequestration of a gas, which allowed us to elucidate those steps via TGA.

$$Li_2O_2\ (s) \rightarrow\ Li_2O\ (s) +\ O_2(g) \tag{4.14}$$

$$B\ (s) +\ O_2\ (g) \rightarrow\ B_2O_3\ (s) \tag{4.15}$$

$$Li_2O\ (s) +\ B_2O_3\ (s)\ \rightarrow\ Li_2B_4O_7(s) \tag{4.16}$$

$$\boldsymbol{Li_2O_2\ (s) +\ B\ (s) \rightarrow\ Li_2B_4O_7\ (s)} \tag{4.17}$$

The first elementary step in Equation 4.14 describes the decomposition of lithium peroxide to form lithium oxide and oxygen gas. This decomposition is observed at 350°C in all of our pyrolant samples containing Li_2O_2 in the form of a significant mass decrease. In the pure lithium peroxide sample in Figure 61, the decomposition results in a mass loss of 24.5wt%. These TGA results compare well to those in the literaure of lithium compounds which show a similar decline in mass for lithium peroxide at a temperature near 350°C (Figure 62). [125] Assuming the reaction in Equation 4.14 goes to completion, the theoretical yield of lithium oxide (Li_2O) is 34.8 wt%, which is in agreement with the wt% value of Li_2O_2 observed in the literature. However, our lithium peroxide sample displayed in green in Figure 61 does not reach this theoretical value before a rapid mass increase occurs between 400-500°C. This indicates Li_2O_2 decomposition was incomplete before the formation of an unknown species, which seems to subsequently decompose between 450-500°C.

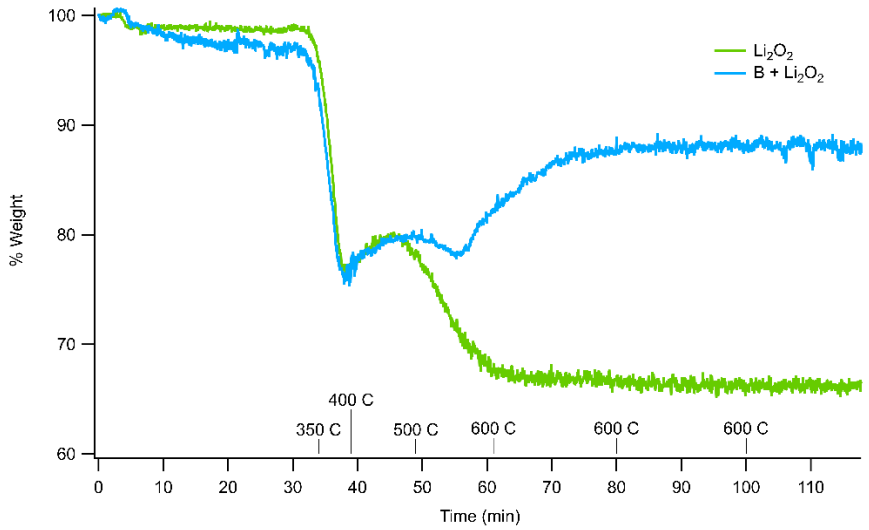

Figure 61: TGA of a pyrolant mixture containing Li_2O_2 (blue) as compared to a pure Li_2O_2 sample (green) shows the differences in behavior above 550°C as the pyrolant oxidizes leading to a mass increase, while pure Li_2O_2 does not.

The lithium peroxide curve eventually reaches 67.2 wt%; 65.2 wt% would indicate 100% decomposition. However, Figure 57 shows that the pyrolant mixtures do not plateau at a lower

mass, as does the pure oxidant. An isothermal hold of our boron pyrolant mixture (blue curve) at 600°C (Figure 61) confirmed an increase in mass up to 88.3 wt%. This occurs as oxygen evolves from the first elementary step (Equation 4.14) and reacts with boron to form boron trioxide (Equation 4.15). We predict that a TGA run flowing air instead of argon gas over the sample would allow the pyrolant mixture B + Li_2O_2 to reach its maximum yield by supplying an excess amount of oxygen gas. Table 24 lists the final weight percent values for the curves in Figure 61 at temperatures 350°C and 600°C, as well as the theoretical wt% values given complete decomposition of Li_2O_2 at 350°C and complete oxidation of B at 600°C. We predict that the products Li_2O and B_2O_3 from the first two elementary reactions then react to produce lithium borate (Equation 4.16). Similarly, mixtures of lithium peroxide with magnesium diboride (MgB2) and titanium diboride (TiB_2) should recover their mass in an extended isothermal run at 600°C in the TGA with a flow of excess oxygen. In addition to B_2O_3 they should form the oxides MgO and TiO_2.

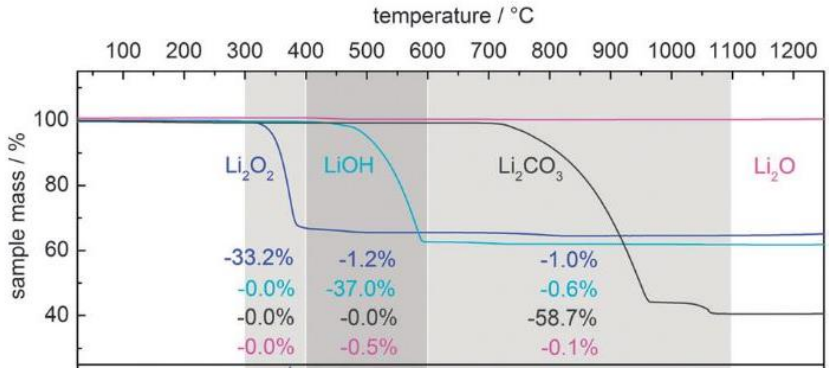

Figure 62: TGA results of lithium compounds held to temperatures of 1200°C. [125]

Table 24: TGA percent weight values of 4 samples at 2 different temperatures, as compared to their theoretical weight percents after the decomposition of lithium peroxide and after oxidation of the solid fuel. The decomposition of lithium peroxide should occur at 350°C.

Pyrolant Sample	$M_{350°C}$ (% wt)	$M_{350°C, theoretical}$ (% wt)	$M_{600°C}$ (% wt)	$M_{600°C, theoretical}$ (% wt)
Li_2O_2	75.5	65.2	67.2	65.2
B + Li_2O_2	75.7	69.9	88.3	100

4.5.2 Propagation of Lithium Peroxide + Boron Pyrolant

One ideal propagation reaction between lithium peroxide and boron is shown in Figure 63. The large temperature peaks in the graph mark each moment the combustion front passes a thermocouple as it proceeds along the length of pyrolant. In addition to Figure 63, the propagations shown in Figures 64-66 depict nearly ideal propagation results as compared to the problematic results shown in Figures 58b, 59, and 60. They each convey a significant noise reduction, no thermocouple breakage (with the exception of Figure 64), and minimal electrical interferance. However, temperature fluctuations can be caused by other phenomena, such as heat conduction from the ignition wire, heat conduction eminating from the combustion front (preheating), phase changes, and electrical interferance.

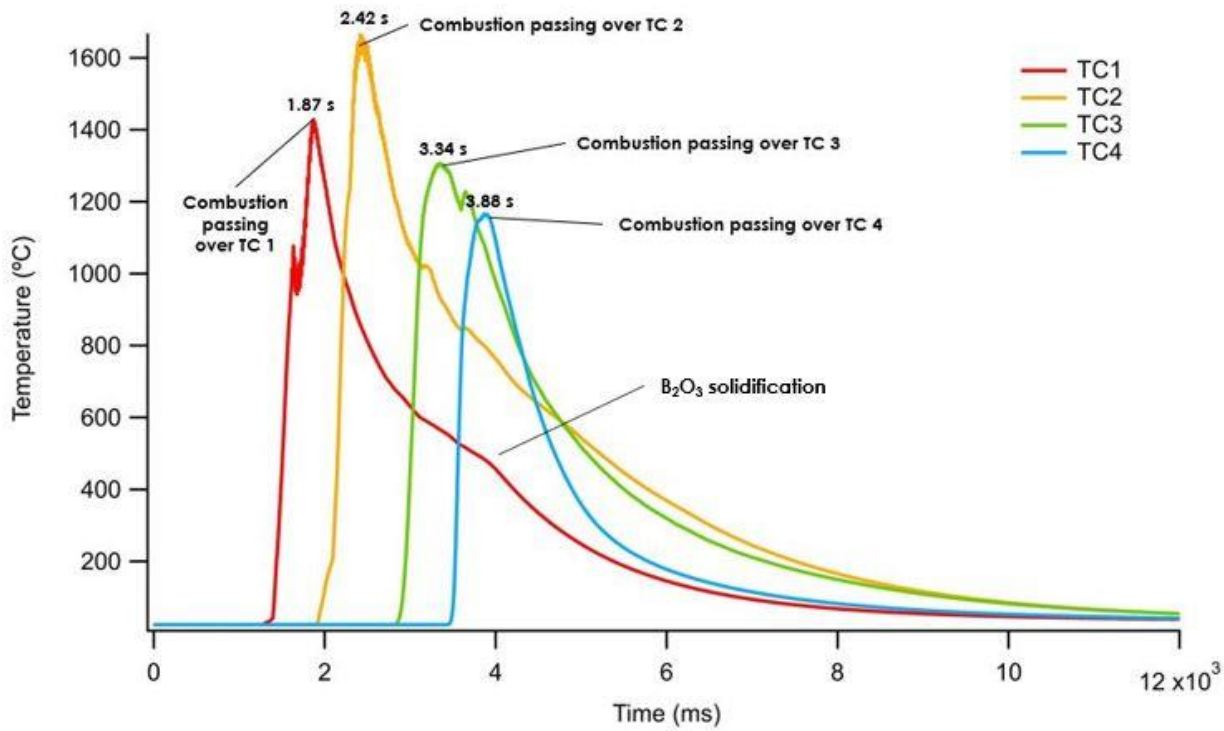

Figure 63: Reaction propagation for the reaction of lithium peroxide and boron using the graphite propagation cell and a nichrome wire.

4.5.2.1 Wire Heating

As current flows through the ignition wire, some heat generated may begin to conduct through the pyrolant regardless of whether the pyrolant has ignited. This may occur if the ignition wire is activated, the pyrolant rapidly ignites and causes the combustion front to pass quickly over the first few thermocouples, then heat directly from the ignition wire reaches the nearest thermocouple: likely thermocouple 1, causing a secondary spike in temperature.

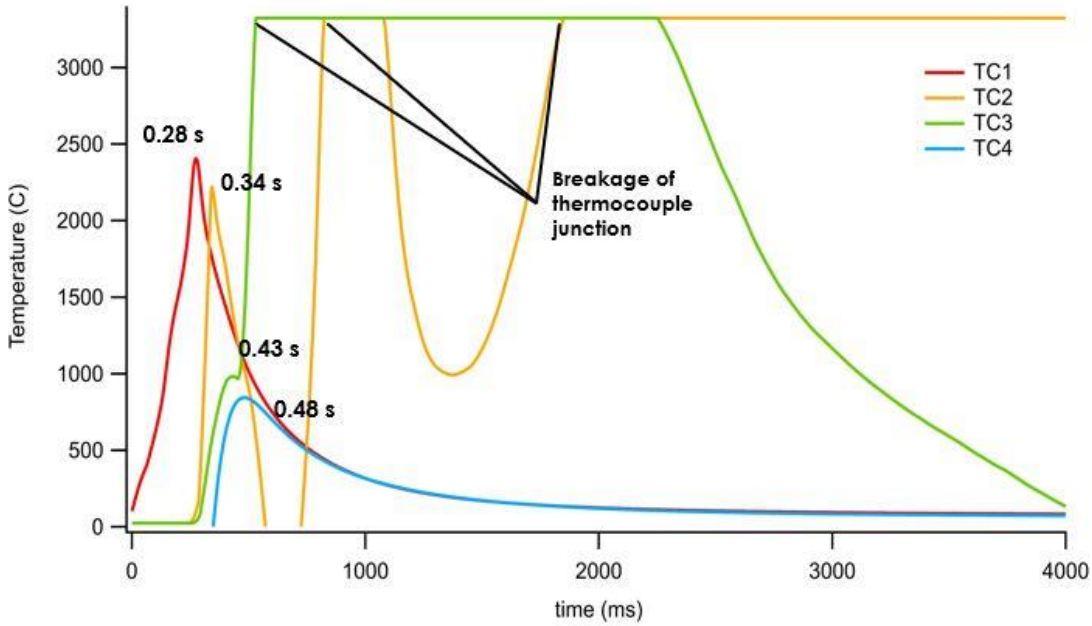

Figure 64: Reaction propagation for the reaction of lithium peroxide and boron using the graphite propagation cell and a tungsten wire. The flatlining of the thermocouples above 3000°C indicates a breakage of the thermocouple junction. This propagation occurred the most rapidly (combustion front passes over TC1 at <0.5s), and resulted in the fastest propagation rate.

4.5.2.2 Preheating

Heat conduction traveling forward from the point of burning pyrolant can cause preheating within the powder. Although similar to wire heating, the origin of the conduction is from the burning pyrolant itself rather than the ignition wire. Preheating causes downstream pyrolant to increase in temperature prior to it fully combusting. An example of this can be seen in TC2 of Figure 63 at t=2 ms, where there is a slight change in slope of the temperature curve at 200°C. Furthermore, this temperature fluctuation arises at a time between the combustion front leaving TC1 and reaching TC2. Moments after the preheating in the TC2 region, TC2 experiences the wave front of burning pyrolant.

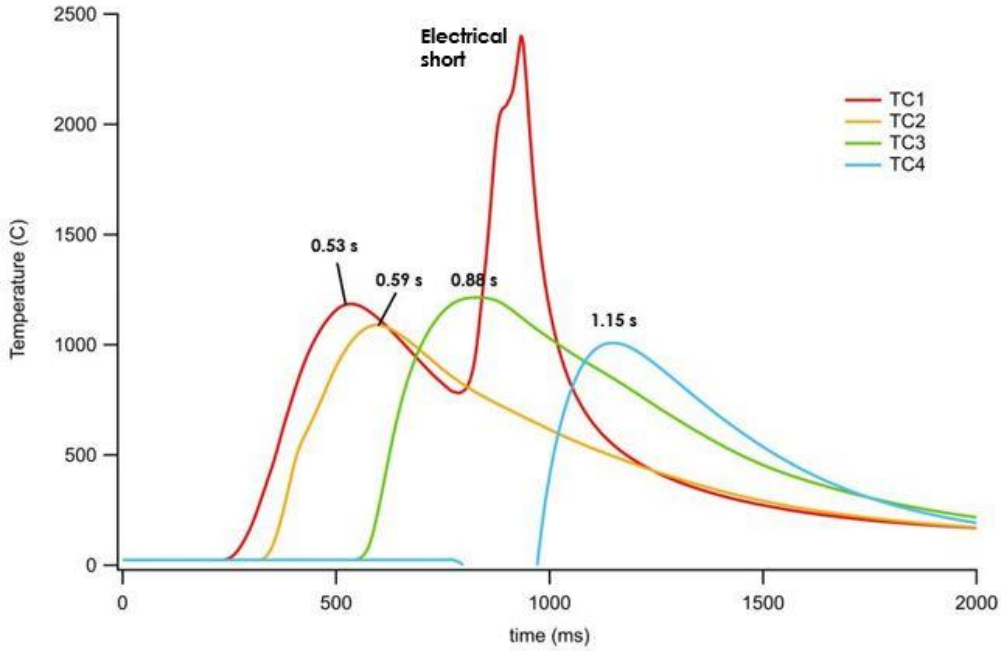

Figure 65: Reaction propagation for the reaction of lithium peroxide and boron using the graphite propagation cell and a tungsten wire. This reaction resulted in significant wire heating, as observed in TC1. This propagation bears strong resemblance to the propagation shown in Figure 66, a promising result for achieving reproducability.

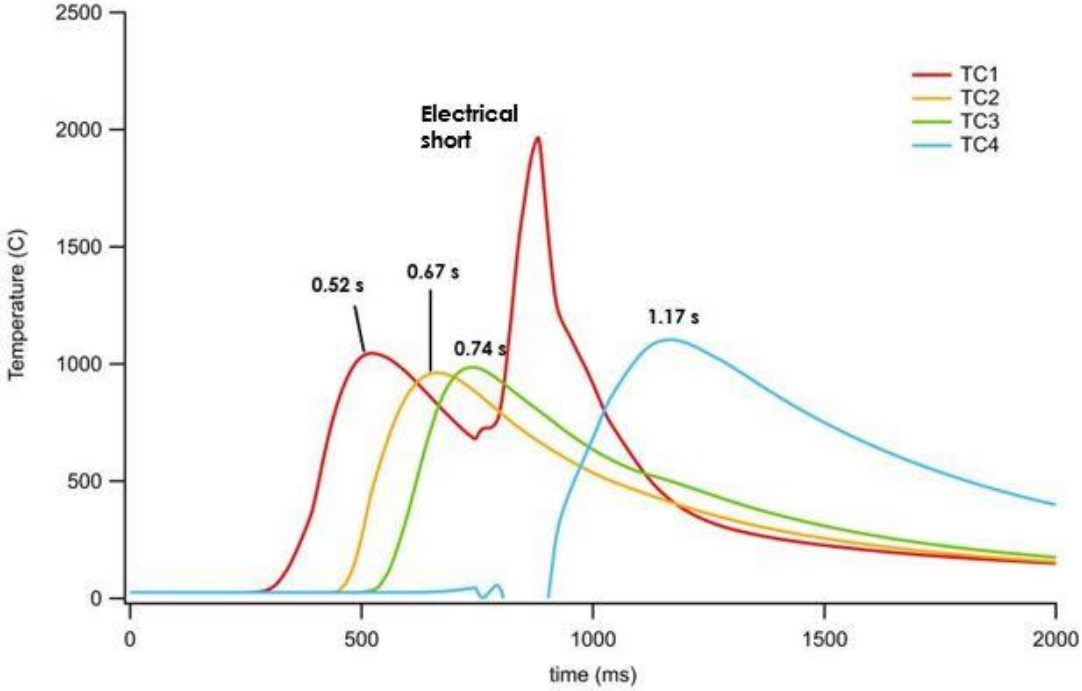

Figure 66: Reaction propagation for the reaction of lithium peroxide and boron using the graphite propagation cell and a tungsten wire. This reaction resulted in significant wire heating, as observed in TC1. This propagation bears strong resemblance to the propagation shown in Figure 65, a promising result for achieving reproducability.

4.5.2.3 Phase Change

As discussed in section 4.1.2, heat can be absorbed by our products during melting or vaporization, and heat can be released via solidification or condensation. The melting and boiling points of the intermediate and overall products of the reaction between boron and lithium peroxide are listed in Table 25. The relatively low melting point of boron trioxide (B_2O_3) allows its phase change to be seen in some of our propagation curves, notably in Figures 63 and 67.

Table 25: The melting and boiling points for anticipated reaction products. *The boiling point of $Li_2B_4O_7$ was estimated from $Na_2B_4O_7$.

Product	Melting Point (°C)	Ref.	Boiling Point (°C)	Ref.
Li_2O	1843	[124]	-	-
B_2O_3	450	[126]	1860	[127]
$Li_2B_4O_7$	1190	[124]	1873	*

4.5.2.4 Electrical Interferance

An extreme example of electrical interferance was shown in Figure 58b. Due to the nature of our experimental set up, our 4 thermocouples should experience a rise in temperature in chronological order. There should be little cause for peaks to be mirrored in multiple thermocouples at the same instant in time. Figure 58b shows various instances where thermocouples 1, 3, and 4 are all experiencing simultaneous temperature peaks. Unlike other temperature peaks, these fluctuations are caused by stray electrons. Since the reaction between boron and lithium peroxide is a reduction-oxidation (redox) reaction, electrons migrating within the pyrolant can be inadvertently channeled through the thermocouple wires, producing electrical interference that can behave like a temperature increase. Due to the electrical conductivity of the graphite cell, electrons entering the graphite can then migrate to neighboring thermocouples. In a case of mild interferance these perturbations can be identified by looking for “bumps” in a

temperature curve that occur at the same time as the burning wave front in another thermocouple. In Figure 63 for example, TC2 exhibits a slight temperature increase at the same time that the burning passes TC3 and TC4.

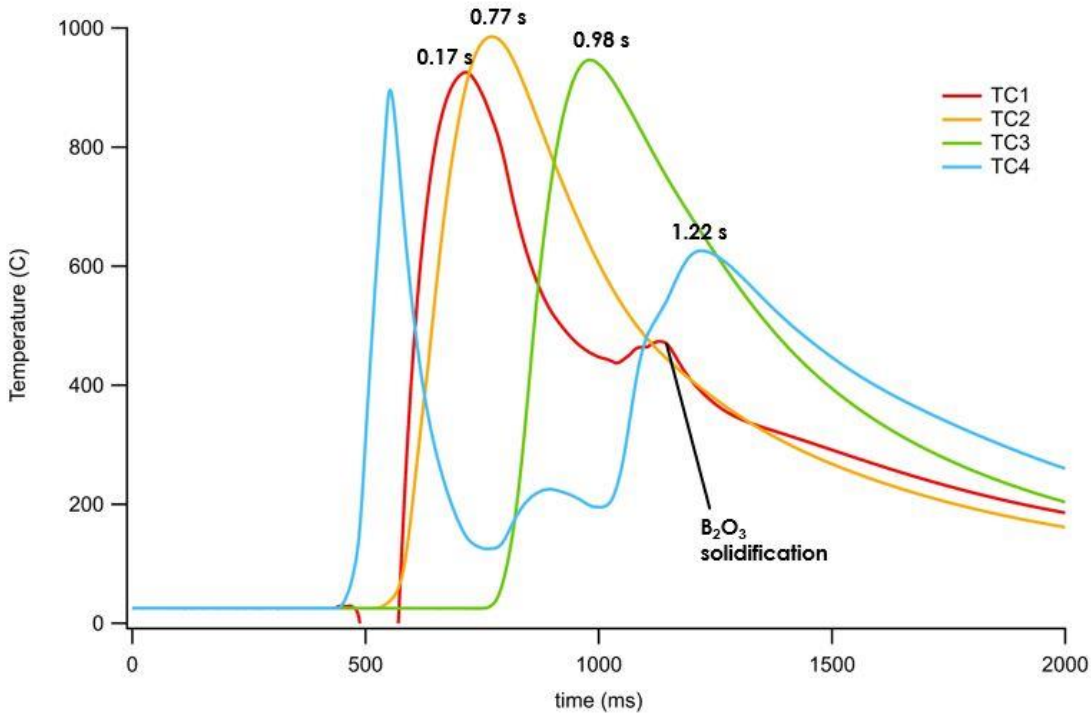

Figure 67: Reaction propagation for the reaction of lithium peroxide and boron using the graphite propagation cell and a tungsten wire. The phase change of boron oxide from liquid to solid is visible in TC1 as that region cools.

4.5.2.5 Rate Calculations

A rate calculation can be made by determining the times the temperature spikes occur since the distances between each thermocouple is known to be 1 cm. The overall rate calculation between the first and last thermocouple is shown in Equation 4.18, where x is the location of a thermocouple and t is the time at which the combustion front passes over a thermocouple.

$$v_{propagation} = \frac{\Delta x_{TC}}{\Delta t_{TC}} = \frac{x_{TC4} - x_{TC1}}{t_{TC4} - t_{TC1}} \tag{4.18}$$

The overall reaction propagation for the experimental run shown in Figure 63 was 1.49 cm/s, which has been our slowest (and therefore best) achieved propagation rate. The rates for many other propagation reactions discussed are listed in Table 26. A singular reaction was performed under nitrogen atmosphere by using N_2 as the purge gas (Figure 64). The utilization of nitrogen resulted in the fastest observed propagation rate of 14.49 cm/s. The highest reaction temperatures achieved in our graphite cell seem to fall within a wide range from 600 – 1400°C. In addition, reaction rates can be inconsistent between thermocouples within the same pyrolant reaction. For example, a peak from TC3 can be closer to TC2 than it is to TC4, indicating the reaction rate increased in the central region of the pyrolant. Inadvertant differences in the packing density of the pyrolant powder within the cell could be a likely cause of these rate changes. A higher packing density in a region of our rectangular chamber could cause a decrease in the propagation rate, since less oxygen permeates the powder and more powder is available for burning.

Table 26: The propagation rates of lithium peroxide and boron pyrolant reactions run with different cell parameters.

#	Cell Type	Wire Type	Atmosphere	Propagation rate (cm/s)	Figure #
1	Graphite	Nichrome	Air (high exposure)	2.21	58a
2	Graphite	Nichrome	Air (tightly sealed)	1.49	63
3	Graphite	Tungsten	Nitrogen	14.49	64
4	Graphite	Tungsten	Argon	4.89	65
5	Graphite	Tungsten	Argon	4.63	66
6	Graphite	Tungsten	Argon	5.92	67

4.6 Conclusion

In this research study, a number of solid exothermic reactions were selected as potential pyrolants with a range of energy densities between 0.8 – 9.0 kWh/kg. These pyrolants were evaluated for use as fuels for long-duration space missions. Ultimately, of 18 pyrolants, the reaction between lithium peroxide (Li_2O_2) and boron (B) was chosen as the initial fuel candidate.

The mechanism of the reaction was determined to proceed through 3 elementary steps: a) the decomposition of lithium peroxide (Li_2O_2) to form lithium oxide (Li_2O), b) the oxidation of boron (B) to form boron oxide (B_2O_3), and c) the reaction of the solid products to form lithium tetraborate ($Li_2B_4O_7$). A slow propagation rate of 1.49 cm/s was achieved by this reaction without the need of any solid additives or external control to further slow burning. This indicates that addition of solid additives with high heat capacity or low melting points could slow the reaction even further and provide a prolonged heat release. Thus, the exothermic reaction between Li_2O_2 and B is a promising candidate for the generation and harvesting of heat to be used as an energy source.

CHAPTER 5: FUTURE WORK

5.1 Hydrodenitrogenation (HDN) of Organic Compounds using *dh*-BN

While performing the catalysis work of hydrogenation using hexagonal boron nitride (*h*-BN) we discovered that boron nitride was able to produce additional interesting products. Our experiments showed that olefins containing nitrile and amine chemical functional groups not only underwent hydrogenation, but also saw breakage of the C-N bond and subsequent removal of the nitrile and amine group as ammonia. This indicates that *dh*-BN may be an effective catalyst for hydrodenitrogenation (HDN) at low temperatures.

A handful of experiments confirmed that the nitrile compounds cinnamonitrile, hydrocinnamonitrile, and acetonitrile could successfully undergo cleavage of their C-N triple bonds to form ammonia gas and their respective characteristic products (Equations 5.1 – 5.3).

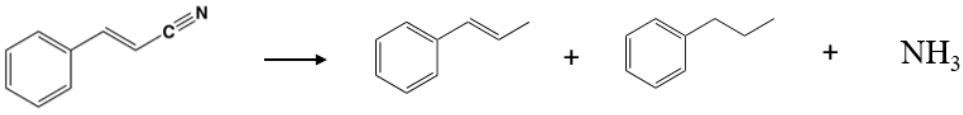

(5.1)

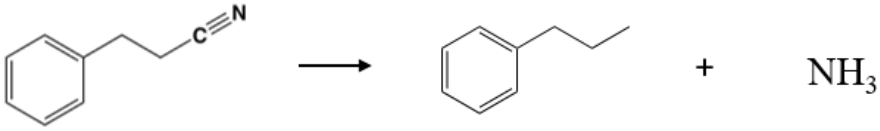

(5.2)

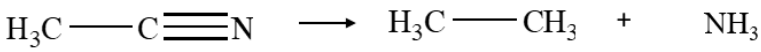

(5.3)

Hexylamine and diisopropylethylamine were also successfully cleaved to form the products shown in Equations 5.4 and 5.5, respectively.

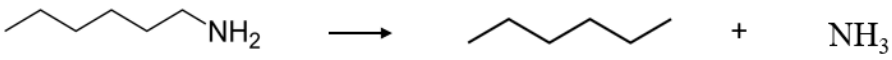

(5.4)

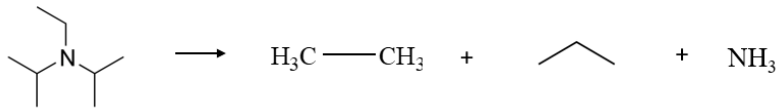

(5.5)

Thus, so far, a short-chain nitrile, two aromatic-containing nitriles, and an olefinic nitrile have undergone successful removal of their nitrogen atoms. This indicates that a C-C double bond is not necessary for the reaction to occur, and the presence of a large ring structure does not hinder the catalytic activity. Further, both a primary and a tertiary amine saw successful nitrogen removal, strongly indicating that a secondary amine (such as methylhexylamine) should be able to be cleaved as well, although this has not been tested. Exploratory experiments with long-chain nitriles and amines (such as decanenitrile or dodecylamine), aromatic amines (such as benzylamine), sterically-hindered compounds (like oleylamine), and structures containing nitrogen *within* 5- or 6-membered rings at different locations (such as piperidine, piperazine, and pyrazole) would illuminate the entire scope through which the boron *dh*-BN can facilitate HDN.

5.2 Photocatalysis using *dh*-BN

Thus far, all discussion of the catalytic activity of *dh*-BN has involved mechanochemical processes. Olefin hydrogenation, CO_2 reduction, and hydrodenitrogenation of nitriles and amines all involved the use of a pebble mill to achieve catalysis at low temperature and pressure. Moreover, the discussion of CO_2 reduction went as far as noting that reactions in a static plug-flow reactor were unsuccessful if mechanical agitation was not involved. However, catalysis *was* found to be largely successful under static conditions if the *dh*-BN is exposed to light.

By constructing a plug-flow reactor from a quartz tube, *dh*-BN can be exposed to light under static or continuous flow of gaseous reagents. Under static conditions, propene exposed to

high-intensity light was found to dehydrogenate to produce benzene and hydrogen. Two such plug flow reactors are shown in Figures 68 and 69 below.

Figure 68: First iteration of a medium-intensity plug-flow photoreactor. The quartz tube contains *dh*-BN and is situatuated in the center of a circular light source.

Studying changes in the packing density of the catalyst in the tube, as well as the intensity of the light and flow of reagents would allow for optimization and potentially control of the products able to be synthesized.

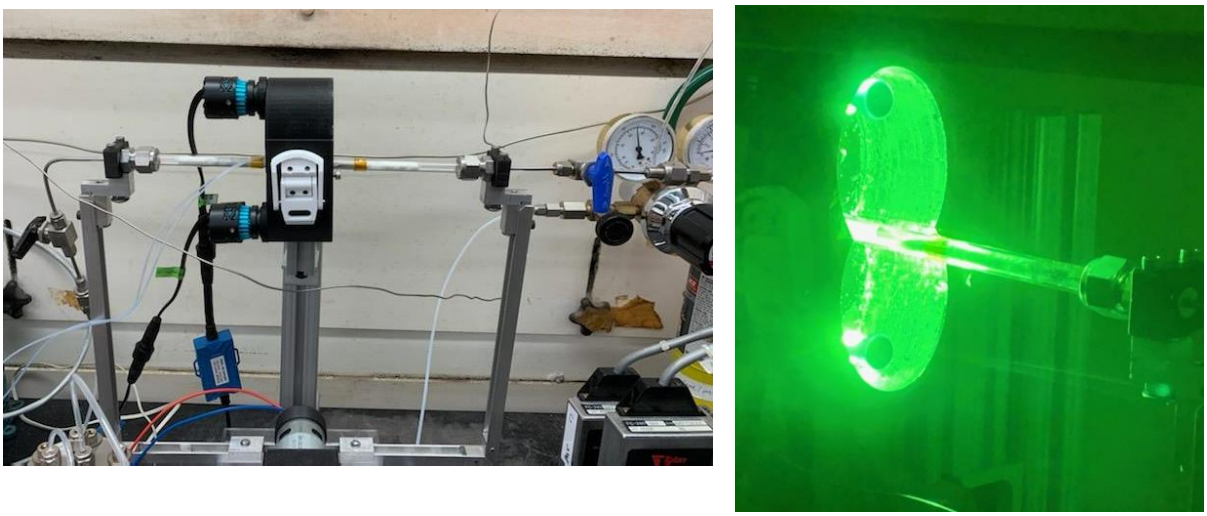

Figure 69: A second iteration of a higher-intensity plug flow photoreactor, with similar setup as in Figure 69, but with a new light source. Figure on the right has a green filter for easier viewing.

5.3 Solid-State Exothermic Reactions for Powering Space Exploration

From the work discussed in Chapter 4, a select number of pyrolants other than lithium peroxide and boron also displayed some potential to be slow propagating. These pyrolants are reactions #2 and #11: boron + magnesium diboride ($B + MgB_2$) and aluminum + molybdenum trioxide ($Al + MoO_3$), and they should be similarly analyzed and assessed for their slowest propagation rate. Once a value can be obtained for each pyrolant's slowest burning rate in powdered form, this rate could be slowed further by pelletizing the powder into various shapes and controlling the volume of empty space in the reaction bed.

The addition of the purge box to the experimental setup allows for testing of a variety of gaseous headspaces other than argon. The presence of atmospheric N_2, CO_2, or He could have different affects on the reaction propagation. Partial vaccum can also be tested. Further, the oxygen levels within the purge box can be monitored and controlled prior to reaction ignition as well as during propagation. The level of oxygen in contact with the pyrolant can cause a hotter burn and faster propagation. However, certain pyrolants (such as lithium peroxide and boron) produce

oxygen in an intermediate step as part of their reaction mechanism. Sensing for a spike in O_2 levels mid-propagation may provide insight into how much of this oxygen proceeds forward in the reaction as opposed to escaping into the surrounding box.

5.4 Mechanochemical Synthesis of MoN for Ammonia Production

Using mechanochemical methods, sodium amide ($NaNH_2$) and molybdenum (V) chloride ($MoCl_5$) were successfully able to yield two phases of molybdenum nitride: δ-MoN and γ-Mo_2N (Equation 5.6). The molybdenum compounds are each a black solid (Figure 70) and the synthesis also produces sodium chloride as a byproduct (Figure 71).

$$20NaNH_2 + 4MoCl_5 \rightarrow 20NaCl + 2Mo_2N + 20H_2 + 9N_2 \quad (5.6)$$

$$5NaNH_2 + MoCl_5 \rightarrow 5NaCl + MoN + 5H_2 + 2N_2 \quad (5.7)$$

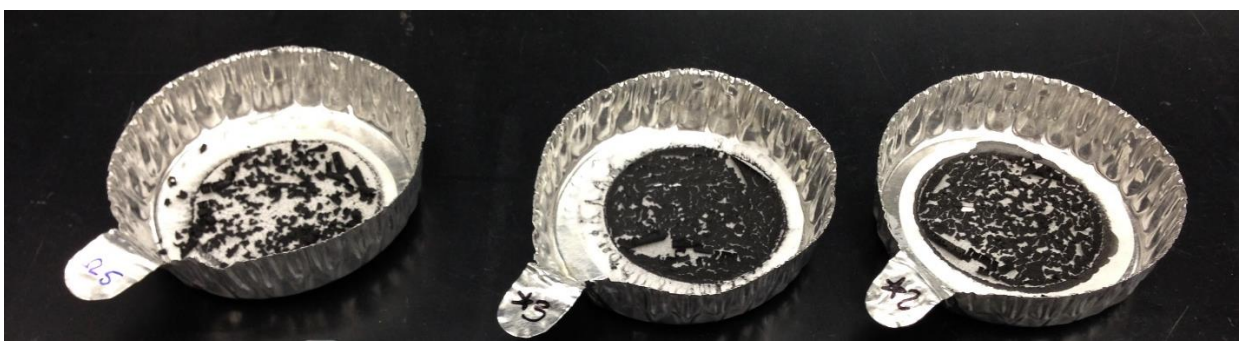

Figure 70: A mixture of δ-MoN and γ-Mo_2N after washing and vaccum filtration.

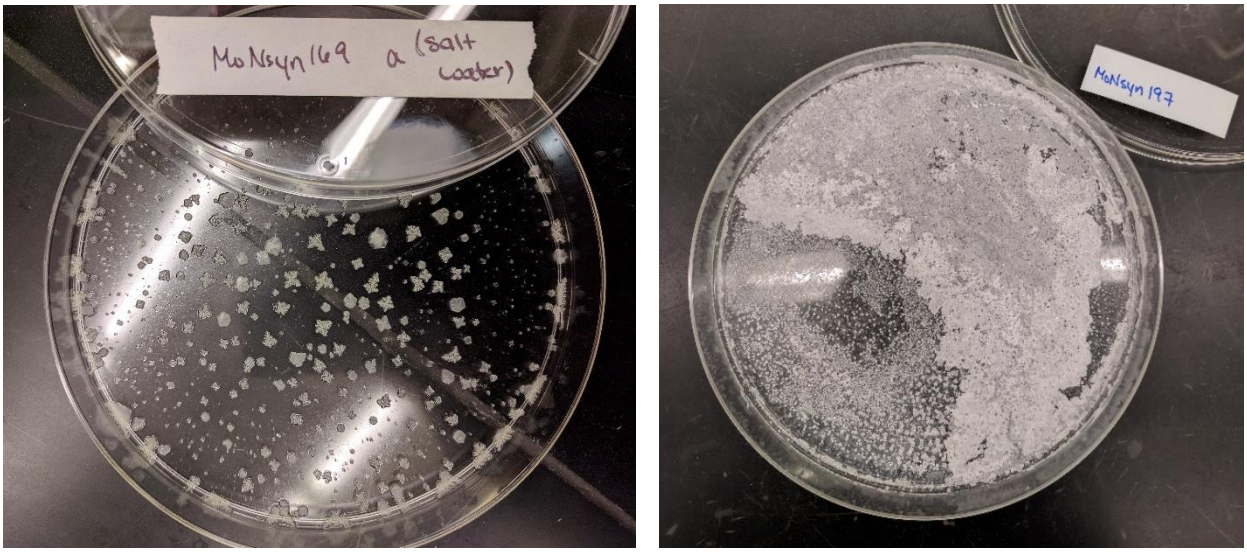

Figure 71: NaCl salt crystals after evaporation of the water supernatant indicates some degree of successful reaction.

Specifically the delta phase of the molybdenum nitride may be an active catalyst for the Haber-Bosch process which produces ammonia industrially. Through x-ray diffraction (XRD), the presence of both compounds are confirmed (Figure 72), although the relative yields of the two phases vary with mill duration and bearing size. However, the gamma phase is consistently the more prevalent. Also troubling was the presence of unreacted material in the vial which resulted in blue molybdenum oxides upon recovery (Figure 73).

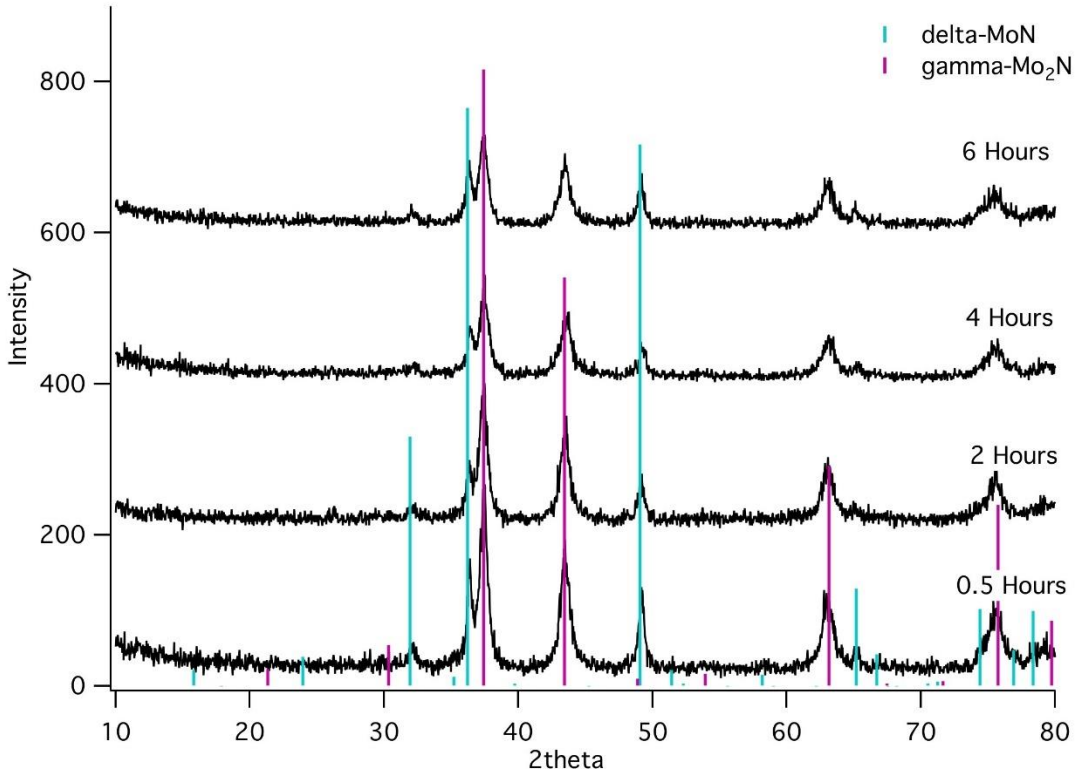

Figure 72: X-ray diffraction of a typical mixture of δ-MoN and γ-Mo_2N at different mill times. With longer duration of milling, peak intensity diminishes at the crystallinity is lost.

Figure 73: If unreacted starting material remained, blue molybdenum oxides resulted from washing with water.

In order to obtain a more concentrated δ-MoN catalyst (undiluted by γ-Mo_2N) the parameters of our synthesis process could be optimized. Initial steps already taken are the simple analysis of the concentrations of each phase with varying milling parameters. However, controlling the heat present during the mechanochemical reaction may prove more effective. Excess heat within the milling vial may be driving the reaction to produce more of the gamma phase, or alternatively, excess heat drives the formation of the delta phase (Figure 74) and there is not enough present.

Heat-withdrawing practices in a ball milling experiement can include the addition of solid chemical additives, such as NaCl or NH_4Cl which would absorb heat without reacting as reagents. In addition, small bearings of a high heat capacity material (steel) can act as a means of removing

heat. If the reaction were to require more heat input to favor the delta phase, our steel reaction vial may be of issue, as it is of a high heat capacity. A vial constructed of a lower heat capacity material may result in less heat withdrawl.

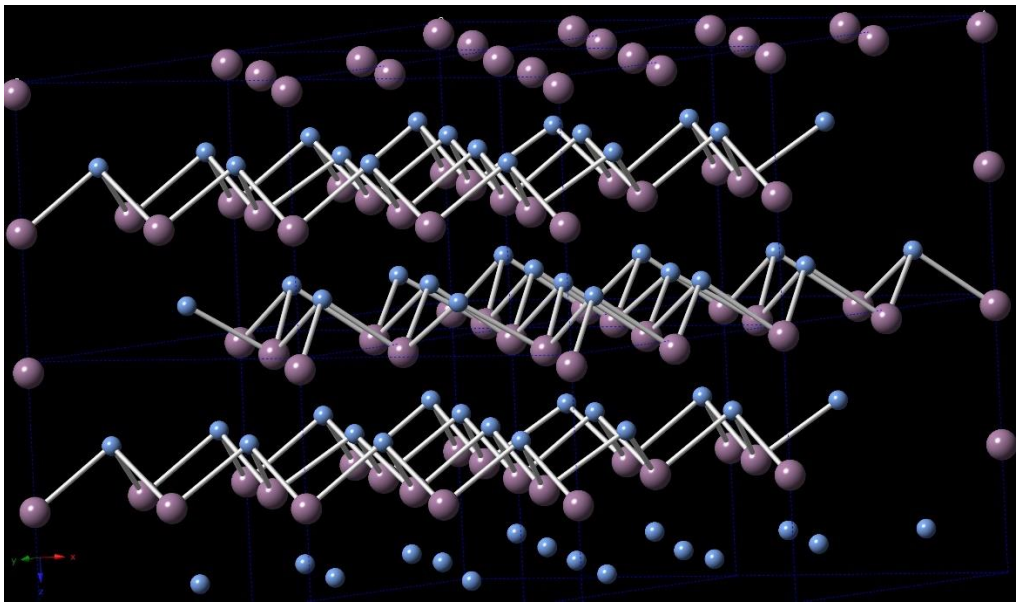

Figure 74: A model of the chemical structure of δ-MoN.

Even a mixture with a small concentration of δ-MoN may be able to successfully catalyze the synthesis of ammonia from the elements in the gas phase. Typically, nitrogen and hydrogen gas are reacted to form ammonia at high temperature as in the reaction in Equation 5.8 and Figure 75. This is traditionally done over heterogeneous iron oxide catalysts, but catalyst alternatives may increase efficiency. It is possible that molybdenum nitride and the implementation of a ball mill could lower the temperature and pressure required by the reaction.

$$N_2 + 3H_2 \rightarrow 2NH_3 \tag{5.8}$$

If we are to have enough δ-MoN to perform catalysis experiments, the catalyst synthesis will need to be scaled up using a pebble, attritor, or planetary mill, which can accommodate

between 10 – 100 times the mass as the mixer mill. This scale up will require its own yield analysis of the two phases, and successful synthesis of a majority delta phase would be a significant accomplishment.

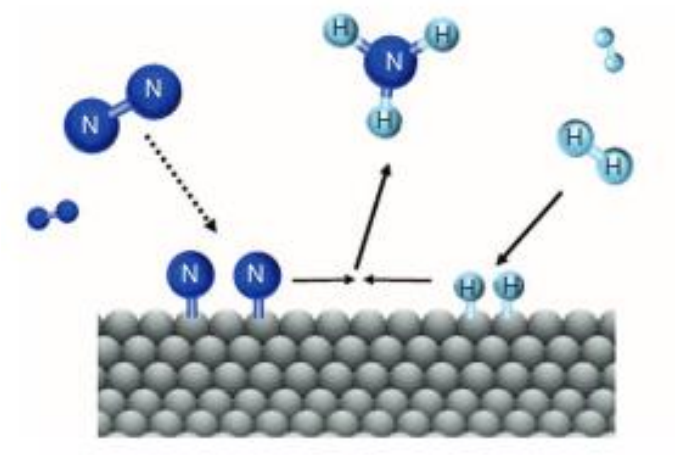

Figure 75: The general process of ammonia synthesis over a catalyst surface should initial begin with the adsorption of diatomic nitrogen and hydrogen before combinging to form ammonia, and subsequent desorption from the surface.

Attempts at producing ammonia using a pebble mill were not initially successful, due to a rather simple but critical issue: we were not able to achieve the mechanical force required in the mill. During mechanical grinding, we noticed that the ball bearings were not making audible collisions or impacts with the material, as they usually do. Selecting different media within the reactor or switching to an attritor mill may be able to allieviate this setback. The mixer and planetary mill vials do not have the innate capability to introduce gas into the reaction headspace. Thus, the attritor mill is the next available option.

APPENDIX A: CURRICULUM VITAE

Katerina L. Chagoya

Education

Ph.D. Mechanical Engineering, *University of Central Florida, Orlando, FL* 2021

Dissertation: Synthesis and Assessment of Sustainable Fuels for Transportation and Space Exploration

Advisors: Dr. Richard Blair, Dr. Jayanta Kapat

M.S. Mechanical Engineering, *University of Central Florida, Orlando, FL* 2021

Thesis: Harvesting Heat from Safer, Energy-Dense, Slow Pyrolant Mixtures for Future Space Missions

Advisors: Dr. Richard Blair, Dr. Jayanta Kapat

B.S. Physics, *University of Central Florida, Orlando, FL* 2016

Minor: Chemistry

Research Experience

Graduate Research Associate Aug 2017 – Present

Blair Research Group, University of Central Florida, Orlando, Florida

Scientist 1 July 2015 – Aug 2017

Ek Laboratories, Longwood, Florida

Undergraduate Research Assistant 2014 – 2016

Blair Research Group, University of Central Florida, Orlando, Florida

Progress Energy Research Assistant 2013 – 2014

Blair Research Group, University of Central Florida, Orlando, Florida

EXCEL Undergraduate Research Assistant 2012 – 2013

Blair Research Group, University of Central Florida, Orlando, Florida

Teaching and Mentoring

Laboratory Research Mentor Aug 2017 – Present

Blair Research Group, University of Central Florida, Orlando, FL

9 Students mentored.

Graduate Teaching Assistant Aug 2020 – Dec 2020

Department of Mechanical Engineering, University of Central Florida, Orlando, FL

EML5060 Mathematical Methods in Mechanical and Aerospace Engineering

EGN3343 Thermodynamics

Graduate Research Mentor Aug 2017 – May 2019

NSF L.E.A.R.N. Program, University of Central Florida, Orlando, FL

3 Students mentored.

Chemistry Intern Supervisor July 2015 – Aug 2017

Ek Laboratories, Inc. Longwood, FL

4 Interns supervised.

Academic Tutor Aug 2014 – Aug 2015

Student Academic Resource Center (SARC) University of Central Florida, Orlando, FL

AST2002 Astronomy

BSC2010C Biology

Awards

L.E.A.R.N. Graduate Mentor Scholarship	2019
FIMS First Place Graduate Poster Presentation Award	2019
L.E.A.R.N. Graduate Mentor Scholarship	2018
SURE Poster Presentation Award	2016
Progress Energy Research Scholarship	2012

Affiliations

American Society of Mechanical Engineers, Member	2018 – present
American Chemical Society, Member	2018 – present
Astronomy Society, Vice President	2015 – 2016
Women in Physics Society, Member	2015 – 2016
American Physical Society, Member	2014 – 2016
Astronomy Society, Member	2014 – 2016
Girls Excelling in Math and Science (GEMS), Member	2011 – 2012

EXCEL 2010 – 2012

Publications

Peer-Reviewed

1. R. Kancherla, K.L. Chagoya, A. Terracciano, R. Blair, S. Vasu, **Modeling of propagation controlled solid fuel-oxidant reactions for the generation of harvestable heat**, AIAA SciTech 2021 Forum, 2021, 10.2514/6.2021-0796.
2. A. Aftab, K.L. Chagoya, A. Felix, R. Blair, N. Orlovskaya, **Catalytic performance of porous Yb_2O_3 sesquioxide**, Advances in Applied Ceramics 120 (2021) 175-186, 10.1080/17436753.2021.1919359.
3. K.L. Chagoya, D.J. Nash, T. Jiang, D. Le, S. Alayoglu, K.B. Idrees, X. Zhang, O.K. Farha, J.K. Harper, T.S. Rahman, R.G. Blair, **Mechanically enhanced catalytic reduction of carbon dioxide over defect hexagonal boron nitride**, Sustainable Chemistry and Engineering (2021), 10.1021/acssuschemeng.0c06172.
4. K.L. Chagoya, A. Felix, F. Torres, N. Ciaffone, T.E. Pitts, A. Curbelo, L. Tetard, J. Kapat, R.G. Blair, **Thermal degradation of biofuels in contact with hot metal surfaces**, Turbo Expo: Power for Land, Sea, and Air, ASME, Phoenix, AZ, 2019, 10.1115/GT2019-91811.
5. D.J. Nash, K.L. Chagoya, A. Felix, F.E. Torres-Davila, T. Jiang, D. Le, L. Tetard, T.S. Rahman, R.G. Blair, **Analysis of the fluorescence of mechanically processed defect-laden hexagonal boron nitride and the role of oxygen in catalyst deactivation**, Advances in Applied Ceramics 118 (2019) 153-158, 10.1080/17436753.2019.1584482.
6. R.G. Blair, K.L. Chagoya, S. Biltek, S. Jackson, A. Sinclair, A. Taraboletti, D.T. Restrepo, **The scalability in the mechanochemical syntheses of edge functionalized graphene materials and biomass-derived chemicals**, Faraday Discuss 170 (2014) 223-233, 10.1039/c4fd00007b.

Not Peer-Reviewed

1. K. Almeida, K.L. Chagoya, A. Felix, T. Jiang, D. Le, T.B. Rawal, P.E. Evans, M. Wurch, K. Yamaguchi, P.A. Dowben, L. Bartels, R.G. Blair, **Towards higher alcohol formation using a single-layer MoS_2 activated Au on silica: Methanol Carbonylation to Acetaldehyde**, ChemRxiv (2020), 10.26434/chemrxiv.8044607.v1.

Patents

1. L. Tetard, F. Torres-Davila, R.G. Blair, K.L. Chagoya, Photochemical transformation using engineered metal-free hexagonal boron nitride. Patent pending, filed July 7, 2021.
2. R.G. Blair, T. Rahman, D. Le, A. Felix, K.L. Chagoya, Catalyst for the Realization of Propylene from Syngas. UCF Patent Disclosure No. 11512. Filed Oct 24, 2019.

Conference Proceedings

1. **Harvesting heat from safer, energy-dense slow pyrolant mixtures for future space missions,** K.L. Chagoya, R.G. Blair, ACS National Meeting and Exposition, 2021.
2. **Optical properties and surface termination of pristine and intercalated GeI_2**, A. Dhingra, K.L. Chagoya, J. Dalton, R.G. Blair, P.A. Dowben, APS March Meeting, 2021.
3. **CO_2 conversion on defect-induced single-layer h-BN**, D. Le, T. Jiang, K. L. Chagoya, D.J. Nash, R.G. Blair, T. Raman, APS March Meeting 2020, Denver, CO, 2020.
4. **Removing nitrogen from biofuels: catalytic cleavage of nitriles and amines using boron nitride,** K.L. Chagoya, R.G. Blair, Florida Inorganic and Materials Symposium, 2019.
5. **Thermal degradation of biofuels in contact with hot metal surfaces**, K.L. Chagoya, A. Felix, F. Torres, N. Ciaffone, T.E. Pitts, A. Curbelo, L. Tetard, J. Kapat, R.G. Blair, Florida Inorganic and Materials Symposium, 2019.
6. **Thermal degradation of biofuels in contact with hot metal surfaces**, K.L. Chagoya, A. Felix, F. Torres, N. Ciaffone, T.E. Pitts, A. Curbelo, L. Tetard, J. Kapat, R.G. Blair, ASME Turbo Expo: Power for Land, Sea, and Air, 2019.
7. **Mechanocatalytic reduction of CO_2 for the realization of formic acid**, K.L. Chagoya, R.G. Blair, ACS National Meeting and Exposition, 2019.
8. **Thermal degradation of biofuels in contact with hot metal surfaces**, K.L. Chagoya, A. Felix, F. Torres, N. Ciaffone, T.E. Pitts, A. Curbelo, L. Tetard, J. Kapat, R.G. Blair, NETL University Turbine Systems Research Review Meeting, 2019.
9. **Study of the effect of ball milling parameters on defect introduction in h-BN for heterogeneous catalytic applications**, F. Torres-Davila, Y. Ding, K. L. Chagoya, A. Felix, D.J. Nash, R.G. Blair, L. Tetard, Bridge Program and National Mentoring Community Conference, Stanford University, California, 2018.
10. **The synthesis of delta phase molybdenum nitride for use as a catalyst in ammonia production via mechanochemical methods**, K.L. Chagoya, D.J. Nash, R.G. Blair, ACS Florida Annual Meeting and Exposition, 2016.
11. **The synthesis of delta phase molybdenum nitride for use as a catalyst in ammonia production via mechanochemical methods**, K.L. Chagoya, D.J. Nash, R.G. Blair, UCF SURE, 2016.
12. **Mechanocatalysis of cellulose for use as feedstock**, K.L. Chagoya, B. Hall, D.T. Restrepo, R.G. Blair, ACS Florida Annual Meeting and Exposition, 2013.
13. **Mechanocatalysis of cellulose for use as feedstock**, K.L. Chagoya, B. Hall, D.T. Restrepo, R.G. Blair, UCF SURE, 2013.

APPENDIX B: COPYRIGHT PERMISSION LETTERS

Copyright permission for the work of Chapter 2 in this dissertation.

The work in Chapter 2 of this dissertation has been previously published by the following authors: K.L. Chagoya, D.J. Nash, T. Jiang, D. Le, S. Alayoglu, K.B. Idrees, X. Zhang, O.K. Farha, J.K. Harper, T.S. Rahman, R.G. Blair with the title "Mechanically enhanced catalytic reduction of carbon dioxide over defect hexagonal boron nitride". It was published by ACS Sustainable Chemistry and Engineering, Volume 9, on February 2, 2021.

CCC | RightsLink®

Home | Help | Live Chat | Sign in | Create Account

ACS Publications
Most Trusted. Most Cited. Most Read.

Mechanically Enhanced Catalytic Reduction of Carbon Dioxide over Defect Hexagonal Boron Nitride

Author: Katerina L. Chagoya, David J. Nash, Tao Jiang, et al
Publication: ACS Sustainable Chemistry & Engineering
Publisher: American Chemical Society
Date: Feb 1, 2021

Copyright © 2021, American Chemical Society

PERMISSION/LICENSE IS GRANTED FOR YOUR ORDER AT NO CHARGE

This type of permission/license, instead of the standard Terms and Conditions, is sent to you because no fee is being charged for your order. Please note the following:

- Permission is granted for your request in both print and electronic formats, and translations.
- If figures and/or tables were requested, they may be adapted or used in part.
- Please print this page for your records and send a copy of it to your publisher/graduate school.
- Appropriate credit for the requested material should be given as follows: "Reprinted (adapted) with permission from {COMPLETE REFERENCE CITATION}. Copyright {YEAR} American Chemical Society." Insert appropriate information in place of the capitalized words.
- One-time permission is granted only for the use specified in your RightsLink request. No additional uses are granted (such as derivative works or other editions). For any uses, please submit a new request.

If credit is given to another source for the material you requested from RightsLink, permission must be obtained from that source.

BACK | CLOSE WINDOW

Copyright permission for the work of Chapter 3 in this dissertation.

Portions of the work in Chapter 3 of this dissertation have been previously published by the following authors: K.L. Chagoya, A. Felix, F. Torres, N. Ciaffone, T.E. Pitts, A. Curbelo, L. Tetard, J. Kapat, R.G. Blair with the title “Thermal degradation of biofuels in contact with hot metal surfaces”. It was published by ASME Turbo Expo: Power for Land, Sea, and Air, Volume 4B, on November 5, 2019.

CCC Marketplace™

This is a License Agreement between Katerina Chagoya ("User") and Copyright Clearance Center, Inc. ("CCC") on behalf of the Rightsholder identified in the order details below. The license consists of the order details, the CCC Terms and Conditions below, and any Rightsholder Terms and Conditions which are included below.

All payments must be made in full to CCC in accordance with the CCC Terms and Conditions below.

Order Date	22-Oct-2021	Type of Use	Republish in a thesis/dissertation
Order License ID	1156334-1		
OCLC Number	894927133	Publisher	ASME
		Portion	Excerpt (up to 400 words)

LICENSED CONTENT

Publication Title	ASME Digital Collection	Country	United States of America
Author/Editor	American Society of Mechanical Engineers	Rightsholder	American Society of Mechanical Engineers ASME
Date	01/01/2017	Publication Type	e-Journal

REQUEST DETAILS

Portion Type	Excerpt (up to 400 words)	Distribution	Worldwide
Number of excerpts	4	Translation	Original language of publication
Format (select all that apply)	Electronic	Copies for the disabled?	No
Who will republish the content?	Author of requested content	Minor editing privileges?	No
Duration of Use	Life of current edition	Incidental promotional use?	No
Lifetime Unit Quantity	Up to 499	Currency	USD
Rights Requested	Main product		

NEW WORK DETAILS

Title	Thermal Degradation of Biofuels in Contact With Hot Metal Surfaces	Institution name	University of Central Florida
Instructor name	Dr. Jayanta Kapat	Expected presentation date	2021-11-02

ADDITIONAL DETAILS

Order reference number	N/A	The requesting person / organization to appear on the license	Katerina Chagoya

REUSE CONTENT DETAILS

Title, description or numeric reference of the portion(s)	Thermal Degradation of Biofuels in Contact With Hot Metal Surfaces. Use of small portions of document such as abstract, portions of introduction, methods, and discussion with new additions.	Title of the article/chapter the portion is from	Thermal Degradation of Biofuels in Contact With Hot Metal Surfaces
		Author of portion(s)	American Society of Mechanical Engineers
		Issue, if republishing an article from a serial	N/A
		Publication date of portion	2017-01-01
Editor of portion(s)	Katerina Chagoya		
Volume of serial or monograph	N/A		
Page or page range of portion	1-6		

CCC Terms and Conditions

1. Description of Service; Defined Terms. This Republication License enables the User to obtain licenses for republication of one or more copyrighted works as described in detail on the relevant Order Confirmation (the "Work(s)"). Copyright Clearance Center, Inc. ("CCC") grants licenses through the Service on behalf of the rightsholder identified on the Order Confirmation (the "Rightsholder"). "Republication", as used herein, generally means the inclusion of a Work, in whole or in part, in a new work or works, also as described on the Order Confirmation. "User", as used herein, means the person or entity making such republication.

2. The terms set forth in the relevant Order Confirmation, and any terms set by the Rightsholder with respect to a particular Work, govern the terms of use of Works in connection with the Service. By using the Service, the person transacting for a republication license on behalf of the User represents and warrants that he/she/it (a) has been duly authorized by the User to accept, and hereby does accept, all such terms and conditions on behalf of User, and (b) shall inform User of all such terms and conditions. In the event such person is a "freelancer" or other third party independent of User and CCC, such party shall be deemed jointly a "User" for purposes of these terms and conditions. In any event, User shall be deemed to have accepted and agreed to all such terms and conditions if User republishes the Work in any fashion.

3. Scope of License; Limitations and Obligations.

   3.1. All Works and all rights therein, including copyright rights, remain the sole and exclusive property of the Rightsholder. The license created by the exchange of an Order Confirmation (and/or any invoice) and payment by User of the full amount set forth on that document includes only those rights expressly set forth in the Order Confirmation and in these terms and conditions, and conveys no other rights in the Work(s) to User. All rights not expressly granted are hereby reserved.

   3.2. General Payment Terms: You may pay by credit card or through an account with us payable at the end of the month. If you and we agree that you may establish a standing account with CCC, then the following terms apply: Remit Payment to: Copyright Clearance Center, 29118 Network Place, Chicago, IL 60673-1291. Payments Due: Invoices are payable upon their delivery to you (or upon our notice to you that they are available to you for downloading). After 30 days, outstanding amounts will be subject to a service charge of 1-1/2% per month or, if less, the maximum rate allowed by applicable law. Unless otherwise specifically set forth in the Order Confirmation or in a separate written agreement signed by CCC, invoices are due and payable on "net 30" terms. While User may exercise the rights licensed immediately upon issuance of the Order Confirmation, the license is automatically revoked and is null and void, as if it had never been issued, if complete payment for the license is not received on a timely basis either from User directly or through a payment agent, such as a credit card company.

   3.3. Unless otherwise provided in the Order Confirmation, any grant of rights to User (i) is "one-time" (including the editions and product family specified in the license), (ii) is non-exclusive and non-transferable and (iii)

is subject to any and all limitations and restrictions (such as, but not limited to, limitations on duration of use or circulation) included in the Order Confirmation or invoice and/or in these terms and conditions. Upon completion of the licensed use, User shall either secure a new permission for further use of the Work(s) or immediately cease any new use of the Work(s) and shall render inaccessible (such as by deleting or by removing or severing links or other locators) any further copies of the Work (except for copies printed on paper in accordance with this license and still in User's stock at the end of such period).

3.4. In the event that the material for which a republication license is sought includes third party materials (such as photographs, illustrations, graphs, inserts and similar materials) which are identified in such material as having been used by permission, User is responsible for identifying, and seeking separate licenses (under this Service or otherwise) for, any of such third party materials; without a separate license, such third party materials may not be used.

3.5. Use of proper copyright notice for a Work is required as a condition of any license granted under the Service. Unless otherwise provided in the Order Confirmation, a proper copyright notice will read substantially as follows: "Republished with permission of [Rightsholder's name], from [Work's title, author, volume, edition number and year of copyright]; permission conveyed through Copyright Clearance Center, Inc. " Such notice must be provided in a reasonably legible font size and must be placed either immediately adjacent to the Work as used (for example, as part of a by-line or footnote but not as a separate electronic link) or in the place where substantially all other credits or notices for the new work containing the republished Work are located. Failure to include the required notice results in loss to the Rightsholder and CCC, and the User shall be liable to pay liquidated damages for each such failure equal to twice the use fee specified in the Order Confirmation, in addition to the use fee itself and any other fees and charges specified.

3.6. User may only make alterations to the Work if and as expressly set forth in the Order Confirmation. No Work may be used in any way that is defamatory, violates the rights of third parties (including such third parties' rights of copyright, privacy, publicity, or other tangible or intangible property), or is otherwise illegal, sexually explicit or obscene. In addition, User may not conjoin a Work with any other material that may result in damage to the reputation of the Rightsholder. User agrees to inform CCC if it becomes aware of any infringement of any rights in a Work and to cooperate with any reasonable request of CCC or the Rightsholder in connection therewith.

4. Indemnity. User hereby indemnifies and agrees to defend the Rightsholder and CCC, and their respective employees and directors, against all claims, liability, damages, costs and expenses, including legal fees and expenses, arising out of any use of a Work beyond the scope of the rights granted herein, or any use of a Work which has been altered in any unauthorized way by User, including claims of defamation or infringement of rights of copyright, publicity, privacy or other tangible or intangible property.

5. Limitation of Liability. UNDER NO CIRCUMSTANCES WILL CCC OR THE RIGHTSHOLDER BE LIABLE FOR ANY DIRECT, INDIRECT, CONSEQUENTIAL OR INCIDENTAL DAMAGES (INCLUDING WITHOUT LIMITATION DAMAGES FOR LOSS OF BUSINESS PROFITS OR INFORMATION, OR FOR BUSINESS INTERRUPTION) ARISING OUT OF THE USE OR INABILITY TO USE A WORK, EVEN IF ONE OF THEM HAS BEEN ADVISED OF THE POSSIBILITY OF SUCH DAMAGES. In any event, the total liability of the Rightsholder and CCC (including their respective employees and directors) shall not exceed the total amount actually paid by User for this license. User assumes full liability for the actions and omissions of its principals, employees, agents, affiliates, successors and assigns.

6. Limited Warranties. THE WORK(S) AND RIGHT(S) ARE PROVIDED "AS IS". CCC HAS THE RIGHT TO GRANT TO USER THE RIGHTS GRANTED IN THE ORDER CONFIRMATION DOCUMENT. CCC AND THE RIGHTSHOLDER DISCLAIM ALL OTHER WARRANTIES RELATING TO THE WORK(S) AND RIGHT(S), EITHER EXPRESS OR IMPLIED, INCLUDING WITHOUT LIMITATION IMPLIED WARRANTIES OF MERCHANTABILITY OR FITNESS FOR A PARTICULAR PURPOSE. ADDITIONAL RIGHTS MAY BE REQUIRED TO USE ILLUSTRATIONS, GRAPHS, PHOTOGRAPHS, ABSTRACTS, INSERTS OR OTHER PORTIONS OF THE WORK (AS OPPOSED TO THE ENTIRE WORK) IN A MANNER CONTEMPLATED BY USER; USER UNDERSTANDS AND AGREES THAT NEITHER CCC NOR THE RIGHTSHOLDER MAY HAVE SUCH ADDITIONAL RIGHTS TO GRANT.

7. Effect of Breach. Any failure by User to pay any amount when due, or any use by User of a Work beyond the scope of the license set forth in the Order Confirmation and/or these terms and conditions, shall be a material breach of the license created by the Order Confirmation and these terms and conditions. Any breach not cured within 30 days of written notice thereof shall result in immediate termination of such license without further notice. Any unauthorized (but licensable) use of a Work that is terminated immediately upon notice thereof may be liquidated by payment of the Rightsholder's ordinary license price therefor; any unauthorized (and unlicensable) use that is not terminated immediately for any reason (including, for example, because materials containing the Work cannot reasonably be recalled) will be subject to all remedies available at law or in equity, but in no event to a payment of less than three times the Rightsholder's ordinary license price for the most closely analogous licensable use plus Rightsholder's and/or CCC's costs and expenses incurred in collecting such payment.

8. Miscellaneous.

   8.1. User acknowledges that CCC may, from time to time, make changes or additions to the Service or to these terms and conditions, and CCC reserves the right to send notice to the User by electronic mail or otherwise for the purposes of notifying User of such changes or additions; provided that any such changes or additions shall not apply to permissions already secured and paid for.

   8.2. Use of User-related information collected through the Service is governed by CCC's privacy policy, available online here:**https://marketplace.copyright.com/rs-ui-web/mp/privacy-policy**

   8.3. The licensing transaction described in the Order Confirmation is personal to User. Therefore, User may not assign or transfer to any other person (whether a natural person or an organization of any kind) the license created by the Order Confirmation and these terms and conditions or any rights granted hereunder; provided, however, that User may assign such license in its entirety on written notice to CCC in the event of a transfer of all or substantially all of User's rights in the new material which includes the Work(s) licensed under this Service.

   8.4. No amendment or waiver of any terms is binding unless set forth in writing and signed by the parties. The Rightsholder and CCC hereby object to any terms contained in any writing prepared by the User or its principals, employees, agents or affiliates and purporting to govern or otherwise relate to the licensing transaction described in the Order Confirmation, which terms are in any way inconsistent with any terms set forth in the Order Confirmation and/or in these terms and conditions or CCC's standard operating procedures, whether such writing is prepared prior to, simultaneously with or subsequent to the Order Confirmation, and whether such writing appears on a copy of the Order Confirmation or in a separate instrument.

   8.5. The licensing transaction described in the Order Confirmation document shall be governed by and construed under the law of the State of New York, USA, without regard to the principles thereof of conflicts of law. Any case, controversy, suit, action, or proceeding arising out of, in connection with, or related to such licensing transaction shall be brought, at CCC's sole discretion, in any federal or state court located in the County of New York, State of New York, USA, or in any federal or state court whose geographical jurisdiction covers the location of the Rightsholder set forth in the Order Confirmation. The parties expressly submit to the personal jurisdiction and venue of each such federal or state court.If you have any comments or questions about the Service or Copyright Clearance Center, please contact us at 978-750-8400 or send an e-mail to **support@copyright.com**.

v 1.1

Copyright permission letter for figures created by Union of Concerned Scientists

RE: [Netlify] [Reuse permission request from the website]

Cynthia DeRocco <CDeRocco@ucsusa.org>
Wed 11/17/2021 10:58 AM
To: Katerina Chagoya <katerina.chagoya.5433@knights.ucf.edu>
Cc: Cana Tagawa <CTagawa@ucsusa.org>

Hi Katerina,

So sorry for the delayed response. You are more than welcome to use this material in your dissertation. Please let me know if you need anything else and good luck on your work!

Cynthia DeRocco
Production and Design Manager
pronouns: she/her/hers
Union of Concerned Scientists
2 Brattle Square | Cambridge, MA 02138-3780 | P: (617)-301-8066

The Union of Concerned Scientists puts rigorous, independent science to work to solve our planet's most pressing problems. Joining with people across the country, we combine technical analysis and effective advocacy to create innovative, practical solutions for a healthy, safe, and sustainable future.
https://nam02.safelinks.protection.outlook.com/?url=http%3A%2F%2Fwww.ucsusa.org%2F&data=04%7C01%7Ckaterina.chagoya.5433%40knights.ucf.edu%7C9df4bfcdf0b743f93a5f08d9a9e31c88%7C5b16e18278b3412c919668342689eeb7%7C0%7C1%7C637727615178858074%7CUnknown%7CTWFpbGZsb3d8eyJWIjoiMC4wLjAwMDAiLCJQIjoiV2luMzIiLCJBTiI6Ik1haWwiLCJXVCI6Mn0%3D%7C3000&sdata=DYcMPy1XemzoRK9UvMIsMm8QQ01W86pOokswB1nGk5M%3D&reserved=0 | Join our action network or expert network | Support our work.
Join the conversation on our blogs: The Equation and All Things Nuclear; or follow UCS on Facebook, Twitter, and Instagram.

Copyright permission letter for a figure in Chapter 4.

No changes were made to the figure, and the license is provided here (below) as well as at the following link: https://creativecommons.org/licenses/by/3.0/legalcode.

Attribution 3.0 Unported (CC BY 3.0)

This is a human-readable summary of (and not a substitute for) the license. Disclaimer.

You are free to:

Share — copy and redistribute the material in any medium or format

Adapt — remix, transform, and build upon the material for any purpose, even commercially.

The licensor cannot revoke these freedoms as long as you follow the license terms.

Under the following terms:

Attribution — You must give appropriate credit, provide a link to the license, and indicate if changes were made. You may do so in any reasonable manner, but not in any way that suggests the licensor endorses you or your use.

No additional restrictions — You may not apply legal terms or technological measures that legally restrict others from doing anything the license permits.

Notices:

You do not have to comply with the license for elements of the material in the public domain or where your use is permitted by an applicable exception or limitation.

No warranties are given. The license may not give you all of the permissions necessary for your intended use. For example, other rights such as publicity, privacy, or moral rights may limit how you use the material.

Creative Commons Legal Code

Attribution 3.0 Unported

CREATIVE COMMONS CORPORATION IS NOT A LAW FIRM AND DOES NOT PROVIDE LEGAL SERVICES. DISTRIBUTION OF THIS LICENSE DOES NOT CREATE AN ATTORNEY-CLIENT RELATIONSHIP. CREATIVE COMMONS PROVIDES THIS INFORMATION ON AN "AS-IS" BASIS. CREATIVE COMMONS MAKES NO WARRANTIES REGARDING THE INFORMATION PROVIDED, AND DISCLAIMS LIABILITY FOR DAMAGES RESULTING FROM ITS USE.

License

THE WORK (AS DEFINED BELOW) IS PROVIDED UNDER THE TERMS OF THIS CREATIVE COMMONS PUBLIC LICENSE ("CCPL" OR "LICENSE"). THE WORK IS PROTECTED BY COPYRIGHT AND/OR OTHER APPLICABLE LAW. ANY USE OF THE WORK OTHER THAN AS AUTHORIZED UNDER THIS LICENSE OR COPYRIGHT LAW IS PROHIBITED.

BY EXERCISING ANY RIGHTS TO THE WORK PROVIDED HERE, YOU ACCEPT AND AGREE TO BE BOUND BY THE TERMS OF THIS LICENSE. TO THE EXTENT THIS LICENSE MAY BE CONSIDERED TO BE A CONTRACT, THE LICENSOR GRANTS YOU THE RIGHTS CONTAINED HERE IN CONSIDERATION OF YOUR ACCEPTANCE OF SUCH TERMS AND CONDITIONS.

1. Definitions

a. **"Adaptation"** means a work based upon the Work, or upon the Work and other pre-existing works, such as a translation, adaptation, derivative work, arrangement of music or other alterations of a literary or artistic work, or phonogram or performance and includes cinematographic adaptations or any other form in which the Work may be recast, transformed, or adapted including in any form recognizably derived from the original, except that a work that constitutes a Collection will not be considered an Adaptation for the purpose of this License. For the avoidance of doubt, where the Work is a musical work, performance or phonogram, the synchronization of the Work in timed-relation with a moving image ("synching") will be considered an Adaptation for the purpose of this License.

b. **"Collection"** means a collection of literary or artistic works, such as encyclopedias and anthologies, or performances, phonograms or broadcasts, or other works or subject matter other than works listed in Section 1(f) below, which, by reason of the selection and arrangement of their contents, constitute intellectual creations, in which the Work is included in its entirety in unmodified form along with one or more other contributions, each constituting separate and independent works in themselves, which together are assembled into a collective whole. A work that constitutes a Collection will not be considered an Adaptation (as defined above) for the purposes of this License.

c. **"Distribute"** means to make available to the public the original and copies of the Work or Adaptation, as appropriate, through sale or other transfer of ownership.

d. **"Licensor"** means the individual, individuals, entity or entities that offer(s) the Work under the terms of this License.

e. **"Original Author"** means, in the case of a literary or artistic work, the individual, individuals, entity or entities who created the Work or if no individual or entity can be identified, the publisher; and in addition (i) in the case of a performance the actors, singers, musicians, dancers, and other persons who act, sing, deliver, declaim, play in, interpret or otherwise perform literary or artistic works or expressions of folklore; (ii) in the case of a phonogram the producer being the person or legal entity who first fixes the sounds of a performance or other sounds; and, (iii) in the case of broadcasts, the organization that transmits the broadcast.

f. **"Work"** means the literary and/or artistic work offered under the terms of this License including without limitation any production in the literary, scientific and artistic domain, whatever may be the

mode or form of its expression including digital form, such as a book, pamphlet and other writing; a lecture, address, sermon or other work of the same nature; a dramatic or dramatico-musical work; a choreographic work or entertainment in dumb show; a musical composition with or without words; a cinematographic work to which are assimilated works expressed by a process analogous to cinematography; a work of drawing, painting, architecture, sculpture, engraving or lithography; a photographic work to which are assimilated works expressed by a process analogous to photography; a work of applied art; an illustration, map, plan, sketch or three-dimensional work relative to geography, topography, architecture or science; a performance; a broadcast; a phonogram; a compilation of data to the extent it is protected as a copyrightable work; or a work performed by a variety or circus performer to the extent it is not otherwise considered a literary or artistic work.

g. **"You"** means an individual or entity exercising rights under this License who has not previously violated the terms of this License with respect to the Work, or who has received express permission from the Licensor to exercise rights under this License despite a previous violation.
h. **"Publicly Perform"** means to perform public recitations of the Work and to communicate to the public those public recitations, by any means or process, including by wire or wireless means or public digital performances; to make available to the public Works in such a way that members of the public may access these Works from a place and at a place individually chosen by them; to perform the Work to the public by any means or process and the communication to the public of the performances of the Work, including by public digital performance; to broadcast and rebroadcast the Work by any means including signs, sounds or images.
i. **"Reproduce"** means to make copies of the Work by any means including without limitation by sound or visual recordings and the right of fixation and reproducing fixations of the Work, including storage of a protected performance or phonogram in digital form or other electronic medium.

2. Fair Dealing Rights. Nothing in this License is intended to reduce, limit, or restrict any uses free from copyright or rights arising from limitations or exceptions that are provided for in connection with the copyright protection under copyright law or other applicable laws.

3. License Grant. Subject to the terms and conditions of this License, Licensor hereby grants You a worldwide, royalty-free, non-exclusive, perpetual (for the duration of the applicable copyright) license to exercise the rights in the Work as stated below:

a. to Reproduce the Work, to incorporate the Work into one or more Collections, and to Reproduce the Work as incorporated in the Collections;
b. to create and Reproduce Adaptations provided that any such Adaptation, including any translation in any medium, takes reasonable steps to clearly label, demarcate or otherwise identify that changes were made to the original Work. For example, a translation could be marked "The original work was translated from English to Spanish," or a modification could indicate "The original work has been modified.";
c. to Distribute and Publicly Perform the Work including as incorporated in Collections; and,
d. to Distribute and Publicly Perform Adaptations.

e. For the avoidance of doubt:

    i. **Non-waivable Compulsory License Schemes**. In those jurisdictions in which the right to collect royalties through any statutory or compulsory licensing scheme cannot be waived, the Licensor reserves the exclusive right to collect such royalties for any exercise by You of the rights granted under this License;
    ii. **Waivable Compulsory License Schemes**. In those jurisdictions in which the right to collect royalties through any statutory or compulsory licensing scheme can be waived, the Licensor waives the exclusive right to collect such royalties for any exercise by You of the rights granted under this License; and,
    iii. **Voluntary License Schemes**. The Licensor waives the right to collect royalties, whether individually or, in the event that the Licensor is a member of a collecting society that administers voluntary licensing schemes, via that society, from any exercise by You of the rights granted under this License.

The above rights may be exercised in all media and formats whether now known or hereafter devised. The above rights include the right to make such modifications as are technically necessary to exercise the rights in other media and formats. Subject to Section 8(f), all rights not expressly granted by Licensor are hereby reserved.

4. Restrictions. The license granted in Section 3 above is expressly made subject to and limited by the following restrictions:

a. You may Distribute or Publicly Perform the Work only under the terms of this License. You must include a copy of, or the Uniform Resource Identifier (URI) for, this License with every copy of the Work You Distribute or Publicly Perform. You may not offer or impose any terms on the Work that restrict the terms of this License or the ability of the recipient of the Work to exercise the rights granted to that recipient under the terms of the License. You may not sublicense the Work. You must keep intact all notices that refer to this License and to the disclaimer of warranties with every copy of the Work You Distribute or Publicly Perform. When You Distribute or Publicly Perform the Work, You may not impose any effective technological measures on the Work that restrict the ability of a recipient of the Work from You to exercise the rights granted to that recipient under the terms of the License. This Section 4(a) applies to the Work as incorporated in a Collection, but this does not require the Collection apart from the Work itself to be made subject to the terms of this License. If You create a Collection, upon notice from any Licensor You must, to the extent practicable, remove from the Collection any credit as required by Section 4(b), as requested. If You create an Adaptation, upon notice from any Licensor You must, to the extent practicable, remove from the Adaptation any credit as required by Section 4(b), as requested.
b. If You Distribute, or Publicly Perform the Work or any Adaptations or Collections, You must, unless a request has been made pursuant to Section 4(a), keep intact all copyright notices for the Work and provide, reasonable to the medium or means You are utilizing: (i) the name of the Original Author (or pseudonym, if applicable) if supplied, and/or if the Original Author and/or Licensor designate another party or parties (e.g., a sponsor institute, publishing entity, journal) for attribution ("Attribution Parties") in Licensor's copyright notice, terms of service or by other reasonable means, the name of such party or parties; (ii) the title of the Work if supplied; (iii) to the extent reasonably practicable, the URI, if any, that Licensor specifies to be associated with the Work, unless such URI does not refer to the copyright notice or licensing information for the Work; and (iv) , consistent with Section 3(b), in the case of an Adaptation, a credit identifying the use of the Work in the Adaptation (e.g., "French translation of the Work by Original Author," or "Screenplay based on original Work by Original Author"). The credit required by this Section 4 (b) may be implemented in any reasonable manner; provided, however, that in the case of a Adaptation or Collection, at a minimum such credit will appear, if a credit for all contributing authors of the Adaptation or Collection appears, then as part of these credits and in a manner at least as prominent as the credits for the other contributing authors. For the avoidance of doubt, You may only use the credit required by this Section for the purpose of attribution in the manner set out above and, by exercising Your rights under this License, You may not implicitly or explicitly assert or imply any connection with, sponsorship or endorsement by the Original Author, Licensor and/or Attribution Parties, as appropriate, of You or Your use of the Work, without the separate, express prior written permission of the Original Author, Licensor and/or Attribution Parties.
c. Except as otherwise agreed in writing by the Licensor or as may be otherwise permitted by applicable law, if You Reproduce, Distribute or Publicly Perform the Work either by itself or as part of any Adaptations or Collections, You must not distort, mutilate, modify or take other derogatory action in relation to the Work which would be prejudicial to the Original Author's honor or reputation. Licensor agrees that in those jurisdictions (e.g. Japan), in which any exercise of the right granted in Section 3(b) of this License (the right to make Adaptations) would be deemed to be a distortion, mutilation, modification or other derogatory action prejudicial to the Original Author's honor and reputation, the Licensor will waive or not assert, as appropriate, this Section, to the fullest extent permitted by the applicable national law, to enable You to reasonably exercise Your right under Section 3(b) of this License (right to make Adaptations) but not otherwise.

5. Representations, Warranties and Disclaimer

UNLESS OTHERWISE MUTUALLY AGREED TO BY THE PARTIES IN WRITING, LICENSOR OFFERS THE WORK AS-IS AND MAKES NO REPRESENTATIONS OR WARRANTIES OF ANY KIND CONCERNING THE WORK, EXPRESS, IMPLIED, STATUTORY OR OTHERWISE, INCLUDING, WITHOUT LIMITATION, WARRANTIES OF TITLE, MERCHANTIBILITY, FITNESS FOR A PARTICULAR PURPOSE, NONINFRINGEMENT, OR THE ABSENCE OF LATENT OR OTHER DEFECTS, ACCURACY, OR THE PRESENCE OF ABSENCE OF ERRORS, WHETHER OR NOT DISCOVERABLE. SOME JURISDICTIONS DO NOT ALLOW THE EXCLUSION OF IMPLIED WARRANTIES, SO SUCH EXCLUSION MAY NOT APPLY TO YOU.

6. Limitation on Liability. EXCEPT TO THE EXTENT REQUIRED BY APPLICABLE LAW, IN NO EVENT WILL LICENSOR BE LIABLE TO YOU ON ANY LEGAL THEORY FOR ANY SPECIAL, INCIDENTAL, CONSEQUENTIAL, PUNITIVE OR EXEMPLARY DAMAGES ARISING OUT OF THIS LICENSE OR THE USE OF THE WORK, EVEN IF LICENSOR HAS BEEN ADVISED OF THE POSSIBILITY OF SUCH DAMAGES.

7. Termination

a. This License and the rights granted hereunder will terminate automatically upon any breach by You of the terms of this License. Individuals or entities who have received Adaptations or Collections from You under this License, however, will not have their licenses terminated provided such individuals or entities remain in full compliance with those licenses. Sections 1, 2, 5, 6, 7, and 8 will survive any termination of this License.
b. Subject to the above terms and conditions, the license granted here is perpetual (for the duration of the applicable copyright in the Work). Notwithstanding the above, Licensor reserves the right to release the Work under different license terms or to stop distributing the Work at any time; provided, however that any such election will not serve to withdraw this License (or any other license that has been, or is required to be, granted under the terms of this License), and this License will continue in full force and effect unless terminated as stated above.

8. Miscellaneous

a. Each time You Distribute or Publicly Perform the Work or a Collection, the Licensor offers to the recipient a license to the Work on the same terms and conditions as the license granted to You under this License.
b. Each time You Distribute or Publicly Perform an Adaptation, Licensor offers to the recipient a license to the original Work on the same terms and conditions as the license granted to You under this License.
c. If any provision of this License is invalid or unenforceable under applicable law, it shall not affect the validity or enforceability of the remainder of the terms of this License, and without further action by the parties to this agreement, such provision shall be reformed to the minimum extent necessary to make such provision valid and enforceable.
d. No term or provision of this License shall be deemed waived and no breach consented to unless such waiver or consent shall be in writing and signed by the party to be charged with such waiver or consent.
e. This License constitutes the entire agreement between the parties with respect to the Work licensed here. There are no understandings, agreements or representations with respect to the Work not specified here. Licensor shall not be bound by any additional provisions that may appear in any communication from You. This License may not be modified without the mutual written agreement of the Licensor and You.
f. The rights granted under, and the subject matter referenced, in this License were drafted utilizing the terminology of the Berne Convention for the Protection of Literary and Artistic Works (as amended on September 28, 1979), the Rome Convention of 1961, the WIPO Copyright Treaty of 1996, the WIPO Performances and Phonograms Treaty of 1996 and the Universal Copyright Convention (as revised on July 24, 1971). These rights and subject matter take effect in the relevant jurisdiction in which the License terms are sought to be enforced according to the corresponding provisions of the implementation of those treaty provisions in the applicable national law. If the standard suite of rights granted under applicable copyright law includes additional rights not granted under this License, such additional rights are deemed to be included in the License; this License is not intended to restrict the license of any rights under applicable law.

Creative Commons Notice

Creative Commons is not a party to this License, and makes no warranty whatsoever in connection with the Work. Creative Commons will not be liable to You or any party on any legal theory for any damages whatsoever, including without limitation any general, special, incidental or consequential damages arising in connection to this license. Notwithstanding the foregoing two (2) sentences, if Creative Commons has expressly identified itself as the Licensor hereunder, it shall have all rights and obligations of Licensor.

Except for the limited purpose of indicating to the public that the Work is licensed under the CCPL, Creative Commons does not authorize the use by either party of the trademark "Creative Commons" or any related trademark or logo of Creative Commons without the prior written consent of Creative Commons. Any permitted use will be in compliance with Creative Commons' then-current trademark usage guidelines, as may be published on its website or otherwise made available upon request from time to time. For the avoidance of doubt, this trademark restriction does not form part of this License.

Creative Commons may be contacted at https://creativecommons.org/.

LIST OF REFERENCES

[1] Monastersky, R., 2013, "Global carbon dioxide levels near worrisome milestone," Nature News, 497(7447), p. 13.

[2] 2014, "Observations: Atmosphere and Surface," Climate Change 2013 – The Physical Science Basis: Working Group I Contribution to the Fifth Assessment Report of the Intergovernmental Panel on Climate Change, C. Intergovernmental Panel on Climate, ed., Cambridge University Press, Cambridge, pp. 159-254.

[3] Doney, S. C., Busch, D. S., Cooley, S. R., and Kroeker, K. J., 2020, "The Impacts of Ocean Acidification on Marine Ecosystems and Reliant Human Communities," Annual Review of Environment and Resources, 45(1), pp. 83-112.

[4] Savo, V., Morton, C., and Lepofsky, D., 2017, "Impacts of climate change for coastal fishers and implications for fisheries," Fish and Fisheries, 18(5), pp. 877-889.

[5] Demeneix, B. A., 2020, "How fossil fuel-derived pesticides and plastics harm health, biodiversity, and the climate," The Lancet Diabetes & Endocrinology, 8(6), pp. 462-464.

[6] Marsooli, R., Lin, N., Emanuel, K., and Feng, K., 2019, "Climate change exacerbates hurricane flood hazards along US Atlantic and Gulf Coasts in spatially varying patterns," Nature Communications, 10(1), p. 3785.

[7] Karnauskas, K. B., Miller, S. L., and Schapiro, A. C., 2020, "Fossil Fuel Combustion Is Driving Indoor CO2 Toward Levels Harmful to Human Cognition," GeoHealth, 4(5), p. e2019GH000237.

[8] Haile, M. G., Wossen, T., Tesfaye, K., and von Braun, J., 2017, "Impact of climate change, weather extremes, and price risk on global food supply," Economics of Disasters and Climate Change.

[9] Wilberforce, T., Baroutaji, A., Soudan, B., Al-Alami, A. H., and Olabi, A. G., 2019, "Outlook of carbon capture technology and challenges," Science of The Total Environment, 657, pp. 56-72.

[10] Dürre, P., and Eikmanns, B. J., 2015, "C1-carbon sources for chemical and fuel production by microbial gas fermentation," Current opinion in biotechnology, 35, pp. 63-72.

[11] Sorcar, S., Thompson, J., Hwang, Y., Park, Y. H., Majima, T., Grimes, C. A., Durrant, J. R., and In, S.-I., 2018, "High-rate solar-light photoconversion of CO2 to fuel: controllable transformation from C1 to C2 products," Energy & Environmental Science, 11(11), pp. 3183-3193.

[12] Alper, E., and Yuksel Orhan, O., 2017, "CO2 utilization: Developments in conversion processes," Petroleum, 3(1), pp. 109-126.

[13] Jacoby, M., 2013, "The Hidden Value Of Carbon Dioxide," Chemical and Engineering News, 91(26), pp. 21-22.

[14] Ménard, G., and Stephan, D. W., 2011, "Stoichiometric Reduction of CO_2 to CO by Aluminum-Based Frustrated Lewis Pairs," Angewandte Chemie, 123(36), pp. 8546-8549.

[15] Li, W., Wang, H., Jiang, X., Zhu, J., Liu, Z., Guo, X., and Song, C., 2018, "A short review of recent advances in CO_2 hydrogenation to hydrocarbons over heterogeneous catalysts," RSC Advances, 8(14), pp. 7651-7669.

[16] Ting, K. W., Toyao, T., Siddiki, S. M. A. H., and Shimizu, K.-i., 2019, "Low-Temperature Hydrogenation of CO_2 to Methanol over Heterogeneous TiO_2-Supported Re Catalysts," ACS Catalysis, 9(4), pp. 3685-3693.

[17] Nash, D. J., Restrepo, D. T., Parra, N. S., Giesler, K. E., Penabade, R. A., Aminpour, M., Le, D., Li, Z., Farha, O. K., Harper, J. K., Rahman, T. S., and Blair, R. G., 2016, "Heterogeneous Metal-Free Hydrogenation over Defect-Laden Hexagonal Boron Nitride," ACS Omega, 1(6), pp. 1343-1354.

[18] Nash, D. J., Chagoya, K. L., Felix, A., Torres-Davila, F. E., Jiang, T., Le, D., Tetard, L., Rahman, T. S., and Blair, R. G., 2019, "Analysis of the fluorescence of mechanically processed defect-laden hexagonal boron nitride and the role of oxygen in catalyst deactivation," Adv. Appl. Ceram., p. Ahead of Print.

[19] Kajdas, C. K., 2005, "Importance of the triboemission process for tribochemical reaction," Tribology International, 38(3), pp. 337-353.

[20] Avvakumov, E. G. e., Avvakumov, E. G., Avvakumov, G., Senna, M., and Kosova, N., 2001, Soft mechanochemical synthesis: a basis for new chemical technologies, Springer Science & Business Media.

[21] Davis, S. J., Lewis, N. S., Shaner, M., Aggarwal, S., Arent, D., Azevedo, I. L., Benson, S. M., Bradley, T., Brouwer, J., Chiang, Y.-M., Clack, C. T. M., Cohen, A., Doig, S., Edmonds, J., Fennell, P., Field, C. B., Hannegan, B., Hodge, B.-M., Hoffert, M. I., Ingersoll, E., Jaramillo, P., Lackner, K. S., Mach, K. J., Mastrandrea, M., Ogden, J., Peterson, P. F., Sanchez, D. L., Sperling, D., Stagner, J., Trancik, J. E., Yang, C.-J., and Caldeira, K., 2018, "Net-zero emissions energy systems," Science, 360(6396), p. eaas9793.

[22] Fernández, J. L. F., Hartmann, P., Schäffer, J., Puhlmann, H., and von Wilpert, K., 2017, "Initial recovery of compacted soil—planting and technical treatments decrease CO 2 concentrations in soil and promote root growth," Annals of Forest Science, 74(4), p. 73.

[23] Martin, J., 2016, "Fueling a Clean Transportation Future, Smart Fuel Choices for a Warming World," Union of Concerned Scientists.

[24] Chiaramonti, D., Prussi, M., Buffi, M., and Tacconi, D., 2014, "Sustainable bio kerosene: Process routes and industrial demonstration activities in aviation biofuels," Applied Energy, 136, pp. 767-774.

[25] Edwards, T., and Zabarnick, S., 1993, "Supercritical fuel deposition mechanisms," Industrial & Engineering Chemistry Research, 32(12), pp. 3117-3122.

[26] Arias Quintero, S., Schmitt, J., Blair, R., and Kapat, J., 2013, "Alternative Microturbine Fuels Feasibility Study Through Thermal Stability, Material Compatibility, and Engine Testing," Journal of Engineering for Gas Turbines and Power, 135(11).

[27] Sobel, D. R., and Spadaccini, L. J., 1995, "Hydrocarbon Fuel Cooling Technologies for Advanced Propulsion," (78804), p. V003T006A041.

[28] Martinez-Sanchez, M., and Pollard, J. E., 1998, "Spacecraft Electric Propulsion-An Overview," Journal of Propulsion and Power, 14(5), pp. 688-699.

[29] Bathgate, S. N., Bilek, M. M. M., and McKenzie, D. R., 2017, "Electrodeless plasma thrusters for spacecraft: a review," Plasma Science and Technology, 19(8), p. 083001.

[30] Shubov, M., 2021, "Gas Core Reactors for Deep Space Propulsion," arXiv preprint arXiv:2105.11533.

[31] Bermudez-Garcia, A., Voarino, P., and Raccurt, O., 2021, "Environments, needs and opportunities for future space photovoltaic power generation: A review," Applied Energy, 290, p. 116757.

[32] Levchenko, I., Xu, S., Teel, G., Mariotti, D., Walker, M., and Keidar, M., 2018, "Recent progress and perspectives of space electric propulsion systems based on smart nanomaterials," Nature communications, 9(1), pp. 1-19.

[33] David W. Miller, J. K., 2003, "Spacecraft Power Systems," Massachusetts Institute of Technology, OpenCourseWare.

[34] Pu, Z., Zhang, G., Hassanpour, A., Zheng, D., Wang, S., Liao, S., Chen, Z., and Sun, S., 2021, "Regenerative fuel cells: Recent progress, challenges, perspectives and their applications for space energy system," Applied Energy, 283, p. 116376.

[35] Dunbar, B., 2021, "Watts on the Moon Challenge," nasa.gov/wattson.

[36] Dunbar, B., 2017, "Juno Spacecraft and Instruments," https://www.nasa.gov/mission_pages/juno/spacecraft/index.html.

[37] Thompson, J. R., "Meet Europa Clipper," https://europa.nasa.gov/spacecraft/meet-europa-clipper/.

[38] 2021, "Electrical Power," https://mars.nasa.gov/mars2020/spacecraft/rover/electrical-power/.

[39] Chahal, M. S., 2012, "European Space Nuclear Power Programme: UK Activities," UK Space Agency.

[40] Barnett, A., "In Depth: Ulysses," https://solarsystem.nasa.gov/missions/ulysses/in-depth/.

[41] globalcarbonatlas.org, 2018, "CO_2 Emissions," http://www.globalcarbonatlas.org/en/CO2-emissions.

[42] Demas, A., 2013, "The Gigaton Question: How Much Geologic Carbon Storage Potential Does the United States Have?," USGS, http://www.usgs.gov/blogs/features/usgs_top_story/the-gigaton-question-how-much-geologic-carbon-storage-potential-does-the-united-states-have/.

[43] Roger, I., Shipman, M. A., and Symes, M. D., 2017, "Earth-abundant catalysts for electrochemical and photoelectrochemical water splitting," Nature Reviews Chemistry, 1, p. 0003.

[44] Jiang, T., Le, D., Chagoya, K. L., Nash, D. J., Blair, R. G., and Rahman, T. S., in preparation, "Catalytic Reduction of Carbon Dioxide to Methanol over Defect-Laden Hexagonal Boron Nitride: insights from theory."

[45] Grant, J. T., Carrero, C. A., Goeltl, F., Venegas, J., Mueller, P., Burt, S. P., Specht, S. E., McDermott, W. P., Chieregato, A., and Hermans, I., 2016, "Selective oxidative dehydrogenation of propane to propene using boron nitride catalysts," Science.

[46] Grant, J. T., McDermott, W. P., Venegas, J. M., Burt, S. P., Micka, J., Phivilay, S. P., Carrero, C. A., and Hermans, I., 2017, "Boron and Boron-Containing Catalysts for the Oxidative Dehydrogenation of Propane," ChemCatChem, 9(19), pp. 3623-3626.

[47] Mori, S., Xu, W.-C., Ishidzuki, T., Ogasawara, N., Imai, J., and Kobayashi, K., 1996, "Mechanochemical activation of catalysts for CO_2 methanation," Applied Catalysis A: General, 137(2), pp. 255-268.

[48] Zlochower, I. A., and Green, G. M., 2009, "The limiting oxygen concentration and flammability limits of gases and gas mixtures," Journal of Loss Prevention in the Process Industries, 22(4), pp. 499-505.

[49] Barth, R. R., Simmons, K. L., and SanMarchi, C., 2013, "SAND2013-8904: Polymers for Hydrogen Infrastructure and Vehicle Fuel Systems: Applications, Properties, and Gap Analysis," Sandia National Laboratories, Albuquerque, New Mexico.

[50] Giannozzi, P., Baroni, S., Bonini, N., Calandra, M., Car, R., Cavazzoni, C., Ceresoli, D., Chiarotti, G. L., Cococcioni, M., Dabo, I., Dal Corso, A., de Gironcoli, S., Fabris, S., Fratesi, G., Gebauer, R., Gerstmann, U., Gougoussis, C., Kokalj, A., Lazzeri, M., Martin-Samos, L., Marzari, N., Mauri, F., Mazzarello, R., Paolini, S., Pasquarello, A., Paulatto, L., Sbraccia, C., Scandolo, S., Sclauzero, G., Seitsonen, A. P., Smogunov, A., Umari, P., and Wentzcovitch, R. M., 2009, "QUANTUM ESPRESSO: a modular and open-source

software project for quantum simulations of materials," Journal of Physics: Condensed Matter, 21(39), p. 395502.

[51] Blöchl, P. E., 1994, "Projector augmented-wave method," Physical Review B, 50(24), pp. 17953-17979.

[52] Kresse, G., and Joubert, D., 1999, "From ultrasoft pseudopotentials to the projector augmented-wave method," Physical Review B, 59(3), pp. 1758-1775.

[53] Lee, K., Murray, E. D., Kong, L. Z., Lundqvist, B. I., and Langreth, D. C., 2010, "Higher-accuracy van der Waals density functional," Physical Review B, 82(8), p. 081101

[54] G. Henkelman, G. J., and H. Jónsson, 2000, "Improved tangent estimate in the nudged elastic band method for finding minimum energy paths and saddle points," J. Chem. Phys., 113(9978).

[55] Owuor, P. S., Park, O.-K., Woellner, C. F., Jalilov, A. S., Susarla, S., Joyner, J., Ozden, S., Duy, L., Villegas Salvatierra, R., Vajtai, R., Tour, J. M., Lou, J., Galvao, D. S., Tiwary, C. S., and Ajayan, P. M., 2017, "Lightweight Hexagonal Boron Nitride Foam for CO_2 Absorption," ACS Nano, 11(9), pp. 8944-8952.

[56] Gordon, I. E., 2020, "HITRANonline," https://hitran.org/.

[57] Scirè, S., Crisafulli, C., Maggiore, R., Minicò, S., and Galvagno, S., 1998, "Influence of the support on CO_2 methanation over Ru catalysts: an FT-IR study," Catalysis Letters, 51(1), pp. 41-45.

[58] Jiang, T. C., Katerina L.; Le, Duy; Blair, Richard G.; Rahman, Talat S. , 2020, "Density Functional Theory for Calculating Carbon Dioxide Adsorption onto Defect Hexagonal Boron Nitride," U. o. C. Florida, ed.

[59] Chen, C.-S., Cheng, W.-H., and Lin, S.-S., 2003, "Study of reverse water gas shift reaction by TPD, TPR and CO_2 hydrogenation over potassium-promoted Cu/SiO_2 catalyst," Applied Catalysis A, General, 238(1), pp. 55-67.

[60] Klepel, O., and Hunger, B., 2005, "Temperature-programmed desorption (TPD) of carbon dioxide on alkali-metal cation-exchanged faujasite type zeolites," Journal of Thermal Analysis & Calorimetry, 80(1), pp. 201-206.

[61] Weng, X., Cui, Y., Shaikhutdinov, S., and Freund, H.-J., 2019, "CO_2 Adsorption on CaO(001): Temperature-Programmed Desorption and Infrared Study," The Journal of Physical Chemistry C, 123(3), pp. 1880-1887.

[62] Beeler, A. J., Orendt, A. M., Grant, D. M., Cutts, P. W., Michl, J., Zilm, K. W., Downing, J. W., Facelli, J. C., Schindler, M. S., and Kutzelnigg, W., 1984, "Low-temperature carbon-13 magnetic resonance in solids. 3. Linear and pseudolinear molecules," Journal of the American Chemical Society, 106(25), pp. 7672-7676.

[63] Behrens, M., Studt, F., Kasatkin, I., Kühl, S., Hävecker, M., Abild-Pedersen, F., Zander, S., Girgsdies, F., Kurr, P., Kniep, B.-L., Tovar, M., Fischer, R. W., Nørskov, J. K., and Schlögl, R., 2012, "The Active Site of Methanol Synthesis over Cu/ZnO/Al_2O_3 Industrial Catalysts," Science, 336(6083), pp. 893-897.

[64] Polarz, S., Strunk, J., Ischenko, V., van den Berg, M. W. E., Hinrichsen, O., Muhler, M., and Driess, M., 2006, "On the role of oxygen defects in the catalytic performance of zinc oxide," Angew. Chem., Int. Ed., 45(18), pp. 2965-2969.

[65] Voorhoeve, R. J. H., Remeika, J. P., and Trimble, L. E., 1976, "Defect chemistry and catalysis in oxidation and reduction over perovskite-type oxides," Ann. N. Y. Acad. Sci., 272(Catal. Chem. Solid-State Inorg.), pp. 3-21.

[66] Ralphs, K., Hardacre, C., and James, S. L., 2013, "Application of heterogeneous catalysts prepared by mechanochemical synthesis," Chemical Society Reviews, 42(18), pp. 7701-7718.

[67] Immohr, S., Felderhoff, M., Weidenthaler, C., and Schüth, F., 2013, "An Orders-of-Magnitude Increase in the Rate of the Solid-Catalyzed CO Oxidation by In Situ Ball Milling," Angewandte Chemie International Edition, pp. n/a-n/a.

[68] Dutta, S., Dorfman, K. D., and Kumar, S., 2015, "Shear-Induced Desorption of Isolated Polymer Molecules from a Planar Wall," ACS Macro Letters, 4(3), pp. 271-274.

[69] Kaufman Rechulski, M. D., Käldström, M., Richter, U., Schüth, F., and Rinaldi, R., 2015, "Mechanocatalytic Depolymerization of Lignocellulose Performed on Hectogram and Kilogram Scales," Industrial & Engineering Chemistry Research, 54(16), pp. 4581-4592.

[70] Brauer, G., 1963, "Boron Nitride," Preparative Inorganic Chemistry, G. Brauer, ed., Academic Press, New York, p. 789.

[71] Blair, R., 2015, "Mechanical and Combined Chemical and Mechanical Treatment of Biomass," Production of Biofuels and Chemicals with Ultrasound, Z. Fang, J. R. L. Smith, and X. Qi, eds., Springer Netherlands, pp. 269-288.

[72] Chen, Y., Choi, S., and Thompson, L. T., 2016, "Low temperature CO_2 hydrogenation to alcohols and hydrocarbons over Mo2C supported metal catalysts," Journal of Catalysis, 343, pp. 147-156.

[73] Chiang, C.-L., Lin, K.-S., Chuang, H.-W., and Wu, C.-M., 2017, "Conversion of hydrogen/carbon dioxide into formic acid and methanol over Cu/$CuCr_2O_4$ catalyst," International Journal of Hydrogen Energy, 42(37), pp. 23647-23663.

[74] Ao, M., Pham, G. H., Sunarso, J., Tade, M. O., and Liu, S. M., 2018, "Active Centers of Catalysts for Higher Alcohol Synthesis from Syngas: A Review," ACS Catalysis, 8(8), pp. 7025-7050.

[75] Barton, E. E., Rampulla, D. M., and Bocarsly, A. B., 2008, "Selective Solar-Driven Reduction of CO_2 to Methanol Using a Catalyzed p-GaP Based Photoelectrochemical Cell," Journal of the American Chemical Society, 130(20), pp. 6342-6344.

[76] Robert D. Crangle, J., 2016, "2016 Minerals Yearbook: Boron," U.S. Geological Survey, ed., U.S. Department of the Interior, Washinton, D.C., p. 7.

[77] Fung, B., Khitrin, A., and Ermolaev, K., 2000, "An improved broadband decoupling sequence for liquid crystals and solids," Journal of magnetic resonance, 142(1), pp. 97-101.

[78] Perdew, J. P., and Wang, Y., 1992, "Pair-distribution function and its coupling-constant average for the spin-polarized electron gas," Physical Review B, 46(20), p. 12947.

[79] Becke, A. D., 1993, "Density-functional thermochemistry. III. The role of exact exchange," The Journal of Chemical Physics, 98(7), pp. 5648-5652.

[80] Harper, J. K., Barich, D. H., Hu, J. Z., Strobel, G. A., and Grant, D. M., 2003, "Stereochemical analysis by solid-state NMR: structural predictions in ambuic acid," The Journal of organic chemistry, 68(12), pp. 4609-4614.

[81] Spadaccini, L. J., Sobel, D. R., and Huang, H., 1999, "Deposit Formation and Mitigation in Aircraft Fuels," Journal of Engineering for Gas Turbines and Power, 123(4), pp. 741-746.

[82] Spadaccini, L. J., and Huang, H., 2003, "On-Line Fuel Deoxygenation for Coke Suppression," Journal of Engineering for Gas Turbines and Power, 125(3), pp. 686-692.

[83] 1991, Thermal oxidation stability of aviation turbine fuels.

[84] Edwards*, T. I. M., 2006, "CRACKING AND DEPOSITION BEHAVIOR OF SUPERCRITICAL HYDROCARBON AVIATION FUELS," Combustion Science and Technology, 178(1-3), pp. 307-334.

[85] Zhu, Y., Yan, S., Zhao, R., and Jiang, P., 2018, "Experimental Investigation of Flow Coking and Coke Deposition of Supercritical Hydrocarbon Fuels in Porous Media," Energy & Fuels, 32(3), pp. 2941-2948.

[86] Venkataraman, R., and Eser, S., 2008, "Characterization of Solid Deposits Formed from Short Durations of Jet Fuel Degradation: Carbonaceous Solids," pp. 9337-9350.

[87] Ervin, J. S., Ward, T. A., Williams, T. F., and Bento, J., 2003, "Surface deposition within treated and untreated stainless steel tubes resulting from thermal-oxidative and pyrolytic degradation of jet fuel," pp. 577-586.

[88] Ram Mohan, A., and Eser, S., 2011, "Effectiveness of Low-Pressure Metal–Organic Chemical Vapor Deposition Coatings on Metal Surfaces for the Mitigation of Fouling from Heated Jet Fuel," Industrial & Engineering Chemistry Research, 50(12), pp. 7290-7304.

[89] Zabarnick, S., 1994, "Studies of Jet Fuel Thermal Stability and Oxidation Using a Quartz Crystal Microbalance and Pressure Measurements," Industrial & Engineering Chemistry Research, 33(5), pp. 1348-1354.

[90] Farrell, J., John Holladay, and Robert Wagner, 2018, "Fuel Blendstocks with the Potential to Optimize Future Gasoline Engine Performance: Identification of Five Chemical Families for Detailed Evaluation," U.S. Department of Energy, DOE/GO-102018-4970.

[91] Tran, L.-S., Togbé, C., Liu, D., Felsmann, D., Oßwald, P., Glaude, P.-A., Fournet, R., Sirjean, B., Battin-Leclerc, F., and Kohse-Höinghaus, K., 2014, "Combustion chemistry and flame structure of furan group biofuels using molecular-beam mass spectrometry and gas chromatography – Part II: 2-Methylfuran," Combustion and Flame, 161, pp. 766-779.

[92] Bao, X., Jiang, Y., Xu, H., Wang, C., Lattimore, T., and Tang, L., 2017, "Laminar flame characteristics of cyclopentanone at elevated temperatures," Applied Energy, p. 671.

[93] Westbrook, C. K., Pitz, W. J., Westmoreland, P. R., Dryer, F. L., Chaos, M., Osswald, P., Kohse-Höinghaus, K., Cool, T. A., Wang, J., Yang, B., Hansen, N., and Kasper, T., 2009, "A detailed chemical kinetic reaction mechanism for oxidation of four small alkyl esters in laminar premixed flames," Proceedings of the Combustion Institute, 32, pp. 221-228.

[94] Stephanie, R., and Christian, T., 2004, "Raman Spectroscopy of Graphite," Philosophical Transactions: Mathematical, Physical and Engineering Sciences(1824), p. 2271.

[95] Westbrook, C. K., Pitz, W. J., and Curran, H. J., 2006, "Chemical Kinetic Modeling Study of the Effects of Oxygenated Hydrocarbons on Soot Emissions from Diesel Engines," The Journal of Physical Chemistry A, 110(21), pp. 6912-6922.

[96] Pepiot-Desjardins, P., Pitsch, H., Malhotra, R., Kirby, S. R., and Boehman, A. L., 2008, "Structural group analysis for soot reduction tendency of oxygenated fuels," Combustion and Flame, 154, pp. 191-205.

[97] Omidvarborna, H., Kumar, A., and Kim, D.-S., 2016, "Variation of diesel soot characteristics by different types and blends of biodiesel in a laboratory combustion chamber," Science of the Total Environment, 544, pp. 450-459.

[98] Zhou, Y.-H., Lv, P.-H., and Wang, G.-C., 2006, "DFT studies of methanol decomposition on Ni(100) surface: Compared with Ni(111) surface," Journal of Molecular Catalysis A: Chemical, 258(1), pp. 203-215.

[99] Bernardo, C. G. P. M., and Gomes, J. A. N. F., 2001, "The adsorption of ethylene on the (100) surfaces of platinum, palladium and nickel: a DFT study," Journal of Molecular Structure: THEOCHEM, 542(1), pp. 263-271.

[100] Grimm, R. L., Mangrum, J. B., and Dunbar, R. C., 2004, "Complexation of Gas-Phase Metal Ions with Furan: Experimental and Quantum Chemical Binding Energies," The Journal of Physical Chemistry A, 108(49), pp. 10897-10905.

[101] Gomez, A., Sidebotham, G., and Glassman, I., 1984, "Sooting behavior in temperature-controlled laminar diffusion flames," Combustion and Flame, 58, pp. 45-57.

[102] Ren, W., Lam, K.-Y., Davidson, D. F., Hanson, R. K., and Yang, X., 2017, "Pyrolysis and oxidation of methyl acetate in a shock tube: A multi-species time-history study," Proceedings of the Combustion Institute(1), p. 255.

[103] Osswald, P., Struckmeier, U., Kasper, T., Kohse-Hoinghaus, K., Juan, W., Cool, T. A., Hansen, N., and Westmoreland, P. R., 2007, "Isomer-specific fuel destruction pathways in rich flames of methyl acetate and ethyl formate and consequences for the combustion chemistry of esters," Journal of Physical Chemistry A(19), p. 4093.

[104] Yang, X., Felsmann, D., Kurimoto, N., Krüger, J., Wada, T., Tan, T., Carter, E. A., Kohse-Höinghaus, K., and Ju, Y., 2015, "Kinetic studies of methyl acetate pyrolysis and oxidation in a flow reactor and a low-pressure flat flame using molecular-beam mass spectrometry," Proceedings of the Combustion Institute, 35, pp. 491-498.

[105] Zaki, T., 2005, "Catalytic dehydration of ethanol using transition metal oxide catalysts," Journal of Colloid And Interface Science, 284, pp. 606-613.

[106] Vlasov, P. A., and Warnatz, J., 2002, "Detailed kinetic modeling of soot formation in hydrocarbon pyrolysis behind shock waves," Proceedings of the Combustion Institute, 29, pp. 2335-2341.

[107] Kameya, Y., Hayashi, T., and Motosuke, M., 2016, "Oxidation-resistant graphitic surface nanostructure of carbon black developed by ethanol thermal decomposition," Diamond and Related Materials, 65, pp. 26-31.

[108] Lapin, N. V., and Bezhok, V. S., 2011, "Low-temperature reforming of ethanol on a nickel-copper catalyst," Russian Journal of Applied Chemistry(6), p. 1007.

[109] Launius, R. D., 2004, Frontiers of space exploration, Greenwood Publishing Group.

[110] O'Donnell, D. J., 1994, "Overcoming barriers to space travel," Space Policy, 10(4), pp. 252-255.

[111] Vedda, J., 2008, "Challenges to the Sustainability of Space Exploration," Astropolitics, 6, pp. 22-49.

[112] Masson-Zwaan, T., and Freeland, S., 2010, "Between heaven and earth: The legal challenges of human space travel," Acta Astronautica, 66(11), pp. 1597-1607.

[113] Iliopoulos, N., and Esteban, M., 2020, "Sustainable space exploration and its relevance to the privatization of space ventures," Acta Astronautica, 167, pp. 85-92.

[114] 2016, "Space Travel: Risk, Ethics, and Governance in Commercial Human Spaceflight," New Space, 4(2), pp. 83-97.

[115] Bainbridge, W. S., 2009, "Motivations for space exploration," Futures, 41(8), pp. 514-522.

[116] Braddock, M., 2017, "Ergonomic challenges for astronauts during space travel and the need for space medicine," J Ergonomics, 7(221), p. 2.

[117] Genah, S., Monici, M., and Morbidelli, L., 2021, "The Effect of Space Travel on Bone Metabolism: Considerations on Today's Major Challenges and Advances in Pharmacology," International Journal of Molecular Sciences, 22(9), p. 4585.

[118] Galts, C., 2017, "A journey to Mars: The medical challenges associated with deep space travel and possible solutions," University of British Columbia Medical Journal, 8, pp. 38-39.

[119] Euroconsult, 2018, "Government Funding in Space Exploration to Surpass $20 Billion by 2027," Prospects for Space Exploration

[120] Dunbar, B., 2021, "Planetary Missions Program Office," https://www.nasa.gov/planetarymissions/overview.html.

[121] Piazza, E., "Legacy Power Systems," https://rps.nasa.gov/power-and-thermal-systems/legacy-power-systems/.

[122] Steven D. Howe, T. R., Douglas Crawford, Jorge Navarro, 2013, "Economical Production of Pu-238," Nuclear and Emerging Technologies for Space Albuquerque, NM.

[123] Peter Atkins, J. d. P., 2010, Physical Chemistry, Oxford University Press, Great Britain.

[124] Technology, N. I. o. S. a., 2018, "NIST Chemistry WebBook," U.S. Department of Commerce.

[125] Nefedov, R. A., Ferapontov, Y. A., and Kozlova, N. P., 2016, "Problem of the lithium peroxide thermal stability," IOP Conference Series: Materials Science and Engineering, 112, p. 012027.

[126] Health, T. N. I. f. O. S. a., 2019, "NIOSH Pocket Guide to Chemical Hazards," Centers for Disease Control and Prevention (CDC).

[127] Cole, S. S., and Taylor, N. W., 1935, "THE SYSTEM Na2O-B2O3, IV Vapor Pressures of Boric Oxide, Sodium Metaborate, and Sodium Diborate between 1150°C and 1400°C," Journal of the American Ceramic Society, 18(1-12), pp. 82-85.